

DEPARTMENT OF EARTH AND ENVIRONMENTAL SCIENCES

PhD program in Chemical, Geological and Environmental Sciences

Cycle XXXVII

Curriculum in Chemical Sciences

Ph.D. Thesis

**Geochemical study of pyrite persistence in the
sedimentary records**

Cruz Muñoz Enmanuel

883903

Tutor: Prof. Davide Ballabio

Supervisor: Prof. Fabio Gosetti

Co-supervisor: Prof. Sergio Andò

Coordinator: Prof. Marco Giovanni Malusà

ACADEMIC YEAR: 2023-2024

Enmanuel Cruz Muñoz

Geochemical study of pyrite persistence in the sedimentary records

enmanuel.cruzmunoz@unimib.it

University of Milano-Bicocca

Milano Chemometrics and QSAR Research Group

Dept. of Earth and Environmental Sciences

P.za della Scienza, 1

20126 Milano - Italy

Acknowledgements

First, I would like to express my sincere gratitude to my supervisors, Fabio Gosetti and Sergio Andò, for their guidance over these past three years, for sharing their knowledge and for the invaluable advice that helped me grow as a scientist.

Special thanks to Davide Ballabio, for always being open to discussion on various topics, for trusting me, for caring about my adaptation in this country over the years, as well as for his human and scientific quality.

I'm also grateful to the other members of the Milano Chemometrics and QSAR Research Group - Roberto Todeschini, Viviana Consonni and Veronica Termopoli - for helping me feel at home in a new country and welcoming me as part of the group.

Heartfelt thanks to Eduardo Garzanti and all the colleagues at the Laboratory for Sediment Provenance Studies. Their passion has been contagious, opening my eyes to a field of science I was previously unfamiliar with, Geology, and introducing me to the fascinating world of minerals.

A mi familia, por haberme permitido estar hoy escribiendo estas palabras de agradecimiento, ya que, sin sus esfuerzos, sacrificios realizados y apoyo constante, esta maravillosa aventura no habría sido posible.

E infine, ma non per questo meno importante, alla mia compagna, il cui supporto in questi anni è stato essenziale per il mio percorso di dottorato e che rappresenta una delle ragioni principali del mio amore per questo Paese.

A mi madre,

“The universe seems neither benign nor hostile, merely indifferent.”

Carl Sagan

Content

List of Abbreviations	i
List of Figures	iii
List of Tables	vi
Preface: aim and structure of the thesis	vii
Part 1: Introduction	
1. Chapter: Background	3
1.1 Pyrite	4
1.2 Chemical and crystal structure	5
2. Chapter: Reactions	9
2.1 Genesis	10
2.1.1 Metamorphic formation	10
2.1.2 Hydrothermal formation	11
2.1.3 Sedimentary formation	12
2.2 Weathering processes	14
2.2.1 Oxidative weathering of pyrite	17
Part 2: Instrumentation and data analysis methods	
3. Chapter: Instrumentation	23
3.1 Raman spectroscopy	24
3.1.1 Hyperspectral Imaging	28
3.2 SEM-EDS	30
3.3 ICP-OES	31
3.4 Chromatographic methods	32
3.4.1 Ion Chromatography	33
3.4.2 High-performance Liquid Chromatography	33
4. Chapter: Data analysis methods	36
4.1 Experimental design	37
4.1.1 Screening designs	39
4.1.2 Plackett-Burman design	39
4.2 Multivariate analysis	40
4.2.1 Data pre-processing	41

4.2.2 Principal Component Analysis	43
4.2.3 K-means clustering	45
4.2.4 Pearson correlation	46
4.2.5 Multivariate Curve Resolution – alternating least squares	47

Part 3: Studies conducted in relation to the main topics

5. Chapter: Raman library	52
5.1 Samples	53
5.2 Instrumentation and acquisition parameters	53
5.3 Spectra acquired	54
5.4 Software development	58
5.5 Conclusions	62

6. Chapter: Weathering products characterization by Raman hyperspectral imaging	64
6.1 Sample	65
6.2 Instrumentation and hyperspectral image	65
6.3 Software	66
6.4 Results and discussion	66
6.4.1 Spectral pre-processing	66
6.4.2 Principal Component Analysis	68
6.4.3 Analysis of the major features	72
6.4.4 Analysis of the minor features	76
6.4.5 Compositional images	77
6.5 Conclusions	78

7. Chapter: Data-driven simulation of oxidative weathering of pyrite	80
7.1 Material and methods	81
7.1.1 Sample	81
7.1.2 Reagents	81
7.1.3 Instrumentation	81
7.1.4 Software	82
7.1.5 Experimental design	82
7.1.6 Experimental procedure and setup	84

7.2 Results	85
7.2.1 Ion chromatography analysis	85
7.2.2 ICP OES analysis	86
7.2.3 Raman hyperspectral images	87
7.2.4 Elemental sulfur quantification	88
7.3 Discussion	90
7.3.1 Screening of the factors	90
7.3.2 Chemical discussion: effect of significant factors	95
7.3.3 Raman hyperspectral image analysis	97
7.4 Conclusions	100
8 Chapter: Case study: sedimentary pyrite in river sands of Taiwan	102
8.1 Material and instrumentation	103
8.1.1 Samples	103
8.1.2 Instrumentation	104
8.1.3 Software	104
8.2 Results	104
8.2.1 Optical microscope	104
8.2.2 Raman spectroscopy	106
8.2.3 SEM-EDS	111
8.3 Discussion	113
8.3.1 Analysis of the samples collected	113
8.3.2 Analysis of geochemical data from the literature	115
8.3.3 Geochemical thoughts on pyrite persistence	120
8.4 Conclusions	123
Concluding remarks and future perspectives	ix
Bibliography	.xi
Publications during the PhD course	xxv
Congresses and courses attended	xxvi
Research period abroad	xxvi

List of Abbreviations

ACS	<i>American Chemical Society</i>
A_g	<i>Singly degenerate</i>
AMD	<i>Acid mine drainage</i>
Amp	<i>Amphibole</i>
Ap	<i>Apatite</i>
BSE	<i>Backscattered electrons</i>
CCD	<i>Charge-coupled device</i>
Cpx	<i>Clinopyroxene</i>
DAD	<i>Diode Array Detector</i>
DoE	<i>Design of experiments</i>
DoF	<i>Degrees of freedom</i>
E_g	<i>Doubly degenerate</i>
Ep	<i>Epidote</i>
FEG	<i>Field emission gun</i>
GC	<i>Gas chromatography</i>
Grt	<i>Garnet</i>
HM	<i>Heavy mineral</i>
HMC	<i>Heavy mineral concentration</i>
HPLC	<i>High-performance Liquid Chromatography</i>
HSI	<i>Hyperspectral imaging</i>
IC	<i>Ion chromatography</i>
ICP OES	<i>Inductively coupled plasma atomic emission spectroscopy</i>
KF	<i>K-feldspar</i>
LC	<i>Liquid chromatography</i>
Lc	<i>Carbonate</i>
Lmf	<i>Medium/high-rank felsic metamorphic</i>
Lms	<i>Low-rank metasedimentary</i>
Lmv	<i>Metavolcanic and metabasite</i>
LO	<i>Longitudinal optical overtone phonon</i>
Ls	<i>Shale/siltstone</i>
Lu	<i>Ultramafic</i>
Lv	<i>Volcanic</i>
LVs	<i>Latent variables</i>
MCR-ALS	<i>Multivariate Curve Resolution – alternating least squares</i>
MLR	<i>Multiple linear least-squares regression</i>
Opx	<i>Orthopyroxene</i>
OWP	<i>Oxidative weathering of pyrite</i>
P	<i>Plagioclase</i>
PCA	<i>Principal Component Analysis</i>
PCs	<i>Principal components</i>
PE	<i>Primary electrons</i>
PLS	<i>Partial least squares</i>
Q	<i>Quartz</i>

SE	<i>Secondary electrons</i>
SEM-EDS	<i>Scanning Electron Microscopy-X-Ray Energy Dispersive Spectroscopy</i>
SNV	<i>Standard Normal Variate</i>
St	<i>Staurolite</i>
T_g	<i>Triply degenerate</i>
tHMC	<i>Transparent Heavy-Mineral Concentration.</i>
Ttn	<i>Titanite</i>
UV	<i>Ultraviolet</i>
XPS	<i>X-ray photoelectron spectroscopy</i>
XRD	<i>X-ray Diffraction</i>
ZTR	<i>Zircon/tourmaline/Ti oxides index</i>

List of figures

1.1	<i>Some common crystallographic forms of pyrite found in nature</i>	6
2.1	<i>Partially oxidized pyrite sample. The reddish patina in some areas of the surface is a symptom of the formation of iron oxides</i>	9
2.2	<i>Pyrite's relationship with the sulfur, carbon and oxygen cycles</i>	16
3.1	<i>Raman effect and (b) scheme of a Raman spectrometer.</i>	27
3.2	<i>Three-dimensional data array of a hyperspectral image</i>	29
3.3	<i>Principles of SEM-EDS</i>	31
3.4	<i>Principles of ICP OES</i>	32
4.1	<i>SNV applied on several Raman spectra</i>	42
4.2	<i>Baseline correction by adapting the spectrum to an asymmetric truncated quadratic cost function of order 7 and a threshold of 0.1</i>	42
4.3	<i>Savitzky-Golay smoothing with a polynomial order of 2 and a window of 15</i>	43
4.4	<i>Derivative pre-processing on normal spectra (black) and spectra showing additive (red) and multiplicative (green) scattering effect</i>	43
4.5	<i>Principal Component Analysis decomposition</i>	45
4.6	<i>Pearson correlation. From left to right, spectra are strongly correlated, moderately correlated and not correlated</i>	46
4.7	<i>MCR-ALS applied to a hyperspectral image</i>	47
5.1	<i>Pyrite spectra of four different locations. Spectra has been pre-processed (baseline correction, smoothing and scaling)</i>	54
5.2	<i>Effect on the relative intensity of E_g/A_g peaks with rotation. A peak highlighted in red means higher intensity with respect to the other</i>	56
5.3	<i>Some of the Raman spectra of goethite, hematite, magnetite, chalcopyrite, marcasite and arsenopyrite are included in the library. Spectra were normalized for easier comparison</i>	57
5.4	<i>Main window of the software</i>	58
5.5	<i>Template to write information on each of the samples included in the project</i>	59
5.6	<i>Window to load the spectral file(s) of the sample being included in the project. A similar window will appear for loading images</i>	60
5.7	<i>Example of how the main window looks once a project has been loaded/created. It is possible to browse through different samples and spectra</i>	60
5.8	<i>Window for comparing spectra. First, samples are selected by clicking on the drop-down list of samples. Then, spectra by clicking directly on the fixed list</i>	61
5.9	<i>In this window, there are different options for baseline correction, and it allows the modification of the parameters. It is also possible to perform smoothing and scaling</i>	61
5.10	<i>The information on the samples introduced when the project was created will appear summarized in table format</i>	62
6.1	<i>Pyrite sample analyzed in this study. Brownish areas at the corners and edges are presumably alteration products, whereas the bright zones are unaltered pyrite</i>	65
6.2	<i>Spectra of some of the saturated pixels detected</i>	67
6.3	<i>Fake RGB images. (a) Raw data, (b) after saturation and cosmic spikes removal, (c) after baseline correction and (d) after smoothing and SNV</i>	68
6.4	<i>Unfolding of a hyperspectral image into a two-dimensional matrix</i>	68
6.5	<i>Scores (a, b, c) and loadings (d, e, f) for the first three principal components, respectively</i>	69
6.6	<i>Scores and loadings for PC4 to PC10 (except PC9). The data variance explained by these PCs is ~10.6 %</i>	70
6.7	<i>Scores and loadings of PC9. The shape of the loadings is typical of Raman shifting</i>	71

6.8	<i>Selected pixel (positive loadings) vs. the normal pyrite peaks in the rest of the image (negative loadings)</i>	71
6.9	<i>Spatial distribution of the pixels belonging to the main (green) and minor (white) features datasets</i>	72
6.10	<i>Distribution maps (a, b, c) and reference spectra (black) versus pure spectra (red) plots (d, e, f) calculated by the MCR-ALS model</i>	74
6.11	<i>Distribution maps (a, b, c) and pure spectra (red) plots (d, e, f) calculated by the non-targeted MCR-ALS model</i>	75
6.12	<i>Centroids found after K-means clustering analysis of the minor features dataset</i>	77
6.13	<i>Real image of the analyzed surface (a) and composite images (b) and (c). Pixels belonging to component 1 are colored in blue, those to component 2 in red and those to component 3 in black. Pixels related to minor features are colored in white</i>	77
6.14	<i>Scheme of the Chemometrics and Hyperspectral imaging approach proposed in the study</i>	79
7.1	<i>Pyrite samples used in the experiments carried out</i>	81
7.2	<i>Overlapped chromatograms of sulfur standards (a) and samples (b) by operating at 254 nm</i>	89
7.3	<i>Coefficients of the PLS model calculated with 6 latent variables (LVs) over elemental sulfur amount (expressed in logarithmic scale) response</i>	92
7.4	<i>Scores (a) and loadings (b) plot using the real values of the factors as dataset, before and after the conclusion of the experiments</i>	93
7.5	<i>Correlation between (a) the difference of total Fe concentration and the amount of sulfur, (b) the difference of sulfate concentration and the amount of sulfur, (c) the difference of total Fe concentration and mass loss and (d) the difference of sulfate concentration and mass loss</i>	94
7.6	<i>Correlation between the amount of sulfur and mass loss responses</i>	94
7.7	<i>Scores (a) and loadings (b) plot considering each factor as the difference between t_0 and t_f. Samples are colored from white to black depending on the amount of sulfur</i>	95
7.8	<i>Real images of sample N12 at t_0 (a) and t_f (b). Pearson correlation model by using a pyrite reference spectrum at t_0 (c) and t_f (d)</i>	97
7.9	<i>PCA score maps (upper) and loadings (bottom). From left to right and from up to down, samples N1 to N16</i>	98
7.10	<i>Pearson correlation calculated using an elemental sulfur reference spectrum. From left to right and from up to down, samples N1 to N16</i>	99
7.11	<i>Pearson correlation calculated using a pyrite reference spectrum. From left to right and from up to down, samples N1 to N16</i>	100
8.1	<i>Map of Taiwan and images of the sampling points. Images acquired from Google Earth</i>	103
8.2	<i>Pyrite crystal in rock fragment under transmitted light (left) and reflected light (right)</i>	105
8.3	<i>From left to the right, pyrite fragments identified in Taimali, Dazhu and Fenggang rivers, respectively</i>	105
8.4	<i>Pyrite fragments identified in the sample collected in Luye river</i>	106
8.5	<i>Schematic representation on the HM fraction preparation of the sample collected in Luye</i>	107
8.6	<i>Mosaic image of the araldite block acquired with the optical microscope of the Raman spectrometer</i>	107
8.7	<i>Raman spectra acquired from some of the samples analyzed. The objective used was the long working distance (LWD) 50x. The rest of the numbers refer to the exposure time (s), the power of the laser (%) and the number of accumulations, respectively</i>	108
8.8	<i>(a) Exposure time and number of accumulations equal to 1 s and 10, respectively. (b) Exposure time and number of accumulations equal to 5 s and 10, respectively. In both cases, from the top to the bottom, the power of the laser ranges from 0.1 to 100 %</i>	109
8.9	<i>(a) Exposure time and number of accumulations equal to 10 s and 1, respectively. (b) Exposure time and number of accumulations equal to 50 s and 1, respectively. In both cases, from the top to the bottom, the power of the laser ranges from 0.1 to 100 %</i>	110

8.10	<i>EDS analysis of some of the samples whose Raman spectra have been shown above as examples in Section 8.2.2</i>	111
8.11	<i>Example of EDS images based on the elemental composition of the sample</i>	112
8.12	<i>Scores (top) and loadings(bottom) of PC1 vs. PC2 (left) and PC3 vs. PC4 (right)</i>	117
8.13	<i>Scores of PC1 vs. PC2 vs. PC3</i>	118
8.14	<i>Correlation plot between some of the variables</i>	119
8.15	<i>Geological map adapted from [164]. Rivers where the sedimentary samples were collected are highlighted in red</i>	120
8.16	<i>PCA of the petrographic and mineralogical data reported in [165]. The scores of the first two PCs are reported, being each sample colored according to their provenance (a), to their drainage (b) or to their relative geographic position (c). Common loadings for PC1 and PC2 is shown in (d)</i>	121

List of tables

1.1	<i>Physical properties of pyrite</i>	5
3.1	<i>Theoretical diameter (μm) of the spot of the laser depending on the magnification and the monochromatic radiation employed</i>	28
4.1	<i>Plackett-Burman experimental matrix. Maximum and minimum levels are denoted by “+” and “-”, respectively. The number of degrees of liberty is $12-7-1=4$</i>	40
5.1	<i>Peak position and occurrence of the E_g, A_g and T_g vibrational modes of the 131 spectra analyzed</i>	55
5.2	<i>Vibrational modes of pyrite in different studies carried out in the literature</i>	55
6.1	<i>Distribution of the different mineralogical phases in the two MCR-ALS models (using a Raman library or the pure variable selection method for the initial estimation of the spectral profiles</i>	78
7.1	<i>Experimental domain of the screened factors in the Plackett-Burman design</i>	83
7.2	<i>Experimental plan with $K=13$ factors and $N=16$ experiment (plus 3 central replicates). Green and cell mean a high and low level for that experiment, respectively. All reported factors are in mg.L^{-1}, except for Size which unit is mm. Sample labels N1 to N16 will be used hereafter</i>	83
7.3	<i>Results of the Ion chromatography analyses reported as the mean value \pm standard deviation of the mean. Samples N1 to N16 refer to the samples of the weathering experiments, whereas C1 to C3 are the central point samples</i>	86
7.4	<i>Results of the ICP-OES analyses reported as the mean value \pm standard deviation of the mean. Samples N1 to N16 refer to the samples of the weathering experiments, whereas C1 to C3 are the central point samples The Fe factor is the total concentration of Fe^{2+} and Fe^{3+}, although it is expected that almost all the iron at t_0 is present as Fe^{3+} due to the very low pH of the solutions</i>	87
7.5	<i>Sulfur is reported as mean value \pm standard deviation of the mean. Mass loss is reported as the difference between t_0 and t_f</i>	89
7.6	<i>Standardized coefficients calculated by PLS regression and confidence limits</i>	92
8.1	<i>Geographical coordinates expressed in decimal degrees scale</i>	103
8.2	<i>HMC of the sedimentary samples</i>	113
8.3	<i>Pyrite percentages found in the HM fraction, expressed as total percentage with respect to all the grains of the sedimentary fraction analyzed</i>	113
8.4	<i>Elemental composition of the different inclusions found in the analyzed pyrite fragments from Luye. Positive presence is denoted by (+) while negative presence is denoted by (-)</i>	115
8.5	<i>Water chemistry and erosion rate data collected from the literature, except for % of pyrite values, which have been generated in this study</i>	117

Preface: aim and structure of the thesis

This doctoral thesis aims to evaluate the oxidative weathering of pyrite in geological records. This is a complex mechanism that involves many different reactions, intermediate and alteration products. Depending on the environmental conditions in which the pyrite is found, it may undergo chemical weathering to a greater or lesser extent. Since this project belongs to the chemical sciences curriculum, we focus on the development of methodologies for the characterization of the samples, the identification of weathering products on the surface and the assessment of their spatial distribution. In addition, pyrite oxidation has been simulated at laboratory scale, to provide some insights on the factor that influences the process. Consequently, all these methodologies were guided by data analysis methods, which are a powerful tool for many fields of science today, demonstrating how they can help in tackling complex geological problems. The structure of this dissertation is divided into three parts and has a total of eight chapters:

The first part, which includes two chapters, provides some general information on the physical and chemical properties of pyrite, the processes leading to its formation and the main reactions involved in the weathering mechanism. All this background information is essential to address some of the studies carried out during the period of the doctorate.

The second part, which also includes two chapters, focuses on the instrumentation and data analysis methods employed, providing general knowledge of the principles underlying these analytical techniques and a general mathematical framework for understanding the data-driven approaches followed.

The third part consists of a description of four main studies carried out, with a chapter devoted to each of them. In particular, the first study was the acquisition of a Raman library of several mineralogical samples and the development of software for this library management and data pre-processing facilities. The second study describes a methodology based on Hyperspectral Imaging for the evaluation of pyrite oxidation products, describing each of the steps followed and the main results of the analysis of a pyrite sample used to validate this methodology. The third study describes

the data-driven experiments carried out in the laboratory for the simulation of pyrite oxidation, providing results on the significant variables that positively or negatively affect this mechanism. Finally, the fourth study is the application of some of the analytical methods previously described to a case study in Taiwan, where unweathered pyrite was found in river sands. The objective of this study was to find a chemical explanation on pyrite's persistence in this geological context.

This doctoral project has been made possible thanks to funding received from the Italian *MIUR project Dipartimenti di Eccellenza 2018–2022*.

Part I

Introduction

Chapter: Background

1

” *The dust we tread upon was once alive.*

— Lord Byron

Metal sulfides can be considered one of the most important ore mineral groups. These compounds are the result of combining S^{2-} as the anion with different metals, which act as the cation. Some minerals are formed by a combination of S and As or Sb as the anions. For instance, sulfosalts are a special category of sulfide minerals following the general formula $M_aT_bX_c$ in which M can be constituted by some metals such as Cu, Ag or Pb, whereas T is commonly As, Sb or Bi and X is constituted by S atoms.

Sulfide minerals are a very well-known group of which several hundred minerals have been discovered in the nature. However, only five of these minerals are considered rock-forming due to their abundance as accessory minerals [1]. These are pyrite, pyrrhotite, chalcopyrite, galena and sphalerite, being pyrite and pyrrhotite the most abundant. Special mention should be made to another type of amorphous iron sulfides usually found beneath the surface of some reducing soils and sediments: mackinawite and greigite. Compared to pyrite, these two amorphous iron sulfides are metastable [2].

The importance of sulfide minerals groups lies in the impact these minerals have on the environment, releasing metals as mineable deposits, therefore being potential sources of soil, water or air pollution. Sulfides exposed to the atmosphere generate sulfuric acid [3]. This fact can be linked to mine wastes, known as acid mine drainage or by rocks containing sulfides, in this case known as acid rock drainage.

Therefore, this chapter will provide general information about pyrite that will be helpful when discussing in later chapters the specific pyrite samples analyzed in some of the studies carried out in the thesis.

1.1 Pyrite

Pyrite (FeS_2) is the most abundant sulfide on the Earth's surface, constituting over 95% of total sulfides [4]. The name given to this mineral is derived from the Latin "*pyrītēs*" or the Greek "*pyrītēs lithos*", which means "stone on fire" or "burning stone". Its etymology alludes to the fact that when a fragment of this mineral is struck against a hard surface it sparkles. This quality made pyrite useful in ancient times to light fires, hence its name is ultimately associated with the concept of fire.

It is found mainly in sedimentary rocks in oxygen-poor environments (e.g., organic-rich black mudrocks), but also in ores (e.g., porphyry copper deposits), intrusive mafic and ultramafic rocks (e.g., in association with ophiolite complexes), as large masses in skarn deposits formed by contact metamorphism, or in hydrothermal veins. In igneous rocks, pyrite can be found either disseminated or concentrated in layers. In addition, it often creates pyrite fossils by replacing shells and plant debris.

Although pyrite is widely used in the production of sulfuric acid [5], its economic value is lower compared to other commonly associated minerals such as chalcopyrite, galena, and sphalerite, although pyrite may locally carry gold dispersions [6]. Furthermore, pyrite is an indicator of mineral deposits, also helping geologists to determine the conditions under which sedimentary rocks were formed. Pyrite is a key mineral to understand Earth's climate change at geological scale, because it is involved in the global carbon, oxygen, and sulfur cycles [7–11].

In the past, the shiny, brassy-yellow color of pyrite lead people to mistakenly identify this mineral as genuine gold. For this reason, pyrite's nickname is "fool's gold". One anecdotal historical fact is found in 1608, when John Smith, following the orders of his captain Christopher Newport, purchased more than one thousand tons of sand from local Native American tribes, believing it to be laden with small fragments of gold. Unfortunately, he sent back to London an entire shipload of sedimentary pyrite. Another historical example is found in the Klondike region of the Yukon Territory, Canada, during the gold rush in the late 1980s. Many prospectors explored the northern wastelands in an attempt to seek their fortune by discovering gold

deposits. However, most of them had to deal with the numerous pyrite veins present, so the more experienced prospectors developed methods to differentiate gold from pyrite, such as color testing under different lighting conditions or even hardness evaluation.

Table 1.1. Physical properties of pyrite.

Transparency	Opaque
Luster	Metallic
Color	Brass-yellow
Streak	Greenish-black
Density	4.8-5.0 g.cm ⁻³
Hardness (Mohs)	6.0-6.5
Tenacity	Brittle
Cleavage	Poor indistinct
Fracture	Irregular, conchoidal

Other properties differentiate gold from pyrite. For instance, gold has a higher density than pyrite. Moreover, while gold is very malleable, allowing jewelers to shape it into fine ornaments, pyrite can easily crumble under pressure. Table 1.1 summarizes some of the most relevant physical properties of pyrite.

1.2 Chemical and crystal structure

It is composed of a ferrous cation (Fe^{2+}) and a disulfide anion (S_2^{2-}) in a Fe:S ratio of 1:2, though some slight (< 1%) stoichiometric deviations with respect to the cation or anion concentration have been reported. Lattice substitutions of Fe^{2+} or S^{2-} ions with endogenous cations or anions of similar radius and charge explain most of these deviations [12]. However, the presence of trace elements can also lead to the modification of some of its semi-conducting bulk properties, thus affecting the reactivity capacity of the surface [12,13].

Pyrite typically occurs in cubic or pentagonal dodecahedral (pyritohedral) morphologies, but also octahedral (less frequently). In many locations,

massive, granular or radiating pyrite is also present. Special mention is made to framboidal pyrite, brass-yellow in reflected light, which is also a common form. In cubic morphology, pyrite has the same crystal arrangement as halite (NaCl), where the center of the S-S bonds occupy the same positions as Cl⁻ ions and Fe²⁺ ions are placed in the same position as Na⁺ ions. However, cubic pyrite shows lower symmetry than halite because of the distorted octahedral arrangement of Fe²⁺ in coordination with six S atoms, each S being coordinated at the same time with one S and three Fe²⁺ in a distorted tetrahedral coordination [6].

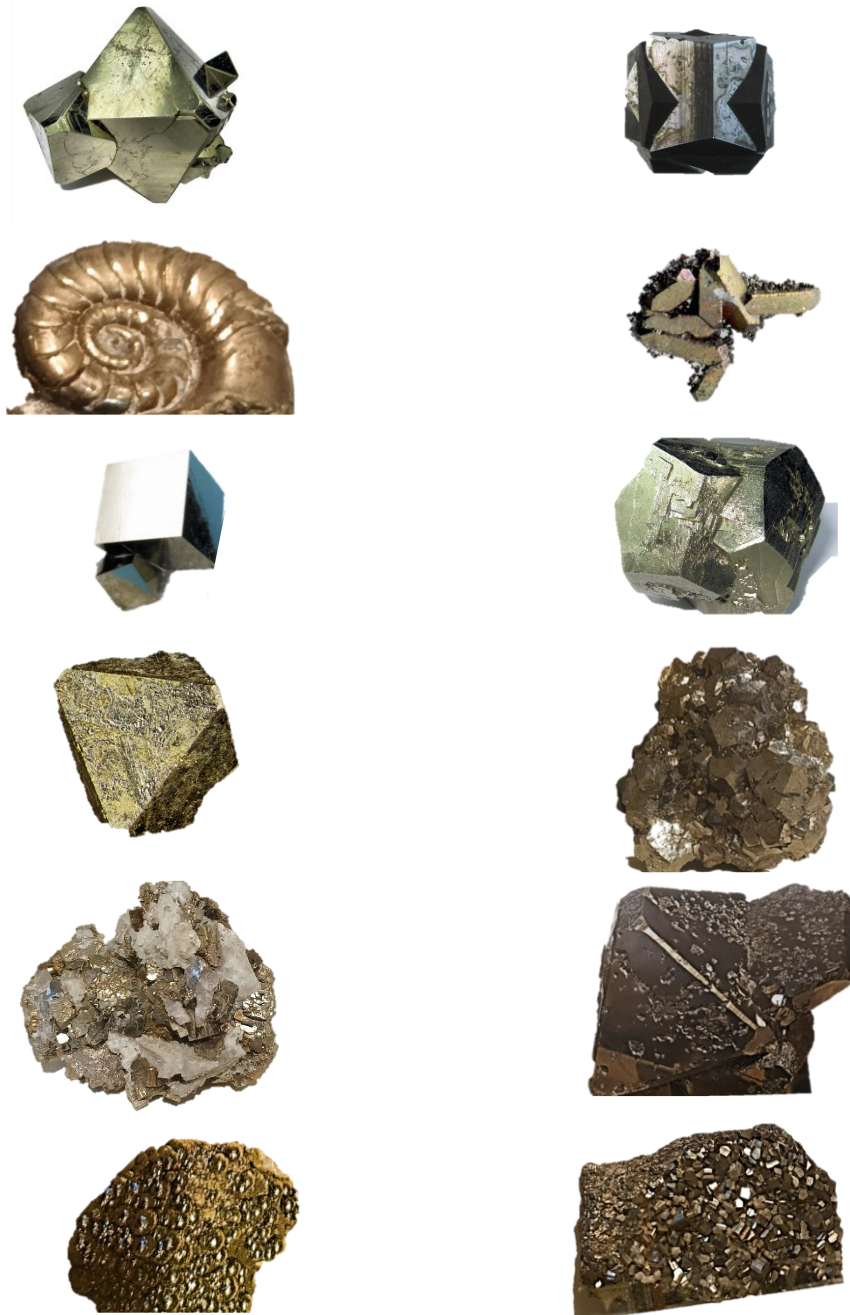


Figure 1.1. Some common crystallographic forms of pyrite found in nature.

In nature, pyrite can be even found in several combinations of morphologies, for instance as striated crystals resulting from the superposition of cubic and dodecahedral growth. Figure 1.1 shows some examples of pyrite samples found in nature showing different crystallographic forms.

Moreover, pyrite is the most common polymorph of FeS_2 by far, being more stable than orthorhombic marcasite. The occurrence of marcasite is much more restricted, commonly found near the surface of acidic settings, presumably formed at low temperatures. It can also be found in some mineral deposits, in sediments and as a groundwater precipitate shale and limestone [14–16]. Marcasite is even less stable than pyrite if exposed to air and moisture. Many marcasite samples stored as “pyrite” decomposed completely into a crumbly mass of yellowish iron sulfates, leaving a noticeable stain if, for example, a cloth or a paper tissue protected the sample, due to the sulfuric acid generated in the process.

If pyrite is hosted in quartz or calcite veins, it degrades to form iron oxides and/or hydroxides, typically in the form of limonite. The presence of these types of compounds is an indicator of gold and other valuable metals in the surroundings. In general, pyrite is an unstable mineral which easily oxidizes. It naturally contains traces of As, so it is also considered a source of this metal which leaches into ground-water if pyrite is exposed to air and water. This situation is typical during coal mining operations.

Chapter: Reactions

2

”

The internal machinery of life, the chemistry of the parts, is something beautiful. And it turns out that all life is interconnected with all other life.

— Richard P. Feynman

In general, pyrite formation requires low oxygen environments and reducing conditions, as well as iron and sulfur availability. It can be formed in different geological settings through different biological or abiotic processes. These formation mechanisms cause pyrite to adopt different morphologies.

Although pyrite has an opaque, pale brass-yellow/silver color when preserved and fresh, it darkens and tarnishes with prolonged exposure to oxygen (Figure 2.1), which is a symptom of its instability to oxidation in certain environments, transforming into different iron oxides minerals and releasing sulfuric acid, which contributes to the acidification of the environments. The oxidation of pyrite over time has had a crucial impact on planet earth's history.

This chapter will discuss the processes of pyrite formation and pyrite weathering, which will serve as the basis for the studies carried out in this thesis.



Figure 2.1. Partially oxidized pyrite sample. The reddish patina in some areas of the surface is a symptom of the formation of iron oxides.

2.1 Genesis

There are three main geological formation mechanisms of pyrite: metamorphism, hydrothermal process and sedimentary processes.

2.1.1 Metamorphic formation

Metamorphism is a geological process that involves changes in the mineralogy, texture and chemical composition of rocks when exposed to high pressure and temperature. Pyrite formed during this process provides valuable information and clues on historical events and metamorphic conditions of the host rocks. There are different types of metamorphic pyrite formation: prograde, retrograde, contact and regional metamorphism.

Prograde metamorphism. This process refers to the changes that rocks undergo when they are subjected to an increase in temperature (200-600°C) and pressure, a situation typical of deep burial and tectonic compression processes [17,18]. The presence of reducing fluids is fundamental, as they facilitate ion transportation and mineral reactions. The pH of these fluids ranges from neutral to slightly acidic [19]. If pyrite was already present, this can recrystallize into larger crystals with increased stability. However, if some iron minerals such as hematite or magnetite are accessible, they can react with sulfur-bearing fluids to form pyrite. Moreover, the release of carbon dioxide or water vapor molecules during the process promotes pyrite formation since this fact increases sulfur availability. Some examples of prograde metamorphic pyrite formation are found in the metapelites, i.e., metamorphosed clay-rich rocks (mudstones or shales) of the Scottish Highlands, and in the metamorphosed iron-rich rocks found in the Labrador trough, Canada.

Retrograde metamorphism. On the contrary, this process refers to the changes that rocks undergo when they are subjected to a decrease in temperature and pressure during uplift and exhumation. Here, fluids also facilitate pyrite formation but, in this process, oxidizing conditions are necessary. Pyrite re-growth occurs due to sulfur release by pyrrhotite [18]. The two dominant factors are the temperature range over which re-equilibration was maintained during this cooling event and the initial pyrite-pyrrhotite ratio. Some examples are the formation of pyrite in veins associated with reactivated faults and fractures and in rocks that have

regressed to greenschist facies conditions, common in the Appalachian Mountains.

Contact metamorphism. This type of metamorphism is caused by the intrusion of hot magma into the rocks and subsequent heating, which creates an aureole around the intrusion. During these processes, high temperatures are achieved (up to 800 °C), but relatively low pressures compared to prograde metamorphism. These magmatic fluids are rich in metals and volatile molecules which can infiltrate into the rocks. This intrusion creates reducing environments. The reaction with iron-bearing minerals in the host rocks forms pyrite. In addition, the heat accumulated in the intrusion can cause thermal metamorphism, while the sulfur and other metals introduced by the magmatic fluid can lead to the formation of pyrite [17–19]. Some examples are the pyrite formation in carbonate rocks, typically adjacent to granitic intrusions such as those of the southwestern United States, and the pyrite found in metamorphic aureoles around igneous intrusions within hornfels, which are contact metamorphosed shale.

Regional metamorphism. This type of metamorphism affects large areas of the crust, which is typically associated with orogeny [18]. This process can be originated in a wide range of temperatures and pressures, from low-grade (greenschist facies) to high-grade (amphibolite and granulite facies). Pyrite is generated by the reactions of sulfur and iron-bearing fluids. The release of volatiles during progressive metamorphism enhances pyrite stability. Some examples are the pyrite found in metamorphosed pelitic rocks such as those of the Alps and Himalayas and in volcanic rocks, in association with sulfide deposits.

2.1.2 Hydrothermal formation

In volcanically and magmatically active environments, hot mineral-rich fluids interact with rocks and flow through the earth's crust, leading to pyrite formation and deposition. Hydrothermal pyrite often shows distinct isotopic signatures compared to sedimentary pyrite, in addition to traces of elements such as cobalt, nickel, and arsenic, which may indicate hydrothermal formation. Pyrite produced in these environments is usually associated with other minerals such as chalcopyrite, sphalerite and galena. There are two systems in which pyrite can be formed: magmatic and seafloor hydrothermal systems.

Magmatic-hydrothermal systems. This process involves the circulation of hydrothermal fluids from magmatic rocks [20]. This type of system is typically associated with granites and porphyries, which are intrusive igneous rocks. The temperature of these systems is driven by the cooling of magma bodies, reaching high pressures and temperatures (from 300 to 500 °C). Fluids are rich in sulfur and metals such as iron, gold and copper, also releasing volatiles such as H₂S. The pH of these fluids is acidic to neutral, and the presence of sulfur species provides reducing properties. Pressure gradients make these fluids migrate through fractures and pore spaces. During migration, they start cooling and mixing with water or other subsurface fluids, which reduces the solubility of sulfur-metal complexes, leading to the precipitation of pyrite and other sulfide minerals in veins, stockworks, or disseminated patterns within the host rocks. One example is the porphyry copper deposit in the Andes, where pyrite is found associated with copper mineralization.

Seafloor-hydrothermal system. Also known as mid-ocean ridge systems or black smokers, involve the discharge of hot, mineral-rich fluids at the ocean floor, a situation associated with subduction zones and divergent plate boundaries [20–22]. In this deep-sea environment, high pressure and temperatures (up to 400 °C) are achieved, involving fluids rich in metals, sulfur and a high chloride content. The mechanism of pyrite formation is as follows: first, seawater infiltrates the oceanic crust, being heated by the underlying magma which generates metal leaching. Then, this hot metal-rich fluid ascends through fractures and porous zones. The encounter with cold seawater leads to fast cooling, which causes sulfide precipitation around hydrothermal vents, forming chimneys and massive sulfide deposits on the seafloor. Examples of this system include the black smoker vents along the mid-Atlantic Ridge and the East Pacific Rise and the ancient volcanogenic massive sulfide deposits such as those of the Iberian pyrite belt.

2.1.3 Sedimentary formation

Sedimentary pyrite formation is a crucial geochemical event that impacts the sulfur and iron cycles. Pyrite is formed in sedimentary basins through a series of complex interactions involving biological activity, organic matter, and mineral precipitation. The main source of pyrite is represented by sulfate-reducing microorganisms, which are ubiquitous on the planet and provide a set of enzymes to promote the oxidation of organic matter and the

production of pyrite and other metastable iron sulfides. Several processes can be distinguished: diagenetic, syngenetic, substitution and framboidal pyrite formation.

Diagenetic pyrite formation. This process is carried out during the early stages of sediment burial and compaction within the sedimentary column [23,24]. It is considered a post-depositional process that happens at low temperatures (<100 °C) and pressures, and it is caused by sulfate-reducing bacteria, so oxygen-depleted environments (anoxic) are essential. The second important factor is the availability of SO_4^{2-} and high levels of organic matter as a carbon source for microbial activity. The mechanism of pyrite formation is as follows: first, microbial decomposition of organic creates anoxic conditions as oxygen is being consumed, then sulfate-reducing bacteria provide a set of enzymes and use organic-matter as a carbon source to reduce SO_4^{2-} to S^{2-} in the form of hydrogen sulfide through an 8-electron mechanism [25,26]. Reactive iron from pore waters or detrital minerals reacts with S^{2-} to form FeS, which undergoes further reactions with sulfur to form pyrite and other metastable minerals. Some examples are the organic-rich marine sediments such as those found in modern continental shelves and ancient black shales like the Devonian-Mississippian black shales in North America, and the pyrite formation in coal beds, such as the Appalachian Basin.

Syngenetic pyrite formation. In this process, pyrite forms during the deposition of sediments. It is often found as fine-grained disseminations or nodules within sedimentary layers [23,27]. Anoxic conditions between the sediment-water interface are crucial, along with high levels of organic matter and a continuous supply of SO_4^{2-} from seawater or pore waters. The process is as follows: organic matter sinks into the water column, consuming oxygen. Then, sulfate-reducing bacteria produce S^{2-} . Finally, iron from hydrothermal sources or detrital iron reacts with S^{2-} to form pyrite within the sediments. Some examples are the sedimentary pyrite found in organic-rich black shales, such as the Permian Kupferschiefer in Germany or the pyrite formed alongside iron oxides in Precambrian banded-iron formations.

Replacement pyrite formation. Chemical reactions involving sulfide fluids replace pre-existing minerals in sedimentary rocks with pyrite [23]. The movement of these fluids through sedimentary rocks is key, as they

interact with carbonates and iron-bearing minerals such as hematite and magnetite. These chemical reactions lead to the dissolution of the original minerals and the precipitation of pyrite, which crystals grow retaining the shape of the replaced mineral. This is known as pseudomorphism. Some examples are the fossil replacement such as pyritized ammonites found in the Jurassic sediments of Lyme Regis, England and the concretions of pyrite found in some carboniferous of Europe and North America.

Framboidal pyrite formation. It refers to the formation of small spherical aggregates of microcrystals that resemble a raspberry. It is a common texture in most sedimentary pyrite [23,26,27]. As for the previous sedimentary processes, anoxic environments are key for microbial activity, along with the presence of organic matter, SO_4^{2-} and reacting iron. Sulfate-reducing bacteria create microenvironments where the reaction of S^{2-} and iron takes place, followed by nucleation of pyrite microcrystals and aggregation into spherical framboids. Framboidal pyrite can also increase in size and coalesce into more massive pyrite grains over time. Some examples are found in the fine-grained marine sediments of anoxic basins such as the Black Sea and in estuarine and deltaic sediments with high organic content, such as the Mississippi Delta.

2.2 Weathering processes

Mineral weathering is a fundamental geochemical process of the Earth's surface. In this process, minerals are decomposed and transformed into secondary minerals and dissolved ions, which influence soil formation, nutrient cycling, landscape evolution, and the global carbon, oxygen and sulfur cycle. There are different mechanisms and factors controlling mineral weathering, which can be physical, chemical or biologically mediated.

On the one hand, **physical weathering** consists of the decomposition of minerals and rocks into smaller fragments without modifying their chemical composition [28]. It can be originated by diverse phenomena: 1) water seeps through cracks in the rocks and minerals. After freezing, it increases in volume and the rocks break; 2) temperature fluctuations cause minerals to expand and contract, leading to the formation of cracks and eventual disintegration; 3) wind, water, ice or other rock particles promote rock

grinding, leading to the eventual abrasion of the surface; 4) rocks and minerals are detached in layers due to the release of pressure by erosion of overlying materials; 5) salt solutions penetrate into the pores and cracks of the rock. The pressure exerted by the salt crystals formed after the eventual evaporation of these solutions causes the disintegration of the material.

On the other hand, **chemical weathering** involves chemical reactions that change the composition of minerals, also leading to the generation of dissolved ions and secondary minerals [28,29]. Although most chemical weathering processes are complex mechanisms that depend on environmental conditions, they can be subdivided into several reaction types: 1) hydrolysis, where the reaction with water induces the breakdown of mineral structure and the formation of clay minerals; 2) oxidation, which involves the reaction with oxygen or other oxidant species, typically associated to iron-bearing minerals such as pyrite; 3) carbonation, the carbonic acid resulting from the dissolution of carbon dioxide in water leads to the dissolution of carbonate minerals; 4) hydration, which involves the incorporation of water molecules in the crystalline structure, causing weakening and the expansion of the mineral; 5) solution, where soluble minerals in water lead to the release of their respective ions in water.

Finally, **biological weathering** involves the actions of plants, animals, and microorganisms, which contribute to both physical and chemical weathering processes mentioned above [28,30]. Some examples are: 1) plant roots, which penetrate the cracks of rocks and minerals, exerting pressure and promoting the breakdown. In addition, they can produce organic acids that enhance chemical weathering; 2) microbial activity, mainly mediated by fungi and bacteria, which produce acids and chelating compounds that facilitate mineral dissolution. For instance, *Acidithiobacillus ferrooxidans* and *Leptospirillum ferrooxidans* catalyze the oxidation of Fe^{2+} to Fe^{3+} , accelerating the oxidation of pyrite; 3) the acids produced by lichen that chemically weather rock surfaces, facilitating mineral breakdown.

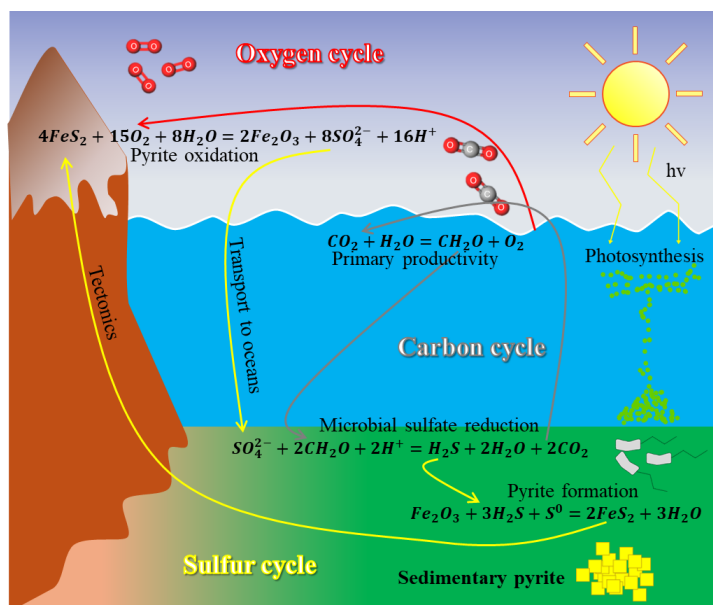
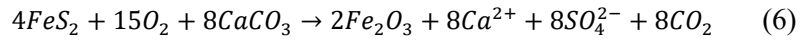
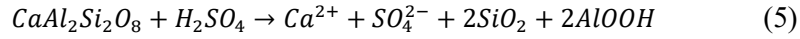
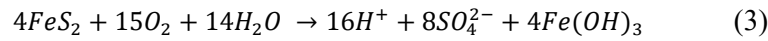
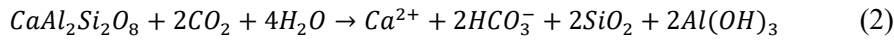
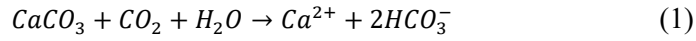


Figure 2.2. Pyrite's relationship with the sulfur, carbon and oxygen cycles.

The weathering of sulfide minerals such as pyrite is key in Earth's evolution, especially chemical weathering. However, pyrite weathering rarely occurs in natural environments through a single mechanism, but as a combination of oxidative, microbial and physical processes.

For instance, physical weathering exposes new surfaces, enhancing microbial weathering, which catalyzes pyrite oxidation, also known as *Oxidative Weathering of pyrite* (OWP) [13]. In particular, it should be highlighted that the oxidative weathering of sedimentary pyrite leads to the depletion of oxygen levels in the atmosphere. Therefore, pyrite plays a key role in the oxygen, sulfur and carbon cycle throughout the Earth's evolution [31], involving both pyrite formation and weathering, as illustrated in the scheme shown in Figure 2.2.

More specifically, the SO_4^{2-} generated during the OWP is linked to the carbonate and silicate weathering, which CO_2 consumption is thought to be responsible for short to long-term climate changes [32,33]. The reactions involved can be summarized as follows:



The carbonic acid generated by the dissolution of CO_2 in water leads to the weathering of carbonates (Eqn. 1) and silicates (Eqn. 2), thus converting atmospheric CO_2 into HCO_3^- . Moreover, pyrite oxidation (Eqn. 3) promotes sulfuric acid production which can also dissolve carbonates and silicates (Eqn. 4 and Eqn.5). Ultimately, the carbonate weathering promoted by OWP and the deposition of carbonates in the oceans result in a net release of CO_2 to the atmosphere (Eqn.6).

However, OWP is a very complex mechanism involving many reactions and pathways, depending on different factors.

2.2.1 Oxidative weathering of pyrite

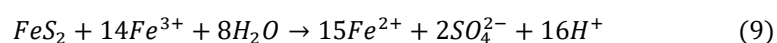
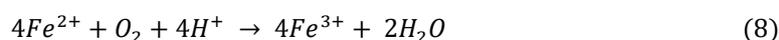
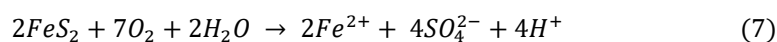
Pyrite oxidation is the main responsible for the acidification of natural waters. When OWP is caused by anthropogenic action, then is known as acid mine drainage (AMD). In addition, this process is economically important for two separation methodologies in the mining industry such as flotation and leaching, where pyrite must be separated from other valuable minerals. The interaction with the collector during flotation processes depends on the oxidation, which can impart hydrophilicity or hydrophobicity to pyrite surface [34]. If pyrite is not properly separated, the quality of the mineral concentrate is reduced and contamination with S, Fe and other As traces increases smelting costs [35]. During leaching, oxidation is the dominant process in the dissolution of pyrite [36]. An estimate of the daily costs in the mining industry for OWP treatment and the resulting acidification of the environment is more than \$1 million in the United States [37].

As mentioned before, the formulation of a detailed pyrite oxidation mechanism must include fundamental aspects such as the identification of the rate-limiting species and rate-limiting steps. In addition, considerations regarding water chemistry, surface and microbial catalysis should be

addressed both for weathered and fresh pyrite, including reaction intermediate species and surface-solution interface modelling. Although OWP has been studied for decades, there is still a lack of consensus on many of these aspects, in addition to the electrochemical or pure chemical nature of OWP. Nevertheless, some agreements have been reached on abiotic pyrite oxidation.

On the one hand, **atmospheric oxidation** generates products and intermediates such as polysulfides (S_n^{2-}), sulfates and iron oxy-hydroxide ($FeOOH$) species [38–40]. The surface is progressively being covered by an oxidation patina which can prevent further oxidation. The reactivity at the surface level of freshly fractured samples depends on the availability of the different species involved. Moreover, the pyrite cleavage can lead to the reduction of S:Fe stoichiometry of 2:1 due to the loss of S, which generates electronic differences between the surface and the core [41]. Although SO_4^{2-} is considered the main weathering product, followed by iron oxy-hydroxide species, there is still debate on the production of elemental sulfur and polysulfides [42]. Atmospheric oxidation begins after minutes of being exposed to air, starting with the oxidation of S^{2-} species. Complete oxidation to SO_4^{2-} is achieved even when the exposition to the atmosphere is limited. However, the rate of oxidation in moist air decreases with time, motivated by the formation of a ferrous sulfate thin patina that retards oxygen transport, which makes the reaction rate controlled by oxygen diffusion through this layer [43].

On the other hand, **aqueous oxidation** is faster than atmospheric oxidation and involves not only chemical, but also electrochemical and bacterial (*T.ferrooxidans*) catalysis pathways [44,45]. This type of oxidation mainly releases SO_4^{2-} and Fe^{3+} into the solution. Calcareous or acidic environments may lead to the formation of additional weathering products such as elemental sulfur, polysulfides (S_n^{2-}), iron oxides such as Fe_3O_4 or Fe_2O_3 , oxy-hydroxides, SO_3^{2-} , polythionates ($S_xO_6^{2-}$), H_2S and thiosulfates ($S_2O_3^{2-}$). The main reactions can be summarized as follows:



In the beginning, oxygen is the main oxidant present in water, which initiates pyrite oxidation (Eqn. 7). Then, the released ferrous iron oxidizes into ferric iron (Eqn. 8). As ferric iron is a more efficient oxidant agent than oxygen [39,46,47], pyrite preferentially oxidizes with this oxidant, also producing sulfate and ferrous iron (Eqn. 9). These reactions are far from equilibrium and have no reverse rate. In some studies, the oxidation rate at low pH due to Fe^{3+} was two orders of magnitude higher than oxidation promoted by dissolved oxygen [46]. However, oxygen is important to replenish ferric iron depletion through Eqn. 8. Other studies evaluated pyrite oxidation by hydrogen peroxide, observing an initial rate of H_2O_2 consumption doubling the rate of total iron production, which implies the catalytic H_2O_2 decomposition by Fe^{3+} [39]. The same study reported that reactive sites of pyrite surface such as corners, crystal edges, crystalline defects, cleavages and fractures are more relevant in determining the rates of reaction than the total surface, which may lead to consider the morphology as an important factor in aqueous OWP. Moreover, other studies highlight that under alkaline to neutral conditions, the precipitation of dissolved Fe occurs, as oxidant diffusion is retarded by coatings of goethite on the pyrite surface [48,49], so the assessment of pyrite alteration products on the surface is fundamental to understand pyrite persistence, especially in the sedimentary records.

Part II

Instrumentation and data analysis methods

Chapter: Instrumentation | 3

” *If a machine is expected to be infallible, it cannot also be intelligent*

— Alan Turing

In the present thesis, several analytical methods have been applied for the assessment of pyrite and its weathering products. In particular, Raman spectroscopy has been used as the main analytical tool for the mineralogical characterization of pyrite and other minerals related to the oxidative weathering process. Some of the contributions of the thesis have been the development of characterization methods based on Hyperspectral Raman imaging. Compared to traditional single-point Raman analysis, this approach allows for the spatial assessment of the pyrite surface, providing a better understanding of the chemical transformation that weathered pyrite undergoes. Two specific studies using hyperspectral Raman imaging will be described in the following chapters. The data analysis methods applied to these images in these studies demonstrate the potential of this type of spectroscopic analysis, serving also as a basis for future studies applied to other minerals or challenges.

In addition, Scanning Electron Microscopy - X-Ray Energy Dispersive Spectroscopy was used for elemental analysis of the sedimentary pyrite from Luye (Taiwan) to test whether these samples had traces of other elements in their composition. On the other hand, inductively coupled plasma optical emission spectroscopy and ion chromatography were used for the quantitative analysis of metallic elements and anions in solution, which helped to better understand the importance of the chemical composition of water in the oxidative process of pyrite. Finally, a high-performance liquid chromatography method was developed for the quantification of elemental sulfur extracted as a proxy for the weathering evaluation in acidic environments.

3.1 Raman spectroscopy

The Raman effect was discovered in 1928 by Indian physicist C.V. Raman. He observed that when light interacts with some molecules, a small fraction of the dispersed radiation is shifted in wavelength. The discovery of this effect earned him the Nobel Prize in Physics in 1930. This effect is also known as Raman scattering

The Raman Effect emerges from the interaction between electromagnetic radiation and matter. More specifically, when a sample is irradiated with visible or infrared monochromatic radiation of energy $h\nu$, most of the light is elastically scattered, meaning that the energy of the emitted photons is the same as that of the excitation radiation, resulting in no wavelength shift. This is known as Rayleigh scattering. However, when a small fraction of photons exchange energy with the molecule's vibrational or rotational states, a wavelength shift occurs, which is known as inelastic or Raman scattering. There are two possible situations: 1) molecules at a fundamental vibrational level ($\nu=0$) absorb a photon and then emit a photon of lower energy. In this case, the emitted radiation results in a shift to longer wavelengths than the excitation radiation, which is called *Stokes* Raman scattering; 2) molecules in an excited vibrational state ($\nu=1$) emit a photon of higher energy, which results in a shift to shorter wavelengths, which is called *Anti-Stokes* Raman scattering. These processes are depicted in Figure 3.1 a. The wavelength shift of the inelastically scattered radiation provides a molecular fingerprint unique to the specific chemical bonds and symmetry of the molecules and is the basis of Raman spectroscopy [50–52]. As the Stokes lines of a spectrum have higher intensity than the anti-Stokes lines due to the number of molecules in a fundamental vibrational level, only Stokes lines of a spectrum are used in Raman spectroscopy. These peak shifts are expressed as wavenumbers (cm^{-1}). However, anti-Stokes lines are specifically used when molecules are prone to emit fluorescence, as this is less likely to interfere, compared to Stokes lines. This phenomenon is governed by quantum mechanics, where the molecule temporarily enters a virtual energy state before re-emitting a scattered photon.

A Raman spectrum is often referred to as a molecular fingerprint because it uniquely reflects the vibrational and rotational characteristics of a molecule's structure. These characteristics depend on the specific

arrangement of atoms, bond lengths, angles, and symmetry. When light interacts with a molecule, the inelastic scattering captured in the Raman spectrum reveals distinct spectral lines, each corresponding to a particular vibrational energy transition. This unique spectral pattern allows for the identification and differentiation of molecules, even in complex mixtures, as no two compounds produce identical Raman spectra under identical conditions.

Polarizability plays a central role in Raman spectroscopy. It describes the ease with which a molecule's electron cloud can be distorted by an external electric field, such as the oscillating field of incident light. Vibrational modes that induce a change in the polarizability of the molecule are classified as Raman-active. For instance, symmetric stretching significantly alters the electron cloud, which typically generates a strong Raman signal. Conversely, an asymmetric stretch or bending vibration might not sufficiently change the polarizability and may be Raman-inactive.

The selection rules for Raman activity depend on changes in the polarizability tensor of a molecule during vibration. A vibrational mode is Raman-active if the polarizability of the molecule changes along at least one axis during the vibration. This differs from infrared (IR) spectroscopy, where a vibrational mode is active only if it induces a change in the molecule's dipole moment. In centrosymmetric molecules, vibrational modes that are Raman-active are generally IR-inactive and vice versa, a phenomenon known as mutual exclusion.

In solids, vibrational modes manifest as phonons, which represent quantized lattice vibrations. These modes can be categorized into (a) optical phonons, which involve relative motion of atoms within the crystal lattice basis and are typically Raman-active or (b) acoustic phonons, which represent collective lattice vibrations and are generally Raman-inactive unless altered by strain or other effects. The Raman spectrum of a solid provides direct insights into these phonons, enabling analysis of the crystal structure, bonding properties, and lattice dynamics.

The symmetry of molecules or crystals determines the Raman activity of its vibrational modes. Group theory classifies these modes based on molecular or lattice symmetry. Phonon symmetry properties are described using the irreducible representations of the crystal's point group, i.e., in highly

symmetric crystals, such as cubic systems, certain phonon modes may or may not exhibit Raman activity depending on their symmetry. The determination of Raman activity relies on selection rules derived from symmetry operations like rotations, reflections, and inversions. Mulliken notation provides a systematic way to label the irreducible representations of symmetry groups in molecules and crystals, facilitating the description of vibrational modes. On the one hand, *singly* degenerate modes are denoted by A or B (symmetric/asymmetric), while *doubly* and *triply* degenerate modes are denoted by E and T, respectively. Subscripts such as *gerade* (g) and *ungerade* (u) reflect symmetric or antisymmetric behavior under inversion.

On the other hand, the position and width of Raman bands are influenced by various intrinsic and extrinsic factors: 1) atomic mass, since heavier atoms vibrate more slowly, leading to lower wavenumbers in the Raman spectrum; 2) bonding strength, since stronger bonds, such as triple bonds, result in higher vibrational frequencies and higher wavenumbers; 3) symmetry, since high-symmetry environments yield sharper, more intense Raman peaks due to well-defined selection rules; 4) strain, since mechanical strain in solids shifts phonon frequencies, altering Raman band positions and broadening peaks; 5) disorder, since structural disorder in crystals diminishes vibrational coherence, causing peak broadening and reduced intensity; 6) crystalline defects, since vacancies, point defects, or substitutions in a lattice introduce localized vibrational modes or modify existing phonons, altering the spectrum; 7) size effects, since in nanomaterials, phonon confinement causes shifts and broadening of Raman peaks, e.g., smaller nanoparticles often exhibit redshifts and asymmetric peaks due to reduced phonon coherence lengths.

Therefore, a Raman spectrometer (Figure 3.1 b) is a powerful analytical instrument used to provide detailed information about molecular vibrations and crystal structures, making it invaluable in both academic research and industrial applications because it is a fast and non-destructive technique that does not require sample preparation.

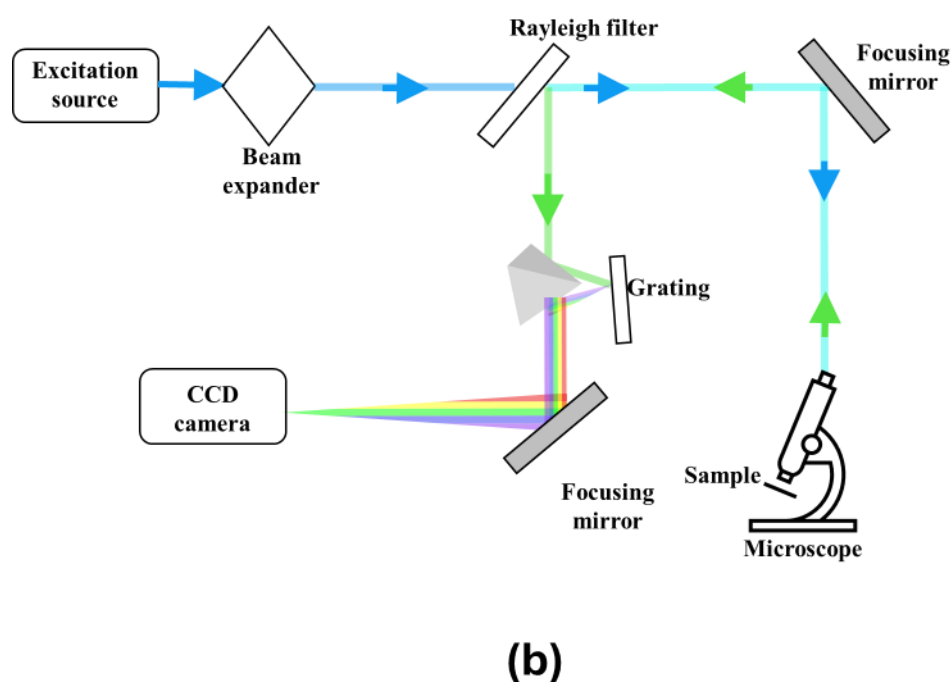
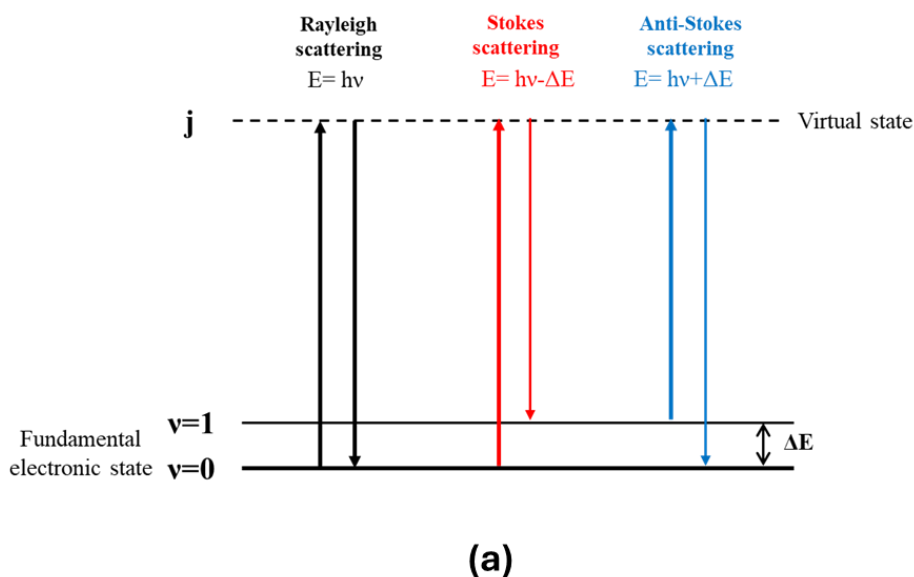


Figure 3.1. (a) Raman effect and (b) scheme of a Raman spectrometer.

Raman spectroscopy has been widely used in many fields of knowledge, such as biology, medicine, material science, environmental sciences and chemistry and it can be applied to the measurement of solid, liquid and gas samples. In particular, there are abundant examples in the literature on the use of Raman spectroscopy as a tool for the characterization of pyrite and related samples [53–59].

3.1.1 Hyperspectral imaging

For solid samples, the laser spot of the instrument covers a certain area of the sample, which depends on the type of laser and the magnification used. Table 3.1 summarizes the theoretical diameter of the spot of the laser. The spectrum of a single acquisition will include only the vibrational modes of the molecules within the area covered. As can be imagined, a homogeneous surface (chemically speaking) can be characterized with only a few acquisitions, which in general can be performed quickly and with good spectral quality, depending on the laser power used, the number of acquisitions per analysis point and the exposure time.

Table 3.1. Theoretical diameter (μm) of the spot of the laser depending on the magnification and the monochromatic radiation employed.

	5x	20x	50x	100x
532 nm	5.226	1.568	0.836	0.784
633nm	7.981	2.394	1.277	1.197
785 nm	6.436	1.931	1.03	0.965

However, single-point analysis is not a viable way to operate if adequate surface characterization of heterogeneous samples is required. In the present thesis, this is an important limitation since the characterization of partially to completely weathered pyrite samples is essential. The traditional approach during mineral analysis starts with a visual evaluation of the sample (e.g., optical microscope in reflected light for opaque minerals), which requires the expertise of an operator to recognize different mineralogical phases. Then, single-point analyses are performed on the different mineralogical phases of the surface. Nevertheless, this approach presents some obvious limitations, as the conclusions derived from this type of analysis are not representative enough of the entire surface under study. Thus, for the study of pyrite and its weathering products, a different approach must be followed to gain better knowledge of the distribution of alteration features on the surface and to link sample morphology with oxidation mechanisms.

In this regard, the technology of many spectroscopic devices has evolved to provide a solution to overcome the limitations of single-point analysis: *Hyperspectral Imaging* (HSI), which refers to the acquisition of spectral images. In traditional RGB images, each pixel is composed of three discrete

values or channels, corresponding to specific wavelengths of the visible spectrum, i.e. red, green and blue. On the contrary, each pixel of a hyperspectral image contains a multitude of channels corresponding to the nature of the electromagnetic radiation effect, e.g. ultraviolet-visible, Raman, fluorescence, near or mid-infrared. Applied to Raman spectroscopy, it is possible to scan a surface area of a sample and obtain an image in which each pixel contains a spectrum [60].

The data generated after the acquisition of each hyperspectral image is organized in a three-dimensional data array as shown in Figure 3.2. The first two are spatial dimensions (X-Y coordinates of each pixel) and the third is the spectral dimension (λ). The size of the resulting image depends on several parameters: 1) spatial resolution, i.e., the distance between the midpoint of the area covered by the laser spot during the first acquisition and the next point covered after moving the laser position; 2) the spectral region acquired, e.g., from 200 to 1200 cm^{-1} ; 3) the spectral resolution, i.e. the gap between the wavenumber value of one Stokes line and the next one.

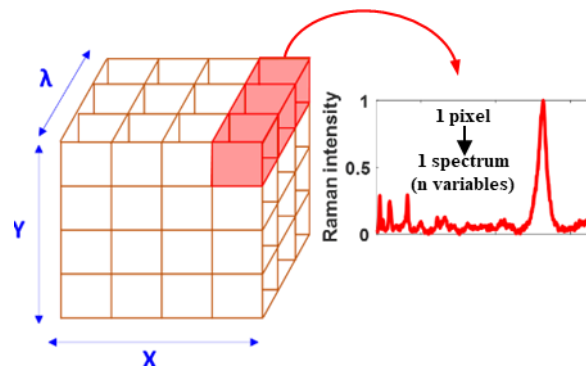


Figure 3.2. Three-dimensional data array of a hyperspectral image.

In general, the amount of data included in one single hyperspectral image is huge. For this reason, the application of multivariate data analysis methods has become essential, as will be explained in Chapter 4.

Although many recent studies employ HSI in a multitude of fields, there are few examples for the analysis of sulfide minerals at macro- (satellite imagery) or micro-scale [61–64]

3.2 Scanning Electron Microscopy-X-Ray Energy Dispersive Spectroscopy (SEM-EDS)

This analytical technique provides qualitative and quantitative information on the surface morphology and elemental composition of materials [65]. First, the microscope part is used to scan the surface with a primary electron beam to obtain high-resolution black-and-white images. These images generated thanks to the detection of the secondary and/or backscattered electrons emitted (Figure 3.3), allow us to study the morphology of the sample and to check for different microcrystalline structures. Secondary electrons are elastically emitted when the incident beam collides with the sample. Generated images include contrast topographic information, which is useful to have an overall image of the surface shape. Backscattered electrons have energy lower than 50 eV and are emitted by inelastic collision of the beam with the sample. The images based on backscattered electrons generate contrast zones whose brightness varies in proportion to the atomic weight of the elements that form the different crystalline zones of the sample. The magnifying power of the most advanced devices can be as high as 100,000 times and spatial resolution up to 1 nm.

Then, a primary electron beam of high intensity is focused on the regions of interest resulting in the ejection of inner-shell electrons from the atoms present in the sample. This causes characteristic X-ray emission as electrons from higher energy levels fill the vacancies (Figure 3.3). The emitted X-rays have specific energies that correspond to the difference between the energy levels characteristic of the elements in the sample. Finally, an EDS detector measures the energy of the emitted X-rays to produce a spectrum in which each of the peaks corresponds to one of the elements presents in the sample.

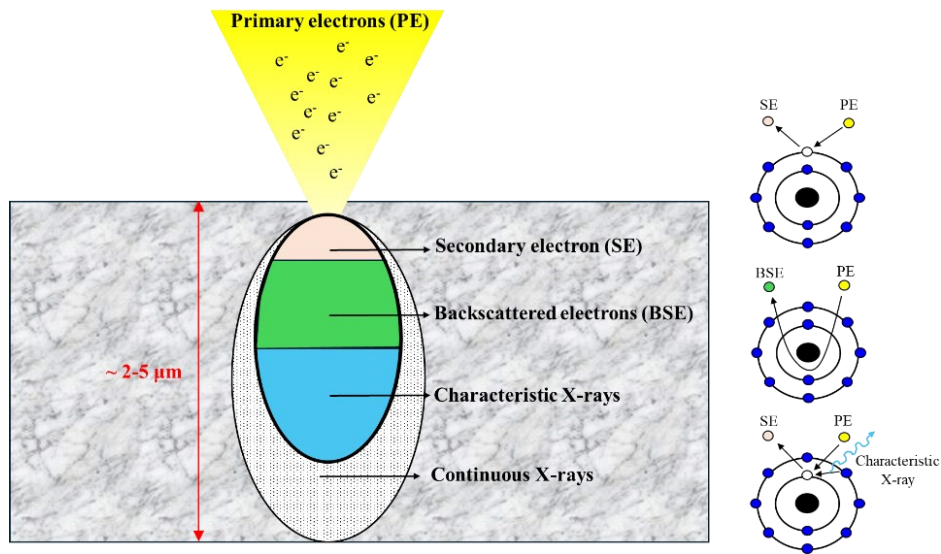


Figure 3.3. Principles of SEM-EDS.

As in Raman, the information collected by the EDS detector allows not only point analysis, but also the possibility of scanning a specific area of the sample, generating hyperspectral images. In this case, the spectral direction (λ) of the generated data matrix does not contain a continuous spectrum, but discrete values in each of the channels referring to the number of counts per second (cps/eV) of each of the elements present.

This technology has been widely used in many fields related to the analysis of solid materials. In particular, there are many examples of the application of SEM-EDS for the analysis of pyrite in diverse contexts [66–72].

3.3 Inductively Coupled Plasma Optical Emission Spectroscopy (ICP OES)

This analytical technique is used for the analysis of the chemical composition of liquid samples [65]. First, the sample is transformed into a fine aerosol in the nebulizer using a stream of argon gas. The aerosol is passed through the spray chamber which removes larger droplets. An argon carrier gas transports the aerosol into an argon plasma torch which is extremely hot (10000 K). The atoms and ions then absorb this heat energy, which causes the displacement of some electrons from the ground state to an excited state. Afterwards, during the transition of the excited electron to

the ground state, electromagnetic radiation of a very specific wavelength is emitted. The emission depends on the element and the energy difference between the excited state and the ground state, as shown in Figure 3.4. The analyzer's optical system catches the light generated and separates it into different emission spectral lines which are recorded in the detector.

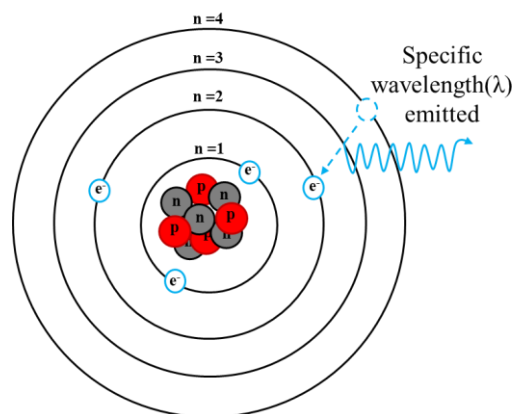


Figure 3.4. Principles of ICP OES.

The light emitted by an element can have different wavelengths, although there are more likely transitions and, therefore, the intensities will be different. Some emission lines of an atom may interfere with the emission lines of some elements. The measurement of the amount of emitted light at each wavelength can be used to calculate the concentration of the different elements in the sample.

Some of the advantages of this technique are the ability to detect elements simultaneously and the speed of analysis. It presents a wide dynamic range and high precision, being able to detect trace elements. It is widely utilized in various fields such as environmental monitoring for the monitoring of heavy metals in air, water and soils [73,74], in the food industry for the detection of contaminants and adulterants [75,76], in the pharmaceutical industry for quality control and toxicity evaluation [77,78] and in geochemistry for the analysis of mineral content, metal ores and heavy metals in soils [79,80].

3.4 Chromatographic methods

In general, chromatographic methods are analytical techniques used for the separation, identification and quantification of molecules within a complex

mixture [81]. These techniques exploit different properties of the molecules to be separated such as the charge, the size, the hydrophobicity or the specific affinity for a stationary phase. The sample to be analyzed is brought into contact with a mobile phase or eluent. The generated flow is passed through a stationary phase where the molecules will travel at different rates, thus achieving separation.

There are different chromatographic techniques based on the nature of the mobile and stationary phases and the mechanism of separation. The major chromatography categories are gas chromatography (GC) and liquid chromatography (LC).

3.4.1 Ion chromatography (IC)

Ion chromatography is a liquid chromatography technique used for the separation and analysis of anions and cations [65]. In this technique, columns with ion-exchange resins are used as the stationary phase. The mobile phase is typically composed of aqueous solutions with varying ionic strength or pH. The separation is achieved based on the ion exchange equilibrium of the ions interacting with the ion exchange sites of the resin. Once the different ions are separated, they leave the column and pass through the detector system, which measures each of the signals based on different properties. In liquid chromatography, the most commonly used detectors measure UV-Vis absorption, fluorescence, conductivity or are coupled systems such as mass spectrometers. IC typically uses conductivity detectors. There are many examples in the literature on the use of ion chromatography. In particular, this technique has been used in many studies for the analysis of different ionic species related to the oxidation of sulfide minerals [82–87].

3.4.2 High-performance Liquid Chromatography (HPLC)

This is a versatile and widely used technique for separating, identifying, and quantifying molecules in a liquid sample [65]. The technique involves the use of a mobile phase that carries the sample through a column packed with a stationary phase. The separation of components is based on the polarity of the molecules and the interaction with the mobile and stationary phases. Depending on the solvent or solvent mixture used as mobile phase and the material packed in the column, there are two main types of HPLC methods:

1) *normal-phase HPLC*, in which the column is polar, and the mobile phase is non-polar; 2) *reversed-phase HPLC*, in which the stationary phase is non-polar and the mobile phase is polar. This is the most common type of HPLC. One of the most used detectors is the Diode Array Detector (DAD), which allows simultaneous detection and quantification of the analytes leaving the column based on the light absorption at certain wavelengths within the UV-Vis range. Other detectors are the fluorescence detector, which measures the fluorescence emitted by certain molecules when exposed to excitation light and the coupling with a mass-spectrometer.

As in the case of IC, there are many examples in the literature on the use of HPLC in geochemistry for the study of sulfide minerals [88–92].

Chapter: Data analysis methods

4

The world is generally multivariate.

”

— Edward Tufte

In many areas of knowledge, experiments that evaluate the impact of multiple variables on a process, property or material feature are still performed following the traditional *one-variable-at-a-time approach*. This approach is often time-consuming and labor-intensive. In contrast, data-driven experiment planning allows us to assess which variables are significant and how they are correlated, as well as to quantify their impact on the desired response. Once the significant variables have been identified, the next objective is to find their optimal values to minimize or maximize that response.

In addition, the flood of data generated by modern analytical tools requires data analysis approaches focused on multivariate statistics to manage, process and extract useful information, which is no longer feasible today with a univariate approach. In this regard, in 1974, Svante Wold and Bruce Kowalski founded the International Chemometrics Society, which defined the word “Chemometrics” as “*a chemical discipline that uses mathematical and statistical methods to design/select optimal procedures and experiments, provide maximum chemical information by analyzing the data, and give a graphical representation of this information, in other words, information aspects of chemistry*”. Nowadays, this is not a discipline exclusive to chemistry, and society knows it by other names, such as “pattern recognition” or “machine learning” methods.

The analysis of the data generated in the studies carried out in the thesis could be divided in two different scenarios: 1) data-driven design and planning of laboratory experiments to extract as much valuable information as possible about the important factors affecting OWP; 2) multivariate analysis of the outcomes of the analytical techniques applied. This chapter provides a brief explanation of the multivariate methods applied in the thesis to address these two scenarios.

4.1 Experimental design

Design of experiments (DoE) is a statistical approach to conduct a series of unique experiments by varying all the variables under study simultaneously [93,94]. Based on mathematical principles, each of the experiments is scheduled from the beginning following some rules. Once the experiments are completed, the information generated is used to calculate regression models to evaluate the significant variables and the nature of their influence. Depending on the objective, several experimental designs can be applied. At this point, it is important to define some terms:

Response. property (y) linked to the quality or performance of the system under evaluation.

Factors. These are the k variables ($x_1, x_2, x_3, \dots, x_k$) that are modified in each experiment. The factors analyzed may influence the response to a greater or lesser extent.

Level. Refers to the different values that a factor can adopt during the experiments.

Experimental domain. Refers to the space in which the factors vary. It is usually defined by the maximum and minimum levels allowed for each factor.

Experimental run. Often defined simply as “experiment”, refers to a single measure of the response after imposing values for the k factors, which defines a point within the experimental domain.

Experimental design. Refers to specific arrangements of N experimental runs in the experimental domain. Depending on the objective, there are multiple experimental designs, each with its own advantages and limitations. They can be divided into *screening* and *optimization* designs.

Replicates. Experimental runs conducted where the values of the k factors are identical.

Model. It refers to the mathematical relationship between factors and response, calculated empirically from experimental data:

$$y = f(x_1, x_2, x_3, \dots, x_k)$$

Normally, DoE is divided into a series of steps that must be followed in an orderly fashion [95–97]:

1. **Definition of the analytical problem.** This is a crucial step that must be carefully addressed. First, the response/s able to provide information on the system under study is/are chosen. Then the objective must be established, i.e., a screening of the relevant factors or the optimization of those factors to maximize or minimize the response. In this regard, some restrictions or limits may have to be imposed on the response. Finally, the factors to be evaluated must be chosen on the basis of previous experimental information, i.e., all the factors that may affect the response, considering also the possible interaction or not that they may present.
2. **Planning the experiments.** Based on the information gathered so far, an appropriate experimental design must be chosen, also taking into account the quality of the information to be provided and the number of experiments required.
3. **Execution of experiments.** Following the experimental plan, experiments are conducted in the laboratory trying to avoid external sources of error not considered in DoE. In general, a good standard procedure is to run the experimental plan in random order, also measuring the responses in the same conditions.
4. **Modelling and data analysis.** Regression models are calculated to quantitatively weigh the significance of each factor (also known as coefficients or model parameters) and the negative or positive influence on the response. A factor is considered significant when its range of variation leads to a variation of the response greater than the experimental error. Then, the quality of the model must be evaluated by estimation of experimental error, model precision, uncertainty, validity domain, etc... If model performance is satisfactory, it can be used to predict the response within the experimental domain.

4.1.1 Screening designs

If the objective is the identification of the most important factors for a certain response, then a suitable experimental design for this objective must be selected during the definition of the analytical problem step. This is very important if, for example, there are a large number of factors that can affect the response. Screening designs are based on the Pareto principle, i.e., the effect on 80% of a given response is caused by 20% of the factors above the noise threshold. The strategy of these designs consists of varying all the factors at the same time, obtaining the desired information in a reduced number of experiments [98]. Depending on the number of factors and the need or not to evaluate the interaction between factors, screening designs can be subdivided into factorial, fractional factorial and Plackett-Burman designs.

Contrary to the univariate approach in which each factor is considered independent and where the effect of each factor on the response does not depend on the other factors, multivariate regression models use different polynomials according to the nature of the relationship between factors and response, i.e., linear, interaction or quadratic. In its simplest form (Ordinary Least Squares regression), this relationship is modelled as:

$$y = \beta_0 + \beta_1 x_1 + \beta_2 x_2 + \dots + \beta_k x_k + \varepsilon$$

where y is the response, x_k is the k factors, β_0 is the intercept term, β_k the coefficient for the k factor and ε is the residual response not explained by the model. For experimental designs that evaluate interactions between factors, additional terms should be included in the polynomial, such as $\beta_{12} x_1 x_2$, which expresses the interaction between factors x_1 and x_2 . The models are usually calculated by means of multiple linear least-squares regression (MLR).

4.1.2 Plackett-Burman design

For screening a large number of factors and estimating their main effects, Plackett-Burman designs [99], which are considered a class of fractional factorial designs, are useful. However, it must be assumed that the interaction between factors and quadratic effects are negligible, so they are advisable for linear regression.

These are two-level orthogonal designs, which means that each factor is analyzed on 2 levels. The number of experiments (N) required is the first multiple of four greater than the number of factors. However, it is advisable to perform more experiments to increase the number of degrees of freedom available for the estimation of the experimental variance. The experimental matrix that determines the level of each factor on each experimental run is built by cyclic permutation. Table 4.1 contains an example of a Plackett-Burman design for 7 variables.

Table 4.1. Plackett-Burman experimental matrix. Maximum and minimum levels are denoted by “+” and “-”, respectively. The number of degrees of liberty is $12-7-1=4$.

		Factors						
		A	B	C	D	E	F	G
Experimental runs	1	+	-	+	-	-	-	+
	2	+	+	-	+	-	-	-
	3	-	+	+	-	+	-	-
	4	+	-	+	+	-	+	-
	5	+	+	-	+	+	-	+
	6	+	+	+	-	+	+	-
	7	-	+	+	+	-	+	+
	8	-	-	+	+	+	-	+
	9	-	-	-	+	+	+	-
	10	+	-	-	-	+	+	+
	11	-	+	-	-	-	+	+
	12	-	-	-	-	-	-	-

A way of estimating the experimental variance is to add new columns to the design up to N-1 columns (using the available degrees of freedom). These additional columns represent *dummy factors* which are associated with non-significant effects and noise. To assess whether a factor is significant or not, the coefficients of the dummy factors can be used qualitatively, by comparing the absolute value with respect to those of the experimental factors.

4.2 Multivariate analysis

Before analyzing the data, a good starting point is to conduct a pre-processing step by performing mathematic operations in order to deal with different scales, measurement units or to minimize undesired random or systematic variations.

Different multivariate methods can help address different problems in chemistry, such as the exploration of the data generated by an instrument, classification or discrimination of different samples or prediction of a property by regression modelling.

4.2.1 Data pre-processing

Preprocessing is perhaps the most important stage of multivariate analysis due to the effect it has on the data and on the quality of the information that can be obtained [100]. These operations can be performed by rows or by columns, so that, once the data have been acquired, it is essential to organize them in a matrix, where each row normally corresponds to a sample and each column to a variable. For many data-analysis methods, it is necessary to apply scaling in order to remove the effects of the scale or units from the variables. In this way, the different variables become comparable, so that the variance no longer depends on their scale. Scaling approaches are commonly applied to the columns (e.g. elemental composition data) whereas other operations are applied to the rows (e.g. spectral data). Some of the most applied pre-processing operations are:

Mean centering. The mean value of each variable is calculated and then subtracted from each individual value. This approach centers the data in the space origin without changing the variance:

$$x'_{ij} = x_{ij} - \bar{x}_j$$

where i refers to the i -th row and j to the j -th column.

Autoscaling. Like mean centering but dividing by the standard deviation S , so it performs variance normalization. Is typically applied when the variables have different units of measure:

$$x'_{ij} = \frac{x_{ij} - \bar{x}_j}{S_j}$$

Min-max scaling. It transforms the data into a specific range, typically from 0 to 1. It is useful to interpret variables on the same scale:

$$x'_{ij} = \frac{x_{ij} - \min(x_j)}{\max(x_j) - \min(x_j)}$$

Standard Normal Variate (SNV). Reduces data dispersion between signals from different samples. Commonly applied to continuous data such as spectral data to deal with additive scattering effects without changing the shape of the spectrum. Like autoscaling but applied in the row direction. An example of SNV scaling is shown in Figure 4.1.

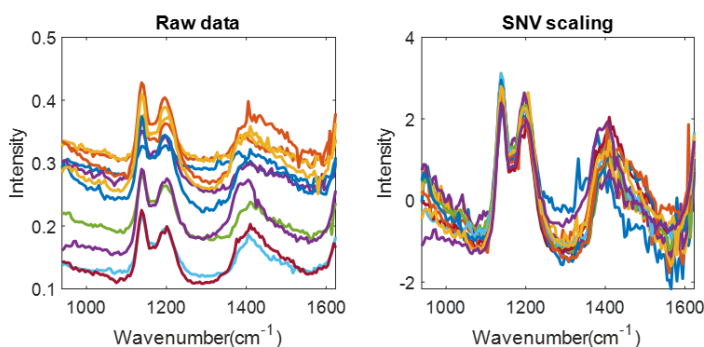


Figure 4.1. SNV applied on several Raman spectra.

Baseline correction. Useful to eliminate systematic deviations due to variations in the analytical instruments such as drift between spectra of different samples. There are many methods such as global polynomial, local polynomial or non-quadratic cost function minimization, which usually perform better but require the imposition of several parameters such as the type of cost function, the threshold and the order of the polynomial. An example of baseline correction is shown in Figure 4.2.

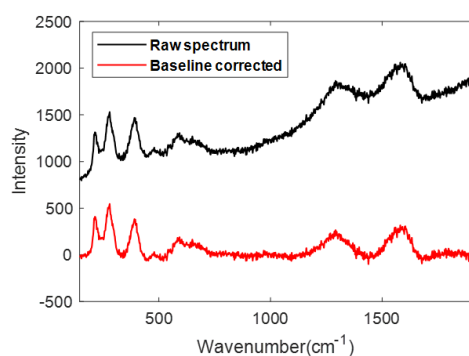


Figure 4.2. Baseline correction by adapting the spectrum to an asymmetric truncated quadratic cost function of order 7 and a threshold of 0.1.

Savitzky-Golay smoothing. One of the most applied filters for smoothing, it eliminates spectral noise by interpolation of a polynomial in small windows. Parameters such as the size of the window and the order of the

polynomial must be imposed. An example of spectral smoothing is shown in Figure 4.3.

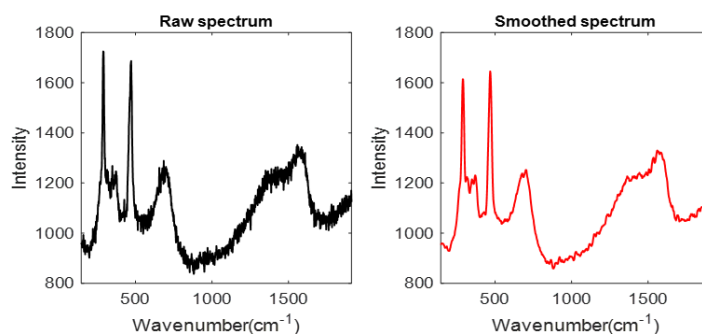


Figure 4.3. Savitzky-Golay smoothing with a polynomial order of 2 and a window of 15.

Derivates. Also based on Savitzky-Golay, it minimizes spectral noise. The first derivate is useful to correct additive scattering effects, whereas the second derivate can deal with multiplicative scattering. However, the spectral shape is modified by these operations, although baseline correction is not necessary. Some of the necessary parameters are the window size and the polynomial and derivative degrees. An example of the first and second derivatives is shown in Figure 4.4, where it is worth noticing how these operations affect scattering effects.

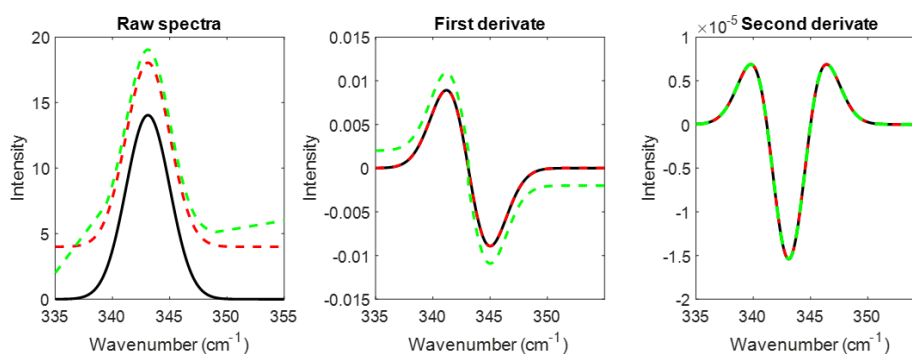


Figure 4.4. Derivative pre-processing on normal spectra (black) and spectra showing additive (red) and multiplicative (green) scattering effect.

4.2.2 Principal Component Analysis (PCA)

This is one of the most widely used unsupervised chemometric techniques for exploring multivariate data [101]. PCA is applied to reduce dimensionality, i.e., the number of variables of the original dataset, removing redundant and correlated variables but preserving the maximum of information. It reveals patterns and inner relationships. PCA should not

be confused with a classification technique (supervised methods), as no limits, thresholds or any other type of supervision is needed. PCA scheme is as follows:

1. Data is arranged in a matrix X with dimensions $I \times J$ where each row corresponds to a sample and each column to a variable.
2. Each sample is projected into an N -dimensional space, also known as *variable space*, equal to the number of variables, i.e., each axis corresponds to a variable and each sample is a point in the space. Normalization is usually applied so that the barycenter of the samples is shifted to the center of the variable space.
3. The next step is to find a direction that explains the maximum variability of the data but imposing a constraint: that direction has to pass through the center of the variable space. This direction will be the first *principal component* (PC1). We repeat this operation to find the second principal component (PC2) that explains the second greatest possible variability (not explained by PC1) but imposing a new constraint: this direction must be orthogonal to PC1. We repeat the operation until the remaining variance is very low, which is usually associated with experimental noise. Finally, all the PCs are projected into a new hyperspace called *principal components space*, which are linear combinations of the original variables.
4. Once samples are projected into the new principal components space, the distances of each sample with respect to the center of the new axes (PCs) are calculated and included in a new matrix called *Scores*. This matrix has dimensions $I \times n$, where n is the number of PCs calculated. A second matrix called *Loadings* is also calculated, with dimensions $n \times J$. This matrix contains information on the relationship between the old variable axes and the new PC axes. The variability not explained by the PCs is included in another matrix called *Residuals* with dimensions $I \times J$.

Summarizing, PCA decomposes an initial matrix X into scores and loadings matrices (Figure 4.5).

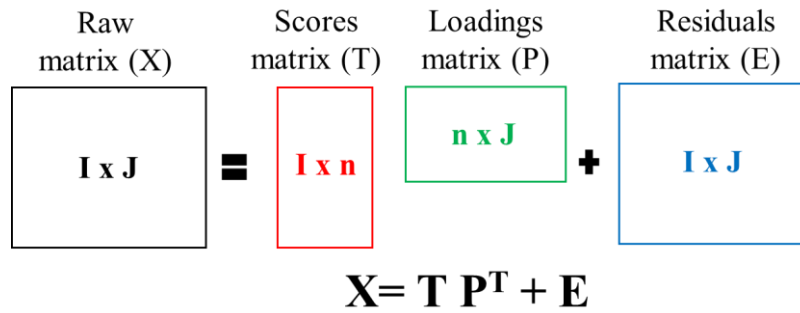


Figure 4.5. Principal Component Analysis decomposition.

4.2.3 K-means clustering

This is another unsupervised method that searches for different groups (known as *clusters*) in the data using distances between samples in an iterative approach. The objective is to find underlying patterns between the different groups of samples [102,103]. In general, K-means algorithms work as follows:

1. Selection of the K clusters we expect in our data. The number of clusters is chosen based on previous information or in a trial-and-error procedure.
2. Random selection of a number of samples equal to K. These samples are considered the initial centroids.
3. Then, starting from a different sample, the Euclidean distance with respect to the initial centroids is measured. That point is assigned as belonging to the cluster of the nearest centroid. This operation is repeated with the rest of the points until all the samples have been assigned to one of the K clusters.
4. The next step is the calculation of the mean or center of each cluster.
5. Now, step 3 is repeated but this time measuring the distances of each sample with respect to the center of the previous clusters.
6. If clusters do not change after this new iteration, then the calculation is done, otherwise the process is repeated with new iterations until no changes are made in the clusters.

One of the drawbacks of this algorithm is that is very dependent on the initial random selection of the centroids. This means that repeating the process twice by imposing the same number of clusters at the beginning could

provide slightly different results. To overcome this situation, it is advisable to carefully analyze the results. Moreover, if we repeat the process but increase the number of clusters each time, the total variability within each cluster will be lower. If the number of clusters is equal to the number of samples, then the total variability is zero, which means that we have over-fitted the algorithm to the data and therefore the information provided is meaningless.

4.2.4 Pearson correlation

Pearson correlation analyzes the relationship between two variables, for instance, between variables of two different spectra. It is based on the correlation coefficient r . This coefficient measures the direction and strength of the linear correlation between pairs of continuous variables [104,105]. In the case of spectral data, each spectrum must have the same number of variables and there must be no missing values. The correlation coefficient takes into account the covariance between the two spectra and the variance of each spectrum, and is computed as follows:

$$r = \frac{\sum(x_i - \bar{x})(y_i - \bar{y})}{\sqrt{\sum(x_i - \bar{x})^2 \sum(y_i - \bar{y})^2}}$$

where x_i and y_i are each of the i variables in the first and second spectrum, respectively and \bar{x} and \bar{y} are the mean values of those two spectra.

The correlation coefficient ranges from -1 to 1. The sign indicates the direction of the relationship between the two spectra and the magnitude indicates the strength of that relationship. A correlation coefficient close to zero means that there is no correlation at all, while the higher the value, the higher the correlation. Figure 4.6 shows an example of the correlation of one spectrum with the other three different spectra.

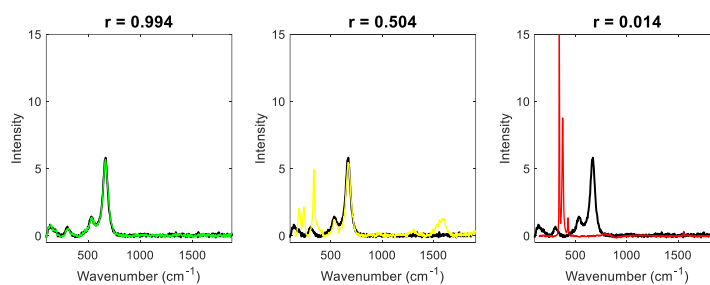


Figure 4.6. Pearson correlation. From left to right, spectra are strongly correlated, moderately correlated and not correlated.

4.2.5 Multivariate Curve Resolution – alternating least squares (MCR-ALS)

Multivariate Curve Resolution (MCR) is an unmixing method which decomposes the raw data into a reduced bilinear model of pure contributions [106]. Like in PCA, it searches maximum data variance but based on real chemical meaning. Contrary to the principal components, here there is no orthogonality. The general formula is:

$$X = CS^T + E$$

where X is the raw matrix, C is the matrix of concentration profiles, S is the matrix of pure signals and E is the residuals matrix.

For example, if MCR is applied to a hyperspectral image [107,108] with different materials, each column of the calculated concentration matrix will correspond to each of the chemical components, whereas each individual value refers to the concentration of each pixel in one of the components. Each row of the pure signal matrix corresponds to the purest spectrum of each component of the sample. Figure 4.7 illustrates this example:

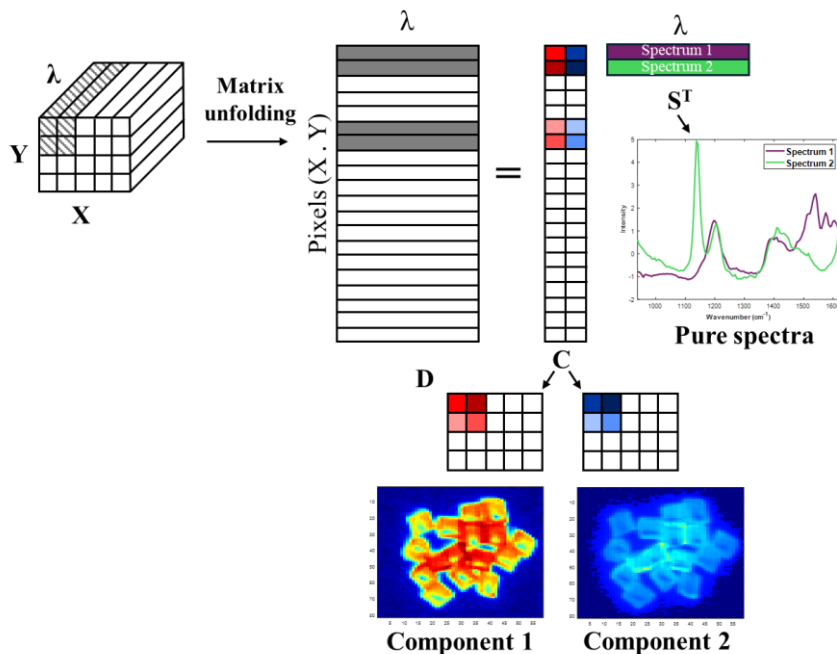


Figure 4.7. MCR-ALS applied to a hyperspectral image.

The fact that orthogonality is not imposed in MCR is important, as the calculated model allows signal overlapping, which is a more realistic interpretation of the original data, contrary to the PCA.

An MCR-ALS model is calculated as follows:

1. The first step is the selection of the number of components. If a PCA is performed, then the number of PCs explaining most of the variance can be used as an estimation of the number of components in MCR.
2. Then it is necessary to build the initial concentration or pure spectra estimates. There are several methods for this operation such as Purest variable selection or Evolving Factor Analysis.
3. The initial estimations of C or S are optimized iteratively by Alternating Least Squares algorithm (ALS). Several constraints are applied at each iteration. These include non-negativity, closure, unimodality or normalization, among others. At each iteration, a new estimate of the C and S matrices is obtained by minimizing the difference between $S^T=C^+D^*$ and $C=D^*(S^T)^+$, where D^* is the PCA reproduced data matrix for the number of components previously selected and C^+ and $(S^T)^+$ are the pseudoinverse matrices of C and S^T , respectively.
4. Optimization is repeated until convergence is achieved.

One of the limitations of MCR-ALS is that the solutions are not unique. This limitation is due to the so-called rotational ambiguity [109], which can be estimated as :

$$D = CT^{-1}TS^T$$

Where T is a non-singular matrix with both dimensions equal to the number of components. This equation means that different rotations of the C and S matrices by means of T produce the same solution. We have ambiguity in our models when several sets of C and S matrices reproduce the data with the same optimal fit.

Part III

*Studies conducted in
relation to the main topics*

Chapter: Raman library | 5

”

The intelligence consists not only in the knowledge but also in the skill to apply the knowledge into practice.

— Aristoteles

In the thesis, we focus on Raman spectroscopy as the main analytical tool for the evaluation of pyrite and its weathering products, since each mineral presents a series of vibrational modes that allow its identification. Therefore, the identification of unknown samples by Raman spectroscopy requires the comparison of the acquired spectra with Raman libraries. Commercial Raman libraries of many different materials are available (e.g. plastics, pigments, biological samples, minerals, etc...), as well as online libraries compiled by different users. An example of a commercial library specific to minerals is the one provided for the Wire software (Renishaw, UK). In the case of free online libraries, a famous example is the RRUFF project, where thousands of mineral spectra are available to download. However, both commercial and non-commercial libraries are very dependent on the skills of the person who acquired the spectra, the imposed acquisition parameters, the laser, the data pre-processing operation performed, the morphology and orientation of the sample, heterogeneities on the surface or presence of trace elements, among many other factors.

To overcome these limitations, the first activity carried out in the present thesis was the acquisition of a Raman library of pyrite and related minerals from different geological locations, morphologies and in different weathering stages. This personal library has been used in subsequent studies carried out in the thesis.

As part of this activity, a software was created in MATLAB environment for the management of a personal Raman library, making it possible to write detailed information about the samples, upload photos of the samples, pre-process the spectra, make comparisons between spectra as well as search for matches between a new spectrum and the ones included in the library.

5.1 Samples

The mineralogical collection analyzed includes samples of pyrite (FeS_2), goethite ($\alpha\text{-Fe}^{3+}\text{O}(\text{OH})$), hematite (Fe_2O_3), magnetite ($\text{Fe}^{2+}\text{Fe}^{3+}_2\text{O}_4$), chalcopyrite (CuFeS_2), arsenopyrite (FeAsS), pyrrhotite (Fe_{1-x}S), galena (PbS), marcasite (FeS_2), ilmenite ($\text{Fe}^{2+}\text{TiO}_3$), limonite (mixture of other iron oxide and oxy-hydroxides) and elemental sulfur from different geological settings and locations. The total number of samples was 30. Some samples are pristine or show no apparent signs of weathering, while others are in varying degrees of weathering. Small fragments were taken from each of the samples, so measurements were made of the surface and inside of the samples. Different zones of each of the fragments were analyzed in order to capture the spectral variability within the same sample in the library. In addition, using the Raman microscope, images were taken before and after the acquisition of the spectra. All spectra were acquired from unpolished samples.

5.2 Instrumentation and acquisition parameters

The Raman spectrometer used to acquire all the spectra was an *inVia QontorTM* confocal Raman spectrometer (*Renishaw, England, UK*), equipped with *LiveTrack focus-tracking*. This technology automatically maintains focus during the analysis of rough, uneven, or curved samples. The spectrometer was also equipped with an edge filter and 1800 mm⁻¹ (vis) grating for the excitation beam laser. The laser used for the acquisition of the library was the 532 nm laser (green; theoretical laser-spot diameter $\sim 0.84 \mu\text{m}$). The laser was adjusted between 5 and 10 % of its power. (depending on the sample) by using a neutral filter. Calibration was carried out daily using the 520.5 cm^{-1} line of a silicon standard.

Each spectrum was acquired using the following parameters: exposure time 1s, three accumulations per spectrum and 65 μm slit opening. Preliminary tests were carried out to identify the combination of parameters to obtain the best possible spectral quality and replicability in the measurements. In addition, the choice of these relatively mild parameters avoids chemical transformation during exposure to laser radiation. Spectra were acquired in the range between 144.5 and 1906.5 cm^{-1} , with an average spectral

resolution of 1.75 cm^{-1} . Each spectrum finally included in the library is the average of three spectra measured under identical conditions.

5.3 Spectra acquired

In total, 303 spectra were included in the library. Specifically, 131 of these spectra were pyrite samples from 11 different locations. In general, pristine or freshly fractured pyrite fragments do not show vibrational modes other than the three typical E_g , A_g and T_g modes. However, some of the fragments with evident weathering symptoms on the surface contain additional signals, as illustrated in Figure 5.1, where pyrite spectra from 4 different locations are shown.

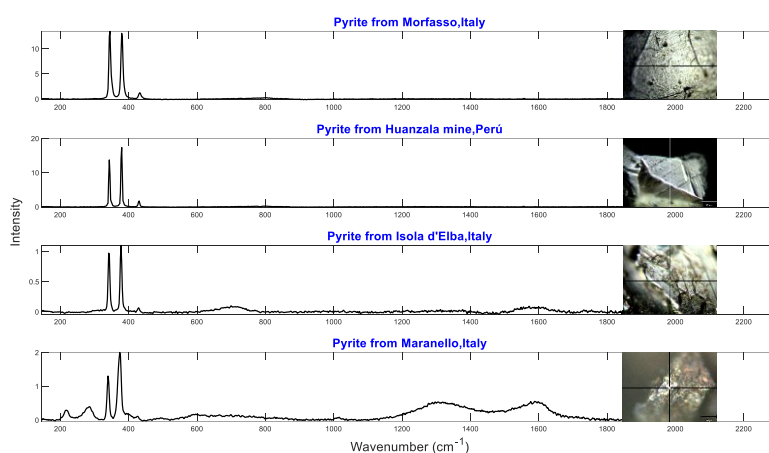


Figure 5.1. Pyrite spectra of four different locations. Spectra has been pre-processed (baseline correction, smoothing and scaling).

As can be observed, samples from Morfasso (Italy) and Huanzala mine (Perú) show the 3 typical Raman peaks of pyrite. All the samples collected at these two locations, as well as each of the small fragments from which spectra were acquired, showed no apparent alterations due to weathering after a first evaluation under the reflected light microscope. On the contrary, pyrite samples from Isola d'Elba (Italy) and Maranello (Italy) showed different degrees of weathering, which could be appreciated by the loss of the typical pyrite luster and the appearance of a reddish patina in the case of the Maranello samples. The latter shows additional Raman peaks at 215.9 and 285.5 cm^{-1} , in addition to the appearance of bands in the $1200\text{-}1400$ and $1500\text{-}1700\text{ cm}^{-1}$ regions. This is probably due to the presence of weathering

compounds on the surface. The following chapter, which describes another study carried out in the thesis, will discuss this phenomenon in more detail.

Among the 131 pyrite spectra in the library, there are discrepancies about the peak position of the vibrational modes. Table 5.1 shows the peak positions found for each of the 3 vibrational modes of pyrite, along with the percentage of spectra showing that peak at that position.

Table 5.1. Peak position and occurrence of the E_g , A_g and T_g vibrational modes of the 131 spectra analyzed.

1 st vibrational mode (E_g)		2 nd vibrational mode (A_g)		3 rd vibrational mode (T_g)	
Wavenumber (cm^{-1})	Occurrence (%)	Wavenumber (cm^{-1})	Occurrence (%)	Wavenumber (cm^{-1})	Occurrence (%)
343	55	379	45	430	43
341	29	377	33	429	42
345	10	375	15	427	9
339	6	374	7	432	6

Peak positions have been rounded to the nearest integer, so small deviations are not contemplated. The most common pyrite peaks are 343 cm^{-1} (E_g), 379 cm^{-1} (A_g) and 430 cm^{-1} (T_g). A combination of different peak positions has been found between those listed in the table.

In the literature (Table 5.2), there are also discrepancies between the vibrational modes of pyrite, although the most repeated peak positions correspond to what was seen in the personal Raman library.

Table 5.2. Vibrational modes of pyrite in different studies carried out in the literature.

Study	E_g (cm^{-1})	A_g (cm^{-1})	T_g (cm^{-1})
[110]	343	379	430
[111]	343	379	430
[112]	343	379	430
[113]	343	379	430
[53]	343	379	430
[114]	344	379	430
[115]	344	381	431
[116]	342	379	432
[117]	335	371	421
[118]	340	370	424
[119]	342	377	428
[120]	342	380	430
[121]	338	374	424

Obvious discrepancies are due to the nature of the samples [117] and [121] which are nanochains and pyrite microcrystals, respectively.

On the other hand, two pyrite samples were used to test how the relative intensity of the E_g and A_g peaks changes as the fragment is rotated. For this purpose, a recognizable point on each surface was identified and a first spectrum was acquired. Then, without moving the sample position and thus the laser incidence point, the samples were carefully rotated 45° and again a new spectrum was acquired. Finally, this operation was repeated by rotating another 45° . The results are shown in Figure 5.2.

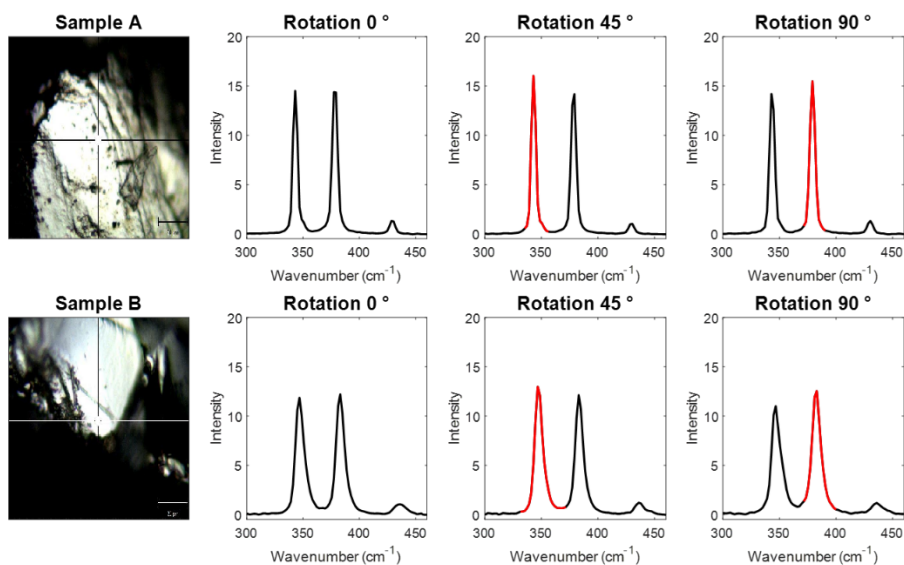


Figure 5.2. Effect on the relative intensity of E_g/A_g peaks with rotation. A peak highlighted in red means higher intensity with respect to the other.

As can be seen, the orientation of the sample with respect to the laser plays a role in the relative intensity of the E_g and A_g modes. The fact that the relative intensity was almost the same at the beginning (0°) in the two samples was just a coincidence, i.e., the orientation of the crystals was the same. However, it should be noted that if the orientation changes, the relative intensity changes. This could explain why in many of the pyrite spectra, sometimes the intensity of the E_g mode is greater than that of the A_g mode and vice versa.

For the rest of the minerals included in the library, both unaltered fragments and fragments showing signs of alteration were analyzed. The number of spectra included in the library will be of great help for the subsequent studies

carried out in the thesis, since they helped in the identification of some vibrational modes. Some of these spectra are shown in Figure 5.3.

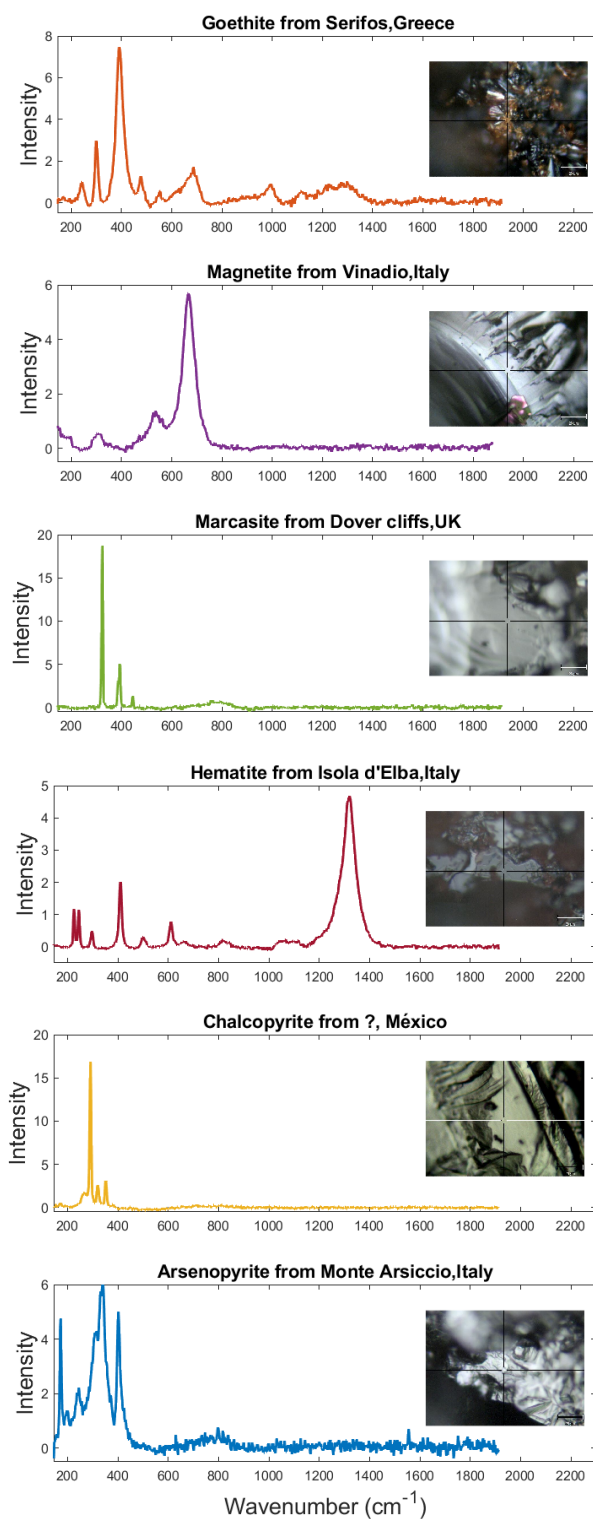


Figure 5.3. Some of the Raman spectra of goethite, hematite, magnetite, chalcopyrite, marcasite and arsenopyrite are included in the library. Spectra were normalized for easier comparison.

5.4 Software development

A software was created in MATLAB using the app design tool, which allows the construction of the graphical user interface and coding. Due to the number of spectra acquired during this study, the idea was to have a quick and easy way to organize and access spectral information without the need for commercial software and licensing requirements. When loading the spectra into the software to create a database, it is possible to include all kinds of written information about the samples, as well as to accompany each of the spectra obtained with a photo of the sample or of the magnified area where the measurement was taken, if available. Once all the information has been loaded into the software, it is possible to perform operations such as quick comparison between any two spectra and preprocessing of the data. In addition, if a new spectrum is entered, it is possible to perform a similarity search based on the Pearson correlation coefficient with respect to the spectra included in the library. The information of the database can be stored and loaded in a few seconds, making it possible to modify the information or delete samples. A stand-alone version of the program was created, so that everyone can download, install and run it on their computer without the need for MATLAB or computer skills.

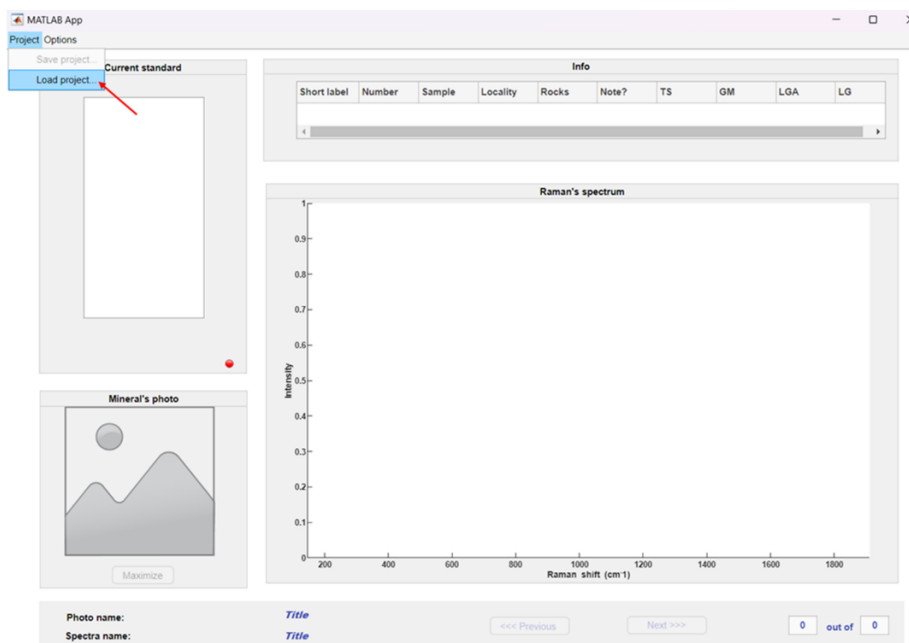


Figure 5.4. Main window of the software.

The main window of the software is shown in Figure 5.4. When opened, the top bar shows two buttons, where you can load a project if it has already been created previously, or you can start creating one from scratch. To create a new project, a new window will appear after clicking on the appropriate button. In this window, it is possible to fill in a template with all kinds of information about the samples, as shown in Figure 5.5.

The screenshot shows a MATLAB App window titled 'Project Options' with a sub-window 'Add new standard'. On the left, a list of mineral abbreviations is provided: Arsenopyrite ==> Apy, Chalcopyrite ==> Ccp, Epsomite ==> Eps, Galena ==> Gn, Goethite ==> Gth, Hematite ==> Hem, Ilmenite ==> Ilm, Lepidocrocite ==> Lep, Limonite ==> Lim, Magnetite ==> Mag, Marcasite ==> Mrc, Pyrite ==> Py, and Pyrrhotite ==> Po. The main form contains the following fields: 'Short label' with 'Py', 'Location' with 'La rioja, Spain', 'Rocks' with 'Cretaceous marl', 'Number of the standard' with '4', and 'Sample ID (collection)' with '0'. A 'Notes' field contains 'Cubic pyrite, shiny, 4 cm'. Below these are checkboxes for 'Type of preparation' with options: 'Thin section' (unchecked), 'Grain mount' (checked), 'Araldite' (unchecked), and 'Loose grains' (unchecked). At the bottom are buttons for 'LOAD SPECTRUMS' and 'LOAD MINERAL PHOTOS', both with red dots, and a 'FINISH' button. A 'Close' button is in the bottom right corner.

Figure 5.5. Template to write information on each of the samples included in the project.

The allowed format for uploading spectra is .txt. For images, it is .jpg. By clicking on load spectra or images, it is possible to locate the files using the interface of the operating system where the software is being used, as shown in Figure 5.6.

Once the project has been created, it is possible to quickly browse through each sample and visualize its different spectra, as shown in Figure 5.7. It is also possible to zoom in and identify the position of the peaks. If images have been loaded for a sample, they will appear in the lower-left corner of the main window. However, if a better view of the image is needed, a larger image will appear in the center of the main window when the maximize button is pressed.

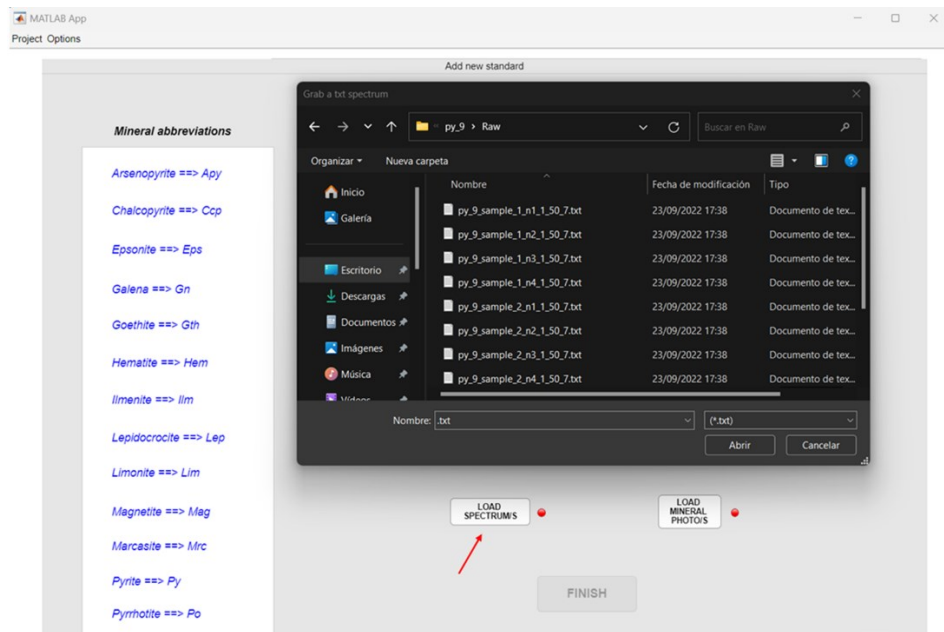


Figure 5.6. Window to load the spectral file(s) of the sample being included in the project. A similar window will appear for loading images.

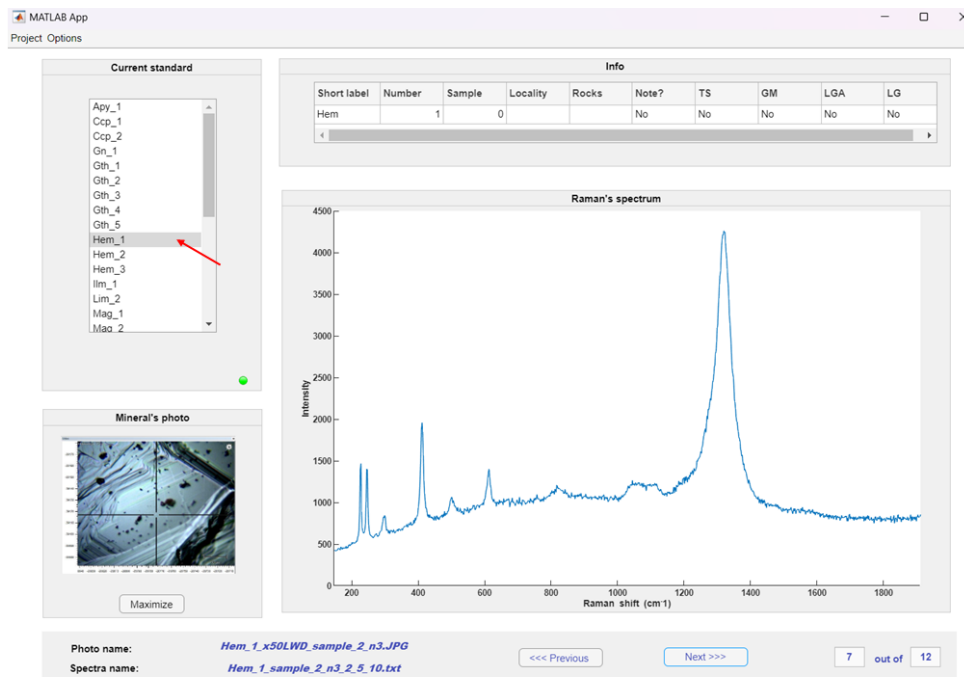


Figure 5.7. Example of how the main window looks once a project has been loaded/created. It is possible to browse through different samples and spectra.

Pressing the options button displays various functions such as comparing different spectra (Figure 5.8), preprocessing the spectra (Figure 5.9) or

displaying the sample information in table format (Figure 5.10), among others.

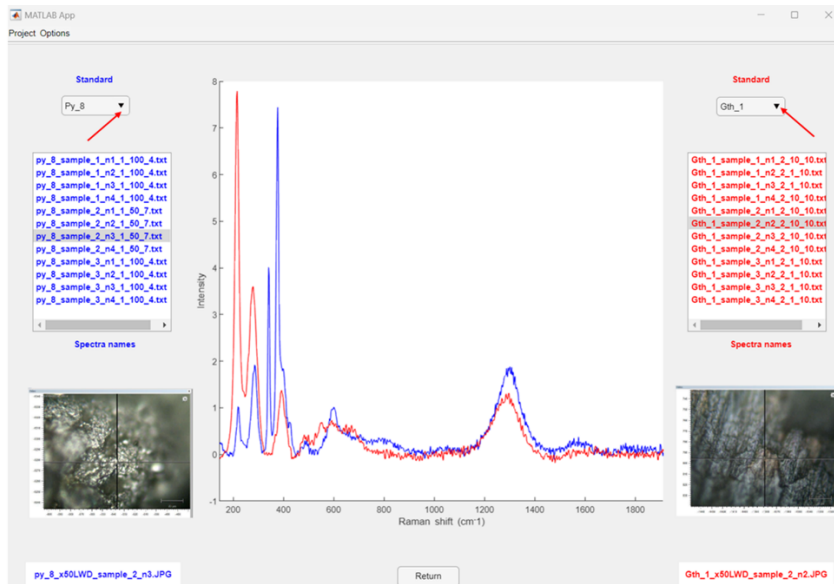


Figure 5.8. Window for comparing spectra. First, samples are selected by clicking on the drop-down list of samples. Then, spectra by clicking directly on the fixed list.

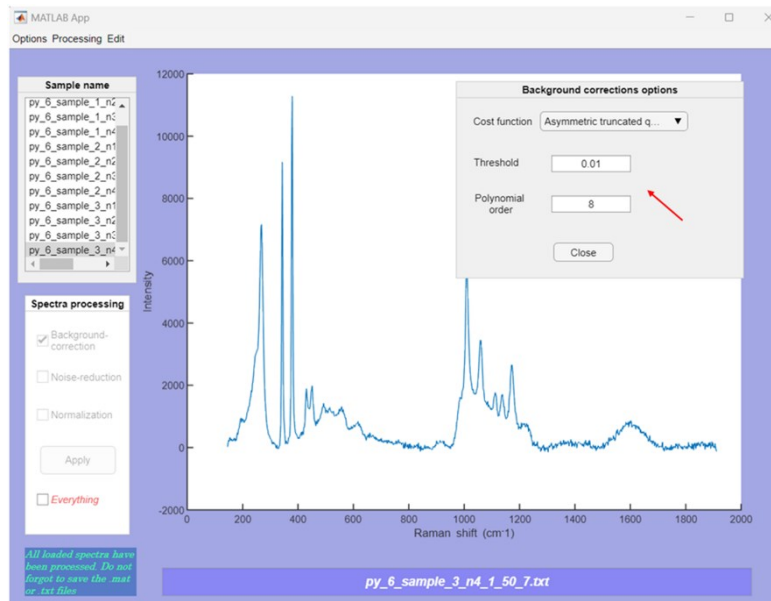


Figure 5.9. In this window, there are different options for baseline correction, and it allows the modification of the parameters. It is also possible to perform smoothing and scaling.



Short label	Number	Sample	Locality	Rocks	Note?	TS	GM	LGA	LG
Gth	1	1710	Pierda Niedda		No	No	No	No	Yes
Gth	2	498	Rio Marina		No	No	No	No	Yes
Gth	3	2928	Seritos		No	No	No	No	Yes
Gth	4	1129	Schipario		No	No	No	No	Yes
Gth	5	125	Libiola		No	No	No	No	Yes
Py	1	0	Val Trebbia		No	No	No	No	Yes
Py	2	2681	Brosso		Yes	No	No	No	Yes
Py	3	0	Morfasso		Yes	No	No	No	Yes
Py	4	0	Perù		No	No	No	No	Yes
Py	5	1673	Brosso		No	No	No	No	Yes
Py	6	0	Camerata Com...		No	No	No	No	Yes
Py	7	66	Isola d'Elba		Yes	No	No	No	Yes
Py	8	1213	Maranello	Sea rock-Marl	Yes	No	No	No	Yes
Py	9	1230	Valle d'andagna		Yes	No	No	No	Yes
Py	10	0	Isola d'elba		No	No	No	No	Yes
Py	11	2466	Fiume- Valle d...		No	No	No	No	Yes
Hem	1	1209	Isola d'elba - Ri...		Yes	No	No	No	Yes
Hem	2	0	Seritos		Yes	No	No	No	Yes
Hem	3	0	Isola d'Elba -P...		Yes	No	No	No	Yes
Mag	1	711	Vinadio		No	No	No	No	Yes
Mag	2	2079	Traversella		No	No	No	No	Yes
Ccp	1	0	Mexico		No	No	No	No	Yes
Ccp	2	677	Lago d'Isco		No	No	No	No	Yes
Gn	1	0	Traversella		No	No	No	No	Yes
Lim	2	109	Libiola		Yes	No	No	No	Yes
lim	1	1991	Pottolo		No	No	No	No	Yes
Mrc	1	0	Dover cliffs		No	No	No	No	Yes
Po	1	0			No	No	No	No	Yes
Apy	1	0	Monte Arsiccio ...		Yes	No	No	No	Yes

Figure 5.10. The information on the samples introduced when the project was created, will appear summarized in table format.

5.5 Conclusions

This first activity carried out during the PhD period was useful in the rest of the studies carried out. The availability of a Raman library is essential because by controlling how the spectra were acquired, it is possible to ensure replicability and reliability in the Raman analyses carried out afterwards by using the same parameters and measurement conditions. In addition, having the spectra of not only different pyrites but other related minerals allow the further identification of weathering products.

As part of this preliminary activity, the software developed for the management of the Raman library served to learn the necessary computational skills in MATLAB that would prove indispensable in later studies. Additional features, such as more spectrum pre-processing options will be included in the future. In addition, the software is expected to be used for didactic purposes as a simple tool for the management and visualization of Raman spectra of minerals.

Chapter: Weathering products characterization by hyperspectral imaging | 6

” *Indeed, we often mark our progress in science by improvements in imaging.*

— Martin Chalfie,
2008 Nobel Prize in Chemistry

A study on oxidative weathering of pyrite should include a methodology for surface characterization. Adequate knowledge of the distribution of alteration products is crucial analytical information, as it allows a better understanding of the oxidation process that the mineral has undergone. Raman spectroscopy has proved to be an important technique for the identification of minerals. However, the traditional single-point analysis does not allow a proper surface characterization of the spatial distribution of weathering products. In contrast, the hyperspectral Raman imaging approach overcomes these limitations by relating spatial coordinates to chemical features, resulting in images based on spectral information. Proper data-driven analysis of these images can provide useful information on the spatial distribution of weathering products on mineral surfaces.

In this study, a novel methodology has been developed for the characterization of pyrite weathering products by combining Raman hyperspectral imaging with chemometrics. A proper data pre-processing and analysis protocol allows for the evaluation of these alteration products, providing information that can be used for the study of pyrite found in different geochemical systems. To test the validity of this methodology, a sample of natural pyrite showing signs of chemical alteration on its surface was analyzed. Exploratory analysis based on Principal Component Analysis, K-means clustering, and Multivariate Curve Resolution-Alternating Least Squares allowed semi-quantitative threshold-based characterization of the distribution of chemical phases on the surface.

6.1 Sample

The sample used to test the developed methodology of this study (Figure 6.1) is a pyrite fragment collected in Velleia Romana (Piacenza province, northern Italy). This locality, which has been described in the literature [122,123], is a natural source of other minerals such as marcasite and baryte. In this area, minerals are found in red clays and marls belonging to the Cretaceous Liguride units (Argille Scagliose).

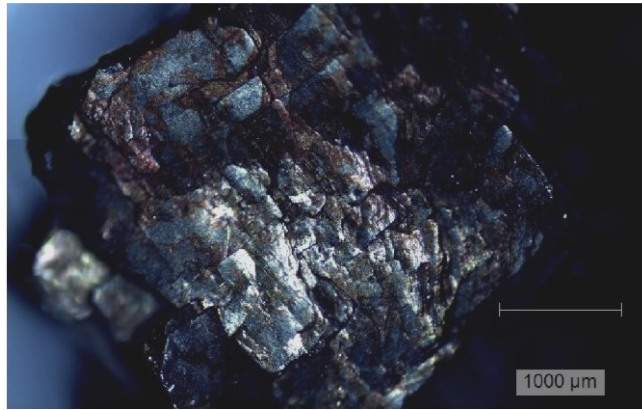


Figure 6.1. Pyrite sample analyzed in this study. Brownish areas at the corners and edges are presumably alteration products, whereas the bright zones are unaltered pyrite.

6.2 Instrumentation and hyperspectral image

The Raman spectrometer and instrumental setup used in this study have been already described in Chapter 5 of the present dissertation. The acquisition conditions were as follows: 5% power of the laser, slit opening 65 μm, exposure time 1 s and number of accumulations equal to 3. These conditions were chosen to avoid local heating of the surface due to laser exposure, which can induce chemical transformations. The spectral range was 144.5-1906.5 cm^{-1} . The average spectral resolution was 1.74 cm^{-1} , with a total number of points per spectrum equal to 1015. The spatial resolution of the grid of analysis for the hyperspectral image acquired was 15 μm in both X- and Y-directions. All the spectra were organized into a three-dimensional data array with dimensions 126 x 143 x 1015, being the first two the spatial dimensions (X and Y coordinates of each pixel) and the third the spectral dimension λ . The number of pixels of the resulting image was 18018.

6.3 Software

MATLAB R2022b (*MathWorks, Massachusetts, USA*) was used for dataset preparation and data pre-processing. HYPER-Tools 3.0 toolbox [124] was used for exploratory analysis, whereas MCR-ALS 2.0 toolbox [125] was used for spectral unmixing operations. In-house codes were created in MATLAB environment for cosmic spikes removal and construction of the final images.

6.4 Results and discussion

6.4.1 Spectral pre-processing

Before starting any exploratory analysis, it is essential to extract the information of interest that could be masked due to the presence of different artifacts. Since the analyzed surface has different mineralogical phases and is not completely flat, Raman scattering effect is different for each pixel. This also applies to background fluorescence and spectral noise. In this study, several pre-processing steps were applied.

The first step was the elimination of dead pixels, which are pixels of null intensity in the spectral channel. Dead pixels are due to incomplete acquisition of spectra when abrupt changes in the height of the sample surface make proper autofocusing difficult. In total, 15 out of 18018 pixels were identified as dead pixels. Although the percentage is really low, it is important to get rid of these pixels to avoid undesired influences during the rest of pre-processing and data analysis operations. Hence, a spatial mask was created to keep out those pixels. A spatial mask is a two-dimensional binary matrix with dimensions equal to those of the hyperspectral image. Spatial masks are often used for different purposes, for instance, if there is only interest in analyzing certain areas of the image.

Then, saturated pixels were detected by means of PCA. Saturation of the CCD detector during acquisition causes artifacts as those shown in Figure 6.2. In particular, Hotelling's T^2 and Q residuals [126] calculated during the PCA were used as outlier diagnostic, having identified a total of 264 saturated pixels. Instead of excluding these pixels with the spatial mask previously created, they were replaced by the average spectrum of the

neighboring pixels, as saturated pixels were distributed throughout the surface without a clear pattern distribution.

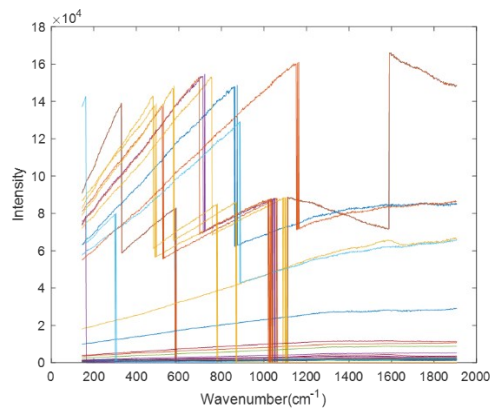


Figure 6.2. Spectra of some of the saturated pixels detected.

The next step was the elimination of cosmic spikes, which are caused by the unexpected incidence of high-energy cosmic radiation in the CCD detector. This uncontrollable phenomenon generates spurious Raman information at random positions in the acquired spectra which can be superimposed on chemically meaningful vibrational modes. For this purpose, a MATLAB routine was created for the automatic correction of cosmic spikes. The procedure was based on an iterative approach using the second order derivative and the half-height peak width to highlight the cosmic peaks among the real Raman modes. Once detected, cosmic spikes are removed by interpolation of the signal. In total, 46 cosmic peaks were detected and removed from the affected spectra.

In addition, baseline correction was performed by adapting each spectrum to an asymmetric truncated cost-function [127]. To avoid loss of spectral information or the creation of additional Raman peaks, several parameters were tested, finally choosing a threshold of 0.001 and a polynomial order of 9 as the best compromise. Moreover, Savitzky-Golay smoothing (7-point windows and a polynomial degree of 2) was applied to the data, followed by SNV for additive scattering correction. Finally, the spectral range was cropped to 200-1650 cm^{-1} .

The effect of pre-processing operations from the raw image (a) to the fully pre-processed image (d) can be observed in Figure 6.3.

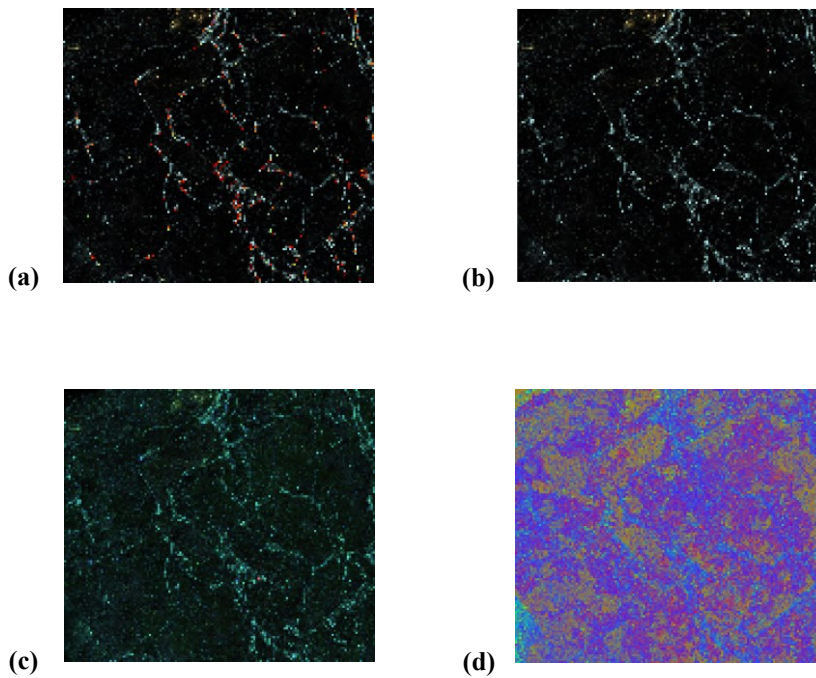


Figure 6.3. Fake RGB images. (a) Raw data, (b) after saturation and cosmic spikes removal, (c) after baseline correction and (d) after smoothing and SNV.

6.4.2 Principal Component Analysis

The next step was the exploratory analysis of the hyperspectral image by means of Principal Component Analysis (PCA). The application of this technique follows the fundamentals of PCA already explained in chapter 4. However, when applied to hyperspectral images, an additional step must be performed before calculating the PCA model: the unfolding of the three-dimensional array into a two-dimensional matrix with a number of rows equal to the number of pixels and with a number of columns equal to the number of spectral channels, as shown in Figure 6.4.

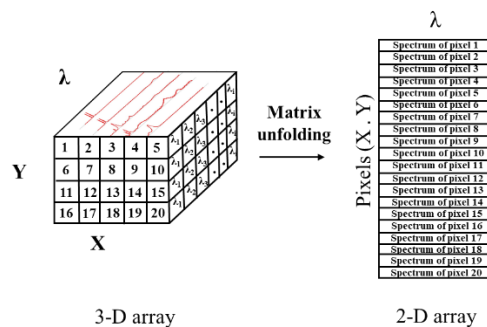


Figure 6.4. Unfolding of a hyperspectral image into a two-dimensional matrix.

Once the PCA model has been computed, the scores matrix is refolded into n 3-D matrices (one for each of the n calculated principal components), where each pixel has the same coordinates as the original hyperspectral image. The pixels in these images are colored according to the score value for that principal component.

The three calculated principal components (PCs) explain $\sim 63\%$ of the total variance, as shown in Figure 6.5.

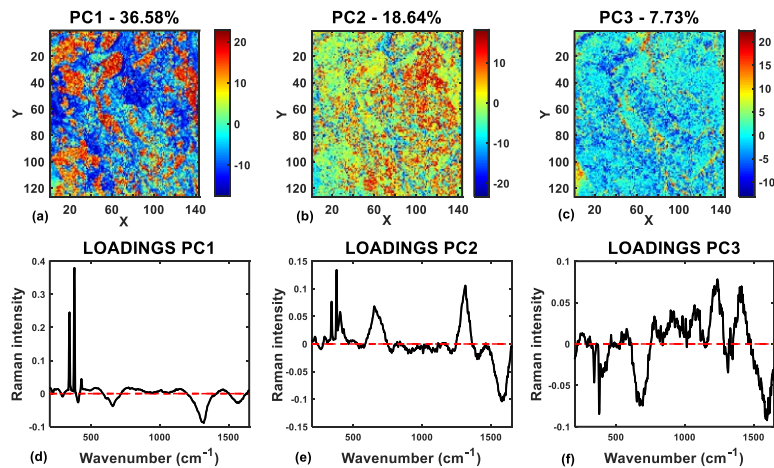


Figure 6.5. Scores (a, b, c) and loadings (d, e, f) for the first three principal components, respectively.

The positive loadings of PC1 (Figure 6.5 d) highlight variables associated with the three vibrational modes of pyrite at 343, 379 and 430 cm^{-1} , whereas the negative loadings are associated with the signals at 658, 1319 and 1575 cm^{-1} . In the score map of PC1 (Figure 6.5 a), it is possible to distinguish between areas of the sample surface characterized by very positive (orange-red) presumably associated with unaltered pyrite, and very negative (blue) which could be associated with the presence of alteration products.

The score map of PC2 (Figure 6.5 b) differentiates between pixels with positive scores, which correspond to the vibrational modes of pyrite but with other overlapped peaks at 405, 222, 289, 653 and 1313 cm^{-1} (Figure 6.5 e).

Finally, PC3 mainly highlights differences between a few pixels and the rest of the surface (Figure 6.5 c). However, pixels with positive values higher than 15 do not show a defined spectral signature, with many peaks in the 745-1480 cm^{-1} region (Figure 6.5 f). This situation is typical of low-crystalline mineralogical phases.

Subsequent PCs (Figure 6.6) show no clear pattern distribution of the pixels. Although the explained variance explained in these PCs is relatively low, loadings contain Raman information different than experimental noise or other artifacts.

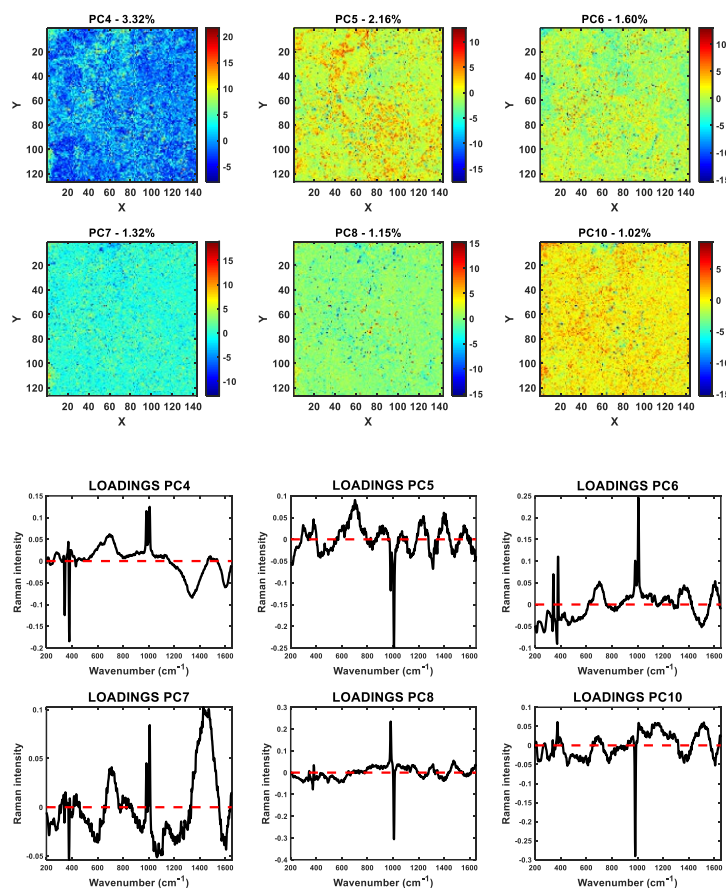


Figure 6.6. Scores and loadings for PC4 to PC10 (except PC9). The data variance explained by these PCs is $\sim 10.6\%$.

However, it is interesting to comment on PC9 (Figure 6.7). This PC defines variance associated with a few pixels of the image, as can be seen in the loadings. This PC explains a Raman shift in the typical vibrational modes of pyrite, which can be justified by the presence of trace metallic elements or defects in the crystalline structure. Therefore, this PC contains interesting information on the sample otherwise overlooked by single-point Raman analysis. To check the extent of the Raman shift, two pixels were selected, with positive and negative scores, respectively, and the spectra were plotted. (Figure 6.8).

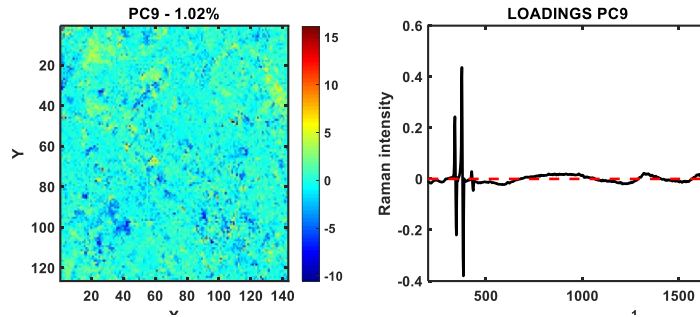


Figure 6.7. Scores and loadings of PC9. The shape of the loadings is typical of Raman shifting.

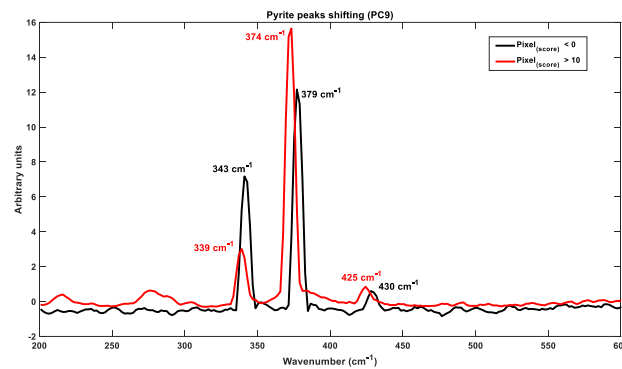


Figure 6.8. Selected pixel (positive loadings) vs. the normal pyrite peaks in the rest of the image (negative loadings).

Although the percentage of variance associated with Raman features in the first three principal components is high compared to the rest of the principal components, this information should not be dismissed, even when it is related to only a few pixels. Therefore, we concluded that the analysis of heterogeneous surfaces requires distinguishing between major and minor Raman features. In this way, the main features can be correctly analyzed without being altered by the minor features of the image, and vice versa. For this purpose, thresholds were established on the scores of the PCs and the pre-processed dataset was divided into two subsets (called major and minor features) by using a spatial mask. The major features dataset includes most of the pixels with information on the first three PCs, whereas the minor features dataset includes the rest of the pixels. The spatial distribution of the pixels included in the major and minor features dataset is shown in Figure 6.9.

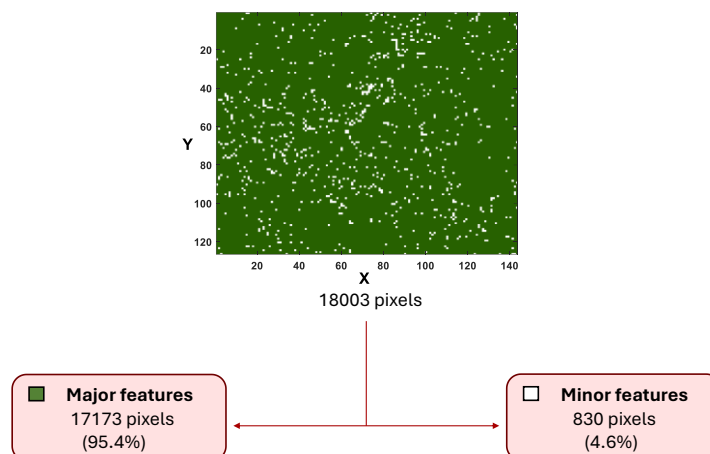


Figure 6.9. Spatial distribution of the pixels belonging to the main (green) and minor (white) features datasets.

6.4.3 Analysis of the major features

In this dataset, there are included 95.4 % of the pixels (17173 out of 18003). At this point, MCR-ALS analysis was carried out to identify spectral signatures and their spatial distribution on the surface.

Two different approaches were tested. On the one hand, the Raman spectral library acquired (Chapter 5) was used for the initial estimation during the iterative calculation of the MCR-ALS model. On the other hand, initial estimations were calculated by pure variable selection method.

Library-based MCR-ALS model. In this model, only some of the spectra included in the library were used for the initial estimations of the spectral profiles. For the selection of the most suitable spectra to be used as a reference, Pearson correlation models were calculated, and spectra were sorted according to the correlation coefficient values. The number of components selected was three, following the information provided by the previous PCA. Hence, the three spectra with the highest correlation coefficient were selected as initial estimations. Then, an offset was added to the spectral channel and a non-negativity constraint was imposed for both spectral and concentration profiles. Convergence criteria were set to 0.1 and the number of maximum iterations selected was 100. A preliminary model showed a good correspondence between reference and pure spectra calculated only for two of the components. In particular, the third component

did not match with any of the spectra in the Raman library. To overcome this situation, the pixels in the third showing poor correspondence with the reference spectra of the library were selected, and the average spectrum was calculated. Now, the MCR-ALS model was calculated again using for the initial estimations this average spectrum plus the two spectra of the library with the highest correlation coefficients.

The percentage of explained variance by this model was 98.6 %. For the estimation of rotational ambiguity, the algorithm described in [128]. The difference between f_n^{\min} and f_n^{\max} for the three components were 0.31, 0.39 and 0.37, respectively, which indicates that a certain degree of rotational ambiguity is present. Concentration and pure spectral profiles are shown in Figure 6.10. As can be seen, concentration profiles show well-defined areas on the surface (Figure 6.10 a-c). In addition, a good correspondence between reference spectra used for the initial estimations and pure spectra is obtained (Figure 6.10 d-f).

In the first component, pixels associated with scores higher than 0.6 have spectral signatures characterized by the three main vibrational modes of pyrite plus small peaks at 218 and 285 cm^{-1} and broad bands in the 1200-1400 cm^{-1} and 1578 cm^{-1} regions. There are two hypotheses to explain this situation. One option is the presence of an amorphous carbon phase of different thickness, which is characterized by vibrational modes of some carbon structures (D-band from 1320 to 1360 cm^{-1} and G-band from 1520 to 1600 cm^{-1}), as seen in [129,130]. The second option could be the presence of a patina on the surface made of different alteration products. In both cases, areas where the thickness of the patina is low are dominated by pyrite vibrational modes with high intensity compared to the rest of the peaks. In addition, one of the spectra used for the initial estimations of spectral profiles was a spectrum of pyrite from Maranello (Modena, Italy) which presented similar alteration features to the sample analyzed in this study.

The second component is characterized by peaks at 224, 245, 289, 409 and 1318 cm^{-1} , which correspond to the other spectra of the Raman library used as reference, which is a hematite sample from Rio Marina (Isola d'Elba, Italy). The peak at 1318 cm^{-1} of hematite (2LO mode) should not be confused with the D-band of amorphous carbon, as was demonstrated in [131].

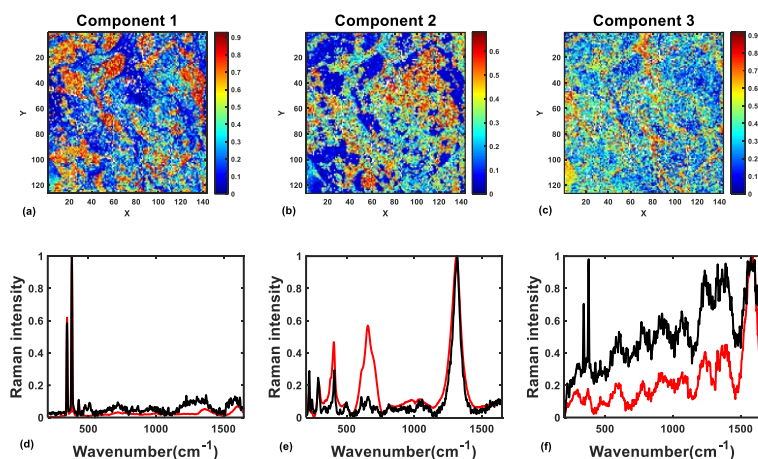


Figure 6.10. Distribution maps (a, b, c) and reference spectra (black) versus pure spectra (red) plots (d, e, f) calculated by the MCR-ALS model.

At this point, thresholds were defined on the concentration maps of the three components (0.53, 0.40 and 0.5, respectively) to perform a semi-quantitative assessment of the spatial distribution. In total, 29.5 % of the image showed concentration profiles higher than the threshold established for the first component, 26.5 % for the second component and 39.4 % for the third component. A compositional image was created for a visual interpretation of the chemical distribution of the three components on the surface, as shown in Figure 6.13 (b).

In addition, a PCA analysis was subsequently performed on the pixels related to the first component, in order to realize how many of these pixels show no other vibrational modes than pyrite. In total, 1568 pixels satisfy this, which means that only 8.7 % of the pyrite in the surface was unweathered.

Non-targeted MCR-ALS model. In this model, the initial estimation of the spectral profiles was done by the pure variable selection method, as previously explained, selecting spectra as the estimation direction and 10% noise tolerance. The rest of the constraints and parameters imposed were the same as in the previous model. The explained variance was 98.7% and the difference between f_n^{\min} and f_n^{\max} for the three components were 0.32, 0.36 and 0.37, respectively. Concentration maps and pure spectra calculated by this model are shown in Figure 6.11.

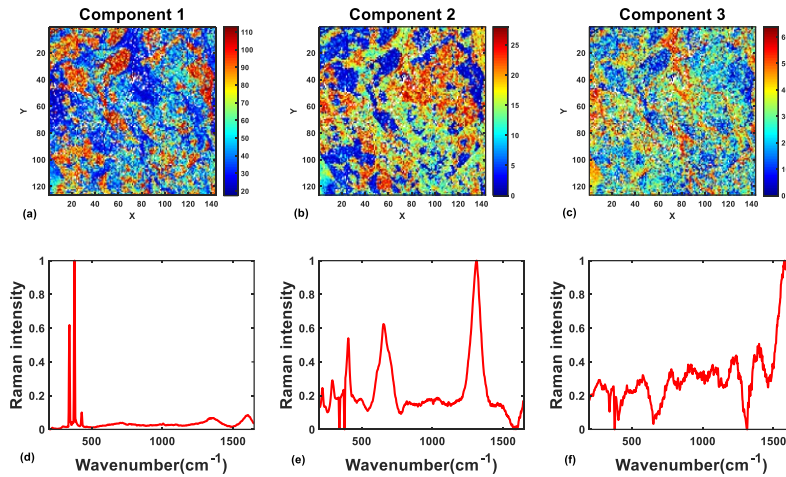


Figure 6.11. Distribution maps (a, b, c) and pure spectra (red) plots (d, e, f) calculated by the non-targeted MCR-ALS model.

The calculated pure spectra are very similar to those calculated by the previous model. If the real image (Figure 6.13 a) is compared with the concentration map of the third component (Figure 6.11 c), then this is distributed in the fractures and edges of the surface.

As previously done, a compositional image was created by imposing thresholds to the concentration profiles of the three components of this new model (79.5, 17.5 and 38.9, respectively), as shown in Figure 6.13 (c). In total, 26.4 % of the image corresponds to the first component, 32.4 % to the second component and 36.6 % to the third component. The percentages of the first and third component are not far from those of the previous model, whereas the percentage of the second component is more different. Hence, it seems that this MCR-ALS model does not resolve with the same efficiency the 2LO mode of hematite from the G-band of amorphous carbon if a proper reference spectrum is not provided for the initial estimations. Nevertheless, the main spectral features of the sample can be correctly identified even if Raman library is not used, as can be seen by comparison of Figures 6.13 (b) and (c), although this model is not able to fully distinguish the delimiters of areas characterized by hematite and the amorphous patina of component 3.

6.4.4 Analysis of the minor features

Following the results of the PCA performed in section 6.4.2, in total 830 pixels (4.6 % of the image) were included in this dataset related to minor features. Furthermore, a second PCA was performed to get rid of pixels with low signal to noise ratio within this dataset, resulting in 93 pixels excluded.

Then, a K-means clustering model was calculated for the remaining 737 pixels. This model provided information on the spectral signatures in the 982 to 1008 cm^{-1} region. The data was mean-centered and Euclidean distance was used as the metric. Four clusters were selected on the basis of a trial-and-error procedure. The calculated centroids are shown in Figure 6.12.

With the exception of the centroid shown in Figure 6.12 (c), all share the three vibrational modes of pyrite plus additional peaks, where changes in the relative intensity from one pixel to another can be explained by the thickness of the patina. Nevertheless, narrow peaks at 982 or 1008 cm^{-1} are invariably present in the four centroids.

In particular, the peak at 1008 cm^{-1} could be attributed to the symmetric stretch vibrational mode (ν_1) of SO_4^{2-} tetrahedra, which could be explained by the presence of traces of $\text{CaSO}_4 \cdot 2\text{H}_2\text{O}$ (gypsum) on the surface.

The peak at 982 cm^{-1} may be related to the presence of different alkaline sulfates depending on the number of hydration waters. Unfortunately, the spectral range recorded does not include the region where the secondary bands allow the proper identification of these sulfates. However, this approach could be used as a first approximation of these spatially distributed minor features (pixels associated with the presence of SO_4^{2-} compounds) and once identified, a new hyperspectral image could be acquired focusing on that area of interest but this time increasing the spectral range and changing some of the parameters for a better characterization of the secondary vibrational modes.

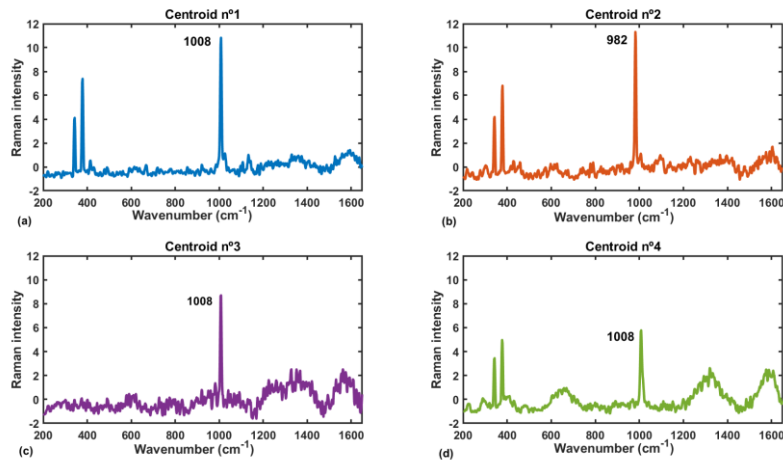


Figure 6.12. Centroids found after K-means clustering analysis of the minor features dataset.

6.4.5 Compositional images

As previously mentioned, two compositional images were created based on the information extracted from the analysis of major and minor features:

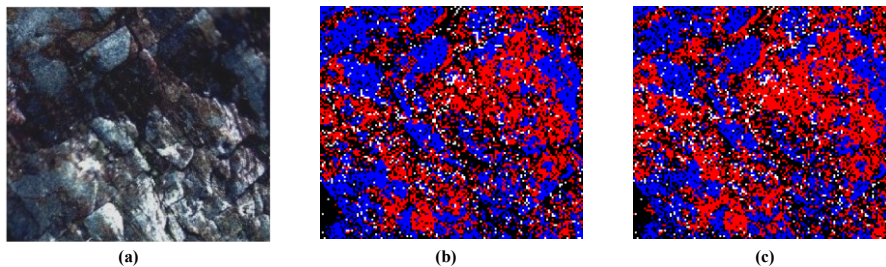


Figure 6.13. Real image of the analyzed surface (a) and composite images (b) and (c). Pixels belonging to component 1 are colored in blue, those to component 2 in red and those to component 3 in black. Pixels related to minor features are colored in white.

Semi-quantitative assessment of the spatial distribution of different mineralogical phases is summarized in Table 6.1. As can be observed, the percentage of surface area that corresponds to pyrite is very similar for both models. A similar situation is found for the percentage of low crystalline compounds on the surface. However, the difference in the percentage of hematite between the two models is greater.

Table 6.1. Distribution of the different mineralogical phases in the two MCR-ALS models (using a Raman library or the pure variable selection method for the initial estimation of the spectral profiles).

MCR-ALS model 1			
Color	Mineralogical phase	Pixels	% of the image
Blue	Pyrite	4753	26.4
Red	Hematite	5831	32.4
Black	Amorphous	6589	36.6
White	Sulfates	830	4.6

MCR-ALS model 2			
Color	Mineralogical phase	Pixels	% of the image
Blue	Pyrite	5306	29.5
Red	Hematite	4773	26.5
Black	Amorphous	7094	39.4
White	Sulfates	830	4.6

6.5 Conclusions

The methodology presented in this study is schematically summarized in Figure 6.14. It proved to be a useful approach for the exploratory analysis of heterogeneous samples. In addition, it has demonstrated the importance of the pre-processing step when dealing with this kind of image. When small but important sources of variability as those of the sulfates found are present in an image, then a good strategy is the splitting of the data into two different datasets. A preliminary PCA analysis provides enough information for this discrimination between major and minor features. Then MCR-ALS is the best option for spectral unmixing of weathered samples, which characterization is usually difficult due to overlapping of the Raman signals. The calculated models provide chemical insights on the mineralogical composition of the samples, which allows for a threshold-based quantification of the extent of oxidation. The percentage of unweathered pyrite was only 8.7 %, the remaining mineralogical phases being hematite, amorphous carbon and a combination of pyrite modes with these two phases. In further studies carried out in this dissertation, part of the methodology proposed here will be employed for the assessment of the spatial distribution of weathering compounds on the surface of pyrite.

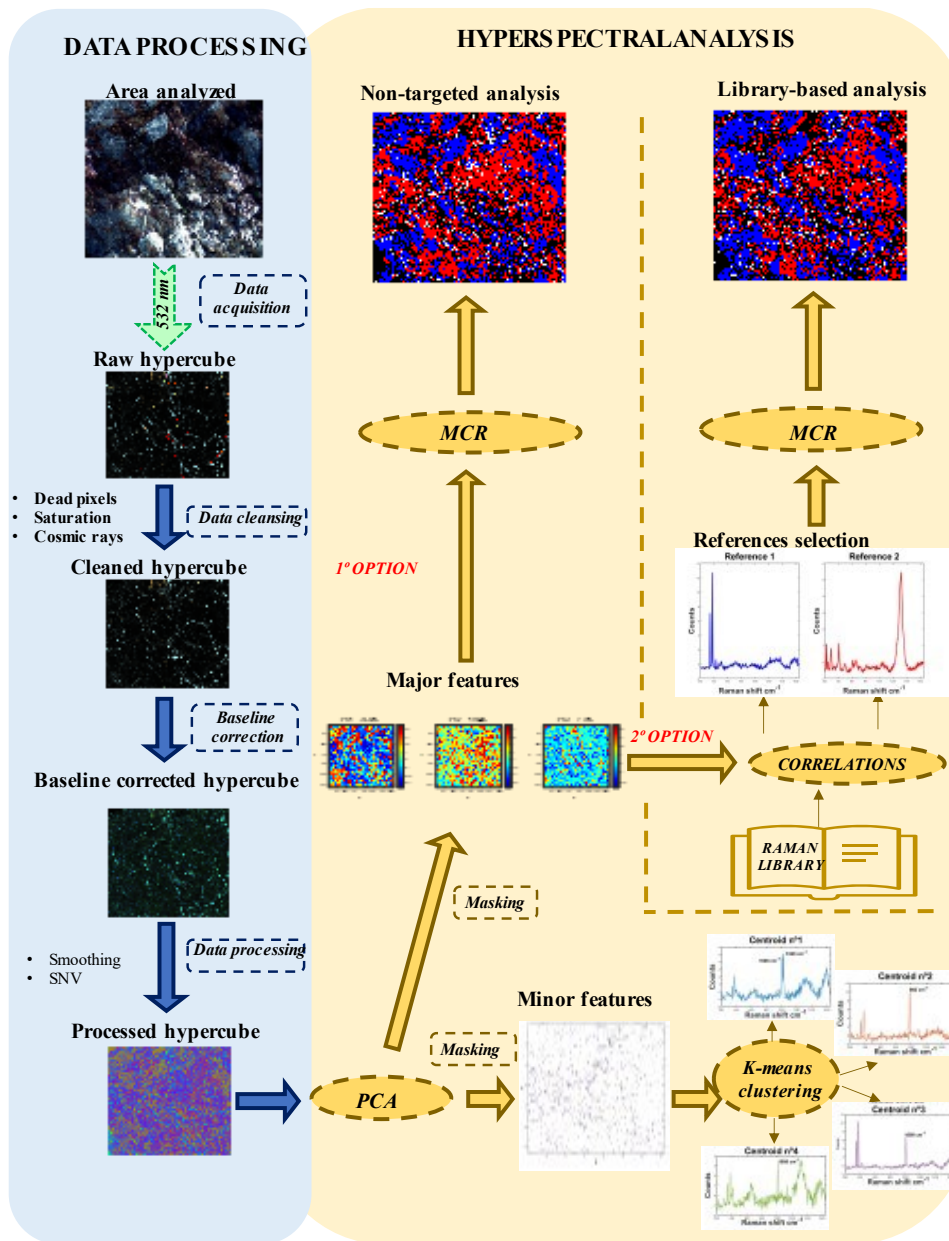


Figure 6.14. Scheme of the Chemometrics and Hyperspectral imaging approach proposed in the study.

Chapter: Data-driven simulation of oxidative weathering of pyrite

7

” *I think that in the discussion of natural problems we ought to begin not with the Scriptures, but with the experiments and demonstrations.*

— Galileo Galilei

In the last decades, many studies have been carried out on the Oxidative weathering of pyrite. Although several reactions and alteration products are involved, different mechanisms have been proposed based on experimental evidence. In particular, the acidification of the environment due to pyrite oxidation is of great importance in many sectors due to the problems it causes. Many of the experiments performed to evaluate the mechanism of weathering or the products generated focused on the influence of a few variables. However, due to the complexity of this mechanism, the degree of pyrite oxidation can be affected by the interaction of a multitude of chemical, physical and biological factors.

Chemometrics has proven to be a valuable tool not only in chemistry, but in many different fields. It offers a multitude of analysis methods for both data exploration and machine learning, whether to perform classification or regression tasks. Unfortunately, many experiments are still performed following the traditional univariate approach, without taking advantage of the tools it can offer for experimental design based on multivariate analysis.

In this regard, this study presents a series of data-driven experiments for the screening of different factors and the assessment of their influence on the oxidative weathering of pyrite in extreme acidic conditions. In this multivariate approach based on the Design of the Experiments, the factors studied are mainly related to major ion water chemistry. A Plackett-Burman design was followed, and regression models were calculated to estimate the significance of the evaluated factors. In addition, the surface of the samples was analyzed by hyperspectral Raman imaging to characterize the spatial distribution of the main weathering product.

7.1 Materials and methods

7.1.1 Sample

The samples used in the experiments were 19 dodecahedral pyrite crystals from Val Trebbia (Piacenza, Italy). The diameter of the samples ranges from 1 to 3 mm and the shape is almost the same in all crystals, as shown in Figure 7.1.



Figure 7.1. Pyrite samples used in the experiments carried out.

7.1.2 Reagents

Hydrochloric acid (fuming 37%), methanol (HPLC grade) and ethanol (ACS grade) were purchased from Carlo Erba (Milan, Italy). Chloride, fluoride, nitrogen, sulfate, and phosphate (ion chromatography standards), as well as, calcium, magnesium, sodium, potassium, strontium (ICP-OES standards), carbon disulfide (ACS grade) and iron nitrate nonahydrate (ACS grade) were purchased from Chem-Lab (Zedelgem, Belgium). Perchloroethylene (HPLC grade) was purchased from Honeywell (Milan, Italy). Silicon (ICP-OES standard), elemental sulfur (99.998% purity) and humic acid sodium salt, were purchased from Sigma-Aldrich (Milano, Italy). Ultrapure water was produced by a Millipore Milli-Q system (Milford, USA).

7.1.3 Instrumentation

Water soluble inorganic anions (Cl^- , F^- , NO_3^- and SO_4^{2-}) were determined using a Dionex ICS-2000 IC (Thermo Fisher, Italy) system. This was equipped with an Ion Pac AS14A-5 μm column (Thermo Fisher, Italy), a guard column AG14A-5 μm and a CCD array detector.

Metal elements (Na, K, Ca, Mg, Si, Sr, and Fe) were determined by using an ICP OES Optima 7000 DV (PerkinElmer, Italy) system.

Elemental sulfur was determined with an HPLC-DAD Infinity 1260 (Agilent, Italy) system. This was equipped with a Zorbax Eclipse C18 (150 x 4.6 mm, 3.5 μm) column (Agilent, Italy).

The Raman spectrometer used for the acquisition of the spectra has been already described in Chapter 5. The acquisition conditions were as follows: 5% power of the laser, slit opening 65 μm , exposure time 0.5 s and number of accumulations equal to 3. The spectral range was 145-1912 cm^{-1} . The average spectral resolution was 1.7 cm^{-1} , with a total number of points per spectrum equal to 1015.

7.1.4 Software

MATLAB R2022b (*MathWorks, Massachusetts, USA*) was used for dataset preparation and data pre-processing operations. Regression toolbox [132] was used for the calculation of regression models to evaluate the results of the experimental design. HYPER-Tools 3.0 toolbox [124] was used for exploratory analysis of the hyperspectral images. In-house codes were created in MATLAB environment for cosmic spikes removal and construction of the final images.

7.1.5 Experimental design

A Design of Experiments (DoE) methodology was employed for the screening of 13 different factors. In order to evaluate the influence of these factors on the OWP in acidic environments, elemental sulfur was extracted, quantified and considered as the response. The selection of the response was based on the fact that, under acidic conditions, ferric iron will be the oxidant of pyrite, leading to the generation of elemental sulfur *via* thiosulfate pathway, which is deposited on the surface of the crystals. Table 7.1 summarizes the evaluated factors and the experimental domain, which has been delimited according to the major ion water chemistry of some rivers around the world [133–138].

Table 7.1. Experimental domain of the screened factors in the Plackett-Burman design.

Factor	Level	Unit
Fe	2 to 50	mg L ⁻¹
Ca	16 to 19	mg L ⁻¹
Mg	9 to 10	mg L ⁻¹
Sr	0.06 to 0.08	mg L ⁻¹
Si	15 to 22	mg L ⁻¹
Cl ⁻	1 to 2	mg L ⁻¹
SO ₄ ²⁻	14 to 17	mg L ⁻¹
F ⁻	5 to 6	mg L ⁻¹
Size	<2 or >2	mm
Humic acid	0 to 100	mg L ⁻¹
Na	Uncontrolled	mg L ⁻¹
K	Uncontrolled	mg L ⁻¹
NO ₃ ⁻	Uncontrolled	mg L ⁻¹

Table 7.2. Experimental plan with K= 13 factors and N= 16 experiment (plus 3 central replicates). Green and cell mean a high and low level for that experiment, respectively. All reported factors are in mg.L⁻¹, except for Size which unit is mm. Sample labels N1 to N16 will be used hereafter.

	Fe	Humic acid	Ca	Mg	Sr	Si	Cl ⁻	SO ₄ ²⁻	F ⁻	Size	Na	K	NO ₃ ⁻
N1	50	0	16	9	0.08	15	1	17	6	>2 mm	UNCONTROLLED FACTORS		
N2	50	100	16	9	0.06	22	1	14	6	<2 mm			
N3	50	100	19	9	0.06	15	2	14	5	>2 mm			
N4	50	100	19	10	0.06	15	1	17	5	>2 mm			
N5	2	100	19	10	0.08	15	1	14	6	<2 mm			
N6	50	0	19	10	0.08	22	1	14	5	<2 mm			
N7	2	100	16	10	0.08	22	2	14	5	>2 mm			
N8	50	0	19	9	0.08	22	2	17	5	<2 mm			
N9	50	100	16	10	0.06	22	2	17	6	<2 mm			
N10	2	100	19	9	0.08	15	2	17	6	<2 mm			
N11	2	0	19	10	0.06	22	1	17	6	>2 mm			
N12	50	0	16	10	0.08	15	2	14	6	>2 mm			
N13	2	100	16	9	0.08	22	1	17	5	>2 mm			
N14	2	0	19	9	0.06	22	2	14	6	>2 mm			
N15	2	0	16	10	0.06	15	2	17	5	<2 mm			
N16	2	0	16	9	0.06	15	1	14	5	<2 mm			
C1	26	50	17.5	9.5	0.07	18.5	1.5	15.5	5.5	<2 mm			
C2	26	50	17.5	9.5	0.07	18.5	1.5	15.5	5.5	<2 mm			
C3	26	50	17.5	9.5	0.07	18.5	1.5	15.5	5.5	<2 mm			

Experimental domains of humic acids, ferric iron concentration and size were established from experience gathered in preliminary experiments carried out. On the other hand, sodium, potassium and nitrate were considered as uncontrolled factors due to their presence as counterions in the reagents used.

A Plackett-Burman design was selected, so each factor was analyzed at two levels. Therefore, 16 unique experiments (samples N1 to N16) plus 3 central point replicates (samples C1 to C3, same experimental conditions) were

conducted, making a total of 19 experiments. The experimental plan followed is shown in Table 7.2.

7.1.6 Experimental procedure and setup

Before starting the experiments, each sample was chemically treated to obtain a surface similar to that of pristine. The treatment is as follows:

1. Samples were washed in ethanol using an ultrasonic bath for 30 minutes. This way added particles and/or organic matter onto the surface are removed.
2. Then, samples were immersed in a 1.5 M HCl solution overnight to remove any oxidation layer. Some studies [139] suggest this procedure to adequately prepare samples for oxidation studies, as the resulting surface exhibits a similar reactivity to that of cleaved pyrite after this treatment.
3. Finally, samples are treated for 2 hours with carbon disulfide to remove any previous elemental sulfur on the surface.

To check the success of this chemical treatment, the surface of some samples was analyzed by acquiring some single-point Raman spectra, resulting in all cases in the three vibrational modes of pyrite at ca. 343, 378 and 429 cm^{-1} , which means that the treatment eliminated all the exogenous compounds. In addition, one of the samples was randomly selected and after choosing a recognizable area, a Raman map was acquired. This procedure was repeated on the same sample after completion of the weathering experiments, to check whether the proposed experimental setup produces noticeable changes on the surface.

The experimental setup was as follows:

1. Pre-treated samples were weighed with an analytical balance and then grouped according to the Size factor.
2. Several solutions equal to the number of experiments were prepared by adjusting the volume of the fresh stock solution to be added in order to obtain a final concentration equal to that of the experimental plan (Table 7.2) for each sample.
3. Then 10 mL of each solution was transferred into a borosilicate glass vial for the weathering experiments, keeping the same

volume stored at 3 °C in another vial. Thus, the solution of each sample before and after the completion of the experiments (hereinafter referred to as t_0 and t_f , respectively) was analyzed to check for chemical changes during the oxidation of pyrite.

4. Finally, the pre-treated pyrite crystals were immersed in their solutions. Each vial was purged with a nitrogen steam to remove as much dissolved oxygen as possible. To do this, a septum with two syringes as in-let out-let was placed to facilitate the removal of the purge procedure. Vials were closed with the cap and parafilm was added to the exterior of the vials to minimize cross-contamination in case of an accidental drop of the vials, which were placed in a recipient full of silicon oil thermal fluid. This recipient was placed in a hotplate at controlled temperature (42 °C) to mimic extreme AMD conditions [140].

In this way, the system was left evolving for 2 months. The temperature of the vials was periodically controlled to prevent overheating. In addition, each vial was shaken manually. The use of stirring bars was avoided to not damaging or breaking the crystals into smaller fragments.

7.2 Results

7.2.1 Ion chromatography analysis

For the determination of the anionic concentration of the t_0 and t_f samples, an 8 mM Na_2CO_3 / 1 mM NaHCO_3 mixture was used as eluent. The flow rate was $0.5 \text{ mL}\cdot\text{min}^{-1}$. The linear concentration of each anion was covered during calibration. Following an isocratic gradient, a good separation of the analytes was achieved after 20 minutes. The area of the peaks was manually selected by the same operator and used as the analytical parameter. For quantification, three replicates of each sample were analyzed, and the average value was provided. In the case of SO_4^{2-} , additional dilutions were needed for the quantification of the t_f samples. The results are provided in Table 7.3.

Table 7.3. Results of the Ion chromatography analyses reported as the mean value \pm standard deviation of the mean. Samples N1 to N16 refer to the samples of the weathering experiments, whereas C1 to C3 are the central point samples.

SAMPLE	F ⁻ mg L ⁻¹	Cl ⁻ mg L ⁻¹	NO ₃ ⁻ mg L ⁻¹	SO ₄ ²⁻ mg L ⁻¹
t ₀ -N1	6.4 ± 0.6	2.0 ± 0.1	291.4 ± 9.8	17.2 ± 0.9
t ₀ -N2	5.3 ± 0.2	1.0 ± 0.0	287.4 ± 8.9	15.1 ± 8.2
t ₀ -N3	4.6 ± 1.0	2.0 ± 0.1	319.4 ± 13.2	14.2 ± 0.8
t ₀ -N4	5.3 ± 0.9	0.9 ± 0.0	324.4 ± 15.0	17.3 ± 0.9
t ₀ -N5	4.8 ± 1.2	1.4 ± 0.1	286.4 ± 13.4	14.0 ± 0.9
t ₀ -N6	4.8 ± 0.8	0.8 ± 0.1	326.4 ± 12.8	14.2 ± 0.9
t ₀ -N7	6.4 ± 0.3	1.9 ± 0.1	267.2 ± 9.4	14.5 ± 0.7
t ₀ -N8	4.8 ± 0.9	1.9 ± 0.1	322.1 ± 14.6	17.3 ± 1.1
t ₀ -N9	6.2 ± 6.5	1.9 ± 0.1	302.1 ± 11.4	18.2 ± 1.0
t ₀ -N10	5.3 ± 1.1	1.8 ± 0.1	272.5 ± 14.3	17.2 ± 1.0
t ₀ -N11	5.0 ± 2.3	1.2 ± 0.4	107.1 ± 106.6	18.5 ± 6.7
t ₀ -N12	5.8 ± 1.3	2.0 ± 0.6	176.3 ± 96.1	13.0 ± 5.0
t ₀ -N13	5.5 ± 1.7	0.9 ± 0.1	260.2 ± 9.2	17.3 ± 0.9
t ₀ -N14	5.9 ± 0.8	1.8 ± 0.0	288.3 ± 12.1	14.2 ± 1.0
t ₀ -N15	4.6 ± 0.9	1.9 ± 0.1	266.3 ± 9.7	17.3 ± 1.0
t ₀ -N16	6.0 ± 0.1	0.8 ± 0.0	259.1 ± 8.8	14.5 ± 0.7
t ₀ -C1	5.6 ± 19.2	1.7 ± 0.5	280.1 ± 75.5	15.4 ± 5.8
t ₀ -C2	5.7 ± 2.6	1.4 ± 0.2	289.5 ± 74.7	15.1 ± 4.6
t ₀ -C3	4.6 ± 7.9	1.4 ± 0.3	295.4 ± 52.6	16.0 ± 4.4
t _f -N1	17.5 ± 0.4	1.0 ± 0.1	214.3 ± 7.1	1545.5 ± 23.3
t _f -N2	n.d.	1.2 ± 0.0	299.2 ± 11.0	55.5 ± 2.3
t _f -N3	3.2 ± 0.4	2.1 ± 0.0	283.4 ± 11.3	722.1 ± 26.4
t _f -N4	1.2 ± 0.0	1.1 ± 0.0	226.1 ± 57.5	537.1 ± 143.4
t _f -N5	1.1 ± 0.2	2.5 ± 0.1	371.3 ± 13.2	31.4 ± 1.8
t _f -N6	3.4 ± 0.7	1.4 ± 0.0	333.3 ± 12.1	278.2 ± 13.7
t _f -N7	1.4 ± 0.1	0.1 ± 0.1	210.0 ± 8.9	21.5 ± 7.4
t _f -N8	2.1 ± 2.0	1.1 ± 0.4	241.5 ± 56.4	239 ± 89.1
t _f -N9	2.1 ± 0.4	2.4 ± 0.0	298.4 ± 19.9	87.2 ± 7.1
t _f -N10	1.3 ± 0.2	2.3 ± 0.0	287.1 ± 10.3	28.2 ± 1.8
t _f -N11	1.4 ± 0.2	1.3 ± 0.0	299.2 ± 10.6	238.2 ± 9.9
t _f -N12	25.3 ± 6.1	2.3 ± 0.3	222.3 ± 34.2	1196.1 ± 188.6
t _f -N13	13.4 ± 0.7	3.4 ± 0.1	264.4 ± 10.9	47.2 ± 2.2
t _f -N14	3.4 ± 0.3	2.4 ± 0.0	290.3 ± 9.2	363.2 ± 15.4
t _f -N15	9.0 ± 0.3	2.2 ± 0.1	292.2 ± 15.4	33.1 ± 1.8
t _f -N16	8.1 ± 3.9	1.4 ± 0.0	256.3 ± 10.9	90.4 ± 6.0
t _f -C1	3.2 ± 26.2	2.4 ± 0.1	292.2 ± 29.3	83.0 ± 11.5
t _f -C2	1.5 ± 0.4	1.2 ± 0.1	297.0 ± 38.2	76.4 ± 15.4
t _f -C3	18.1 ± 1.4	1.0 ± 0.1	298.1 ± 49.7	98.1 ± 24.2

7.2.2 Inductively coupled plasma-optical emission spectroscopy analysis

For the metallic determination of each sample, calibration was performed by measuring the intensity of the emission wavelength lines that provide the maximum signal intensity and minimal interferences. These lines for Na, K, Ca, Mg, Si, Sr, and Fe were 589.592, 766.490, 393.366, 280.271, 251.611, 407.771 and 238.204 nm, respectively. Samples were diluted in HNO₃ (1% v/v). Three replicates of each sample were analyzed, and the average value was provided. Results are shown in Table 7.4.

Table 7.4. Results of the ICP-OES analyses reported as the mean value \pm standard deviation of the mean. Samples N1 to N16 refer to the samples of the weathering experiments, whereas C1 to C3 are the central point samples. The Fe factor is the total concentration of Fe^{2+} and Fe^{3+} , although it is expected that almost all the iron at t_0 is present as Fe^{3+} due to the very low pH of the solutions.

SAMPLE	Fe mg L ⁻¹	Ca mg L ⁻¹	Mg mg L ⁻¹	Sr μ g L ⁻¹	Si mg L ⁻¹	Na mg L ⁻¹	K mg L ⁻¹
t_0 -N1	49.3 \pm 0.4	16.1 \pm 0.2	9.30 \pm 0.02	0.0600 \pm 0.0002	14.9 \pm 0.0	n.d.	7.20 \pm 0.01
t_0 -N2	49.0 \pm 0.2	15.2 \pm 0.2	9.10 \pm 0.02	0.0800 \pm 0.0005	18.9 \pm 0.0	4.0 \pm 0.1	7.00 \pm 0.02
t_0 -N3	48.5 \pm 0.2	19.0 \pm 0.1	9.40 \pm 0.01	0.0600 \pm 0.0002	16.9 \pm 0.1	n.d.	7.00 \pm 0.01
t_0 -N4	48.6 \pm 0.1	19.1 \pm 0.0	10.00 \pm 0.02	0.0600 \pm 0.0002	17.8 \pm 0.2	n.d.	6.90 \pm 0.01
t_0 -N5	2.4 \pm 0.0	19.2 \pm 0.1	10.10 \pm 0.01	0.0800 \pm 0.0003	24.0 \pm 0.2	1.4 \pm 0.0	7.40 \pm 0.02
t_0 -N6	49.7 \pm 0.4	18.4 \pm 0.1	10.10 \pm 0.02	0.0600 \pm 0.0005	17.2 \pm 0.1	n.d.	6.40 \pm 0.01
t_0 -N7	2.1 \pm 0.0	16.8 \pm 0.0	10.10 \pm 0.01	0.0800 \pm 0.0004	25.0 \pm 0.2	n.d.	7.60 \pm 0.05
t_0 -N8	49.1 \pm 0.1	18.5 \pm 0.0	9.20 \pm 0.01	0.0600 \pm 0.0004	16.8 \pm 0.1	n.d.	7.50 \pm 0.02
t_0 -N9	48.9 \pm 0.1	16.3 \pm 0.0	9.90 \pm 0.02	0.0600 \pm 0.0002	16.9 \pm 0.0	1.9 \pm 0.0	7.30 \pm 0.03
t_0 -N10	2.0 \pm 0.1	18.3 \pm 0.1	9.10 \pm 0.02	0.0800 \pm 0.0004	22.5 \pm 0.1	n.d.	7.30 \pm 0.01
t_0 -N11	1.8 \pm 0.0	18.2 \pm 0.0	9.90 \pm 0.03	0.0500 \pm 0.0002	22.1 \pm 0.1	n.d.	6.70 \pm 0.01
t_0 -N12	50.7 \pm 0.1	15.1 \pm 0.1	9.80 \pm 0.02	0.0600 \pm 0.0005	12.6 \pm 0.1	n.d.	6.40 \pm 0.00
t_0 -N13	2.1 \pm 0.0	16.1 \pm 0.1	9.10 \pm 0.01	0.0800 \pm 0.0001	25.0 \pm 0.2	n.d.	7.00 \pm 0.01
t_0 -N14	1.9 \pm 0.1	17.1 \pm 0.1	9.00 \pm 0.02	0.0500 \pm 0.0003	21.4 \pm 0.1	n.d.	6.40 \pm 0.00
t_0 -N15	2.0 \pm 0.1	15.8 \pm 0.2	9.90 \pm 0.02	0.0500 \pm 0.0001	20.0 \pm 0.1	n.d.	6.40 \pm 0.01
t_0 -N16	2.2 \pm 0.1	15.6 \pm 0.0	9.10 \pm 0.01	0.0500 \pm 0.0001	20.2 \pm 0.1	n.d.	6.40 \pm 0.00
t_0 -C1	25.9 \pm 0.5	18.9 \pm 0.2	9.7 \pm 0.0	0.0800 \pm 0.0010	21.7 \pm 1.1	n.d.	7.1 \pm 0.0
t_0 -C2	25.7 \pm 1.7	16.8 \pm 0.2	9.5 \pm 0.2	0.0600 \pm 0.0020	18.8 \pm 0.4	n.d.	6.9 \pm 0.0
t_0 -C3	26.5 \pm 0.9	16.5 \pm 0.3	9.5 \pm 0.1	0.0600 \pm 0.0020	19.8 \pm 0.4	n.d.	6.8 \pm 0.1
t_f -N1	480.0 \pm 0.7	18.0 \pm 0.0	8.60 \pm 0.04	0.0800 \pm 0.0001	26.4 \pm 0.1	1.3 \pm 0.0	7.00 \pm 0.02
t_f -N2	60.0 \pm 0.1	18.6 \pm 0.0	8.60 \pm 0.00	0.0800 \pm 0.0003	46.1 \pm 0.3	9.4 \pm 0.1	8.30 \pm 0.05
t_f -N3	257.2 \pm 0.7	20.6 \pm 0.1	8.60 \pm 0.03	0.0800 \pm 0.0008	35.6 \pm 0.2	7.7 \pm 0.1	7.80 \pm 0.00
t_f -N4	278.3 \pm 0.5	21.8 \pm 0.1	10.60 \pm 0.01	0.0800 \pm 0.0008	34.8 \pm 0.3	7.5 \pm 0.1	8.20 \pm 0.01
t_f -N5	8.7 \pm 0.1	27.6 \pm 0.1	12.00 \pm 0.06	0.1200 \pm 0.0002	77.4 \pm 0.5	15.3 \pm 0.2	9.40 \pm 0.03
t_f -N6	135.2 \pm 0.3	19.8 \pm 0.0	10.40 \pm 0.03	0.0800 \pm 0.0003	29.7 \pm 0.1	0.9 \pm 0.0	5.70 \pm 0.01
t_f -N7	6.5 \pm 0.1	19.3 \pm 0.1	10.70 \pm 0.05	0.1000 \pm 0.0003	66.9 \pm 0.3	12.1 \pm 0.3	9.30 \pm 0.01
t_f -N8	149.2 \pm 0.4	19.5 \pm 0.1	9.40 \pm 0.03	1.0800 \pm 0.0002	32.7 \pm 0.2	2.3 \pm 0.0	7.00 \pm 0.01
t_f -N9	74.0 \pm 0.2	17.7 \pm 0.1	10.40 \pm 0.04	0.0800 \pm 0.0006	45.2 \pm 0.3	8.5 \pm 0.1	7.50 \pm 0.01
t_f -N10	6.2 \pm 0.1	21.8 \pm 0.1	9.70 \pm 0.02	1.1000 \pm 0.0006	64.8 \pm 0.3	13.2 \pm 0.1	8.30 \pm 0.03
t_f -N11	67.6 \pm 0.2	20.3 \pm 0.3	11.40 \pm 0.02	0.0600 \pm 0.0002	50.8 \pm 0.0	2.8 \pm 0.1	7.10 \pm 0.01
t_f -N12	455.7 \pm 0.7	12.9 \pm 0.4	9.60 \pm 0.05	0.0800 \pm 0.0006	43.9 \pm 0.5	n.d.	6.50 \pm 0.02
t_f -N13	9.2 \pm 0.0	19.4 \pm 0.1	9.60 \pm 0.02	0.1000 \pm 0.0002	70.2 \pm 0.2	10.7 \pm 0.1	8.50 \pm 0.01
t_f -N14	102.5 \pm 0.2	20.0 \pm 0.1	9.40 \pm 0.01	0.0600 \pm 0.0006	66.9 \pm 0.5	2.7 \pm 0.1	6.80 \pm 0.02
t_f -N15	6.4 \pm 0.0	19.5 \pm 0.1	10.70 \pm 0.02	0.0800 \pm 0.0002	68.0 \pm 0.1	3.5 \pm 0.1	7.10 \pm 0.01
t_f -N16	22.8 \pm 0.3	18.5 \pm 0.4	9.60 \pm 0.02	0.0800 \pm 0.0002	51.6 \pm 0.1	n.d.	7.60 \pm 0.02
t_f -C1	72.0 \pm 36.7	19.3 \pm 0.2	5.0 \pm 0.1	0.1170 \pm 0.0030	49.4 \pm 0.5	15.5 \pm 0.7	2.2 \pm 0.0
t_f -C2	44.6 \pm 1.3	19.8 \pm 0.2	11.1 \pm 0.2	0.0800 \pm 0.0020	44.0 \pm 0.7	6.6 \pm 0.1	7.3 \pm 0.1
t_f -C3	48.0 \pm 1.9	18.8 \pm 0.7	10.0 \pm 0.0	0.0800 \pm 0.0020	44.6 \pm 0.4	4.1 \pm 0.4	7.5 \pm 0.0

7.2.3 Raman hyperspectral images

For the acquisition of images of each sample, the spatial resolution of the grid of analysis was 15 μ m in both X- and Y-directions. For each image, spectra were organized into a three-dimensional data matrix with dimensions 40 x 40 x 1015, being the first two the spatial dimensions (X and Y coordinates of each pixel) and the third the spectral dimension λ . The number of pixels of the resulting images was 1600.

Then, all images were assembled in an orderly fashion into a single image. This operation was possible because images do not represent all the elemental sulfur produced due to weathering, since only a small area of the surface was covered. However, it is possible to analyze all the images at the same time for the assessment of the spatial distribution of sulfur. A spatial

mask was used to distinguish between different samples in the assembled image.

Very low signal-to-noise ratio pixels were identified and masked by means of Hotelling's T^2 and Q residuals. Cosmic spikes and saturated spectra were corrected by an in-house code. Therefore, the number of left-out pixels was 2822 out of 25600. Baseline correction was performed by adapting the signal to an asymmetric truncated quadratic cost function of order 8 with a threshold of 0.1. These parameters were selected to avoid the creation of fake Raman signals. Savitzky-Golay smoothing was also performed with a polynomial degree of 2 and a 7-point window. Additive scattering effects were corrected by applying standard normal variate (SNV) normalization. Cosmic spike correction and the subsequent data analysis of the hyperspectral images were based on the methodology described in Chapter 6 of this dissertation.

7.2.4 Elemental sulfur quantification

For the extraction of the elemental sulfur produced after 2 months of weathering, each crystal separated from the solution. Laboratory tissues were used to carefully dry the samples. Then, each crystal was accurately weighed and stored in clean vials (all the Raman images described above were acquired at this point). The extraction procedure is as follows:

1. Each crystal was immersed in carbon disulfide for two hours.
2. Then, the crystals were discarded, and the carbon disulfide was evaporated using a nitrogen steam. All these operations were carried out with extreme caution under the laboratory hood and avoiding the use of light bulbs because of the high flammability and volatility of carbon disulfide. After evaporation, the remaining substance, presumably sulfur, crystallized on the walls of the vials.
3. Afterwards, perchloroethylene (2.5 mL) was added to the vials and left overnight under magnetic stirring.
4. To obtain experimental replicates from each sample, a total of three aliquots (0.5 mL) were placed in clean vials and then all the perchloroethylene was evaporated with a nitrogen steam.
5. Finally, 0.5 mL of methanol was added to each of the vials before analysis.

Stock solutions of elemental sulfur from 0.02 to 100 mg.L⁻¹ were prepared for calibration. The HPLC elution method was isocratic gradient during 5 minutes with a 95/5 MeOH/H₂O (v/v) mobile phase and 1 mL min⁻¹ flow. The sulfur peak was detected by selecting the 254 nm wavelength of the DAD at 3.44 min, with no other co-eluted peaks, as shown in Figure 7.2. Finally, the area of the peaks was calculated and used for sulfur quantification based on the calibration line.

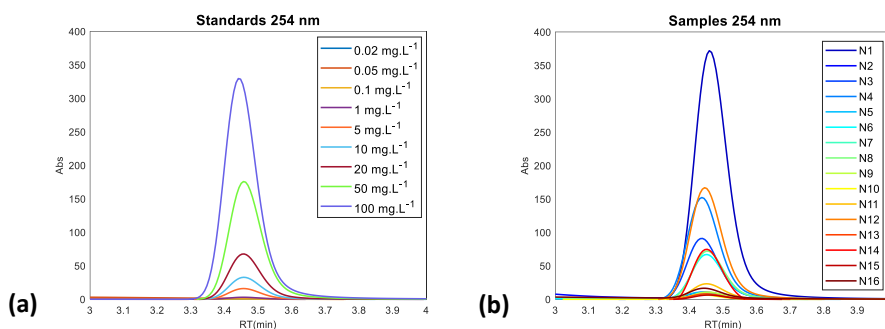


Figure 7.2. Overlapped chromatograms of sulfur standards (a) and samples (b) by operating at 254 nm.

The total amount of sulfur extracted is reported in Table 7.5, along with the mass loss for each crystal at the end of the experiment.

Table 7.5. Sulfur is reported as mean value \pm standard deviation of the mean. Mass loss is reported as the difference between t_0 and t_f .

Sample	$\mu\text{g S}^0$	$\Delta w(\text{mg})$
N1	305.4 ± 4.1	13.7
N2	7.7 ± 0.1	0.5
N3	114.6 ± 0.7	8.4
N4	124.8 ± 1.0	10.9
N5	6.6 ± 0.1	0.3
N6	52.1 ± 0.5	2.6
N7	6.6 ± 0.1	0.7
N8	56.0 ± 0.3	2.1
N9	8.2 ± 0.1	1
N10	4.7 ± 0.1	0.3
N11	17.3 ± 0.1	2.2
N12	278.4 ± 1.3	13.6
N13	5.9 ± 0.1	0.8
N14	68.4 ± 0.6	3.3
N15	4.7 ± 0.1	0.2
N16	10.9 ± 0.1	0.5

7.3 Discussion

7.3.1 Screening of the factors

Linear regression was calculated by means of Partial Least Squares (PLS), which finds the directions, also known as Latent Variables (LVs), that capture variance and maximize the covariance between the response and variable matrix. These LVs are linear combinations of the original variables. The model allowed us to estimate the significance of each factor based on the value of its coefficients in the PLS model, which provides information on the relationship of these factors and the elemental sulfur extracted. The higher the coefficient of each factor (in absolute value), the greater the influence of these factors.

Furthermore, two dummy factors were initially added to the design. These factors are associated with non-significant effects. Thus, the qualitative comparison of each coefficient with those of the dummy factors can be used to estimate the significance of the factors, as suggested in [141]. It is important to note that, in general, the values of each factor at t_0 (Table 7.3 and Table 7.4) are only slightly different from those proposed by the experimental matrix (Table 7.2), which is reasonable and acceptable as the solutions were manually prepared. However, there is one exception, that is the Si factor. It appears that important errors were introduced either during the preparation of the solutions or measurements. If these values are very different from that proposed by the experimental matrix, then the quality of the models will be very poor due to the lack of orthogonality in the Plackett-Burman design. To overcome this situation, the Si factor was discarded and substituted by a third dummy factor. In this way, we can maintain as much orthogonality as possible.

Therefore, the data were organized into a new dataset including t_0 values of 16 unique experiments (Table 7.3 and Table 7.4, samples N1 to N16), 1 central point (Table 7.3 and Table 7.4, samples C1 to C3) and 15 factors (after including dummy factors). Then, each column of the dataset was coded by normalizing the values as follow:

$$x_{ij(\text{coded})} = 2 \frac{x_{ij} - \min(x_j)}{\max(x_j) - \min(x_j)} - 1$$

where x_{ij} is the value of the i -th sample in the j -th factor j and x_j is the entire column of the j -th factor. The normalization of this dataset in the range between -1 and 1 prevents different scales from having a dissimilar effect on the response.

The remaining degrees of freedom (DoF) for the estimation of the confidence intervals of the coefficients (in PLS, there is no β_0 term) were calculated as:

$$DoF = N + C - K = 2$$

where N is the number of unique experiments (16), C is the number of repeated experiments (1 at the central point of the design), and K is the number of factors (15).

Confidence intervals for the β_k coefficients were calculated as follows:

$$\beta_k \pm t_{0.05, \nu} \cdot S \cdot \sqrt{c_{jj}}$$

where $t_{0.05, \nu}$ is the critical t-value at 95% for 2 DoF, S is the standard deviation of the response of the 3 replicates at the central point, and c_{jj} is the j -th diagonal element of the dispersion matrix D , which was calculated as $D = (X^T \cdot X)^{-1}$, being X the coded dataset.

To calculate the model, the amount of extracted sulfur was expressed in logarithmic scale. The number of selected latent variables (LVs) was 6 and autoscaling was performed on the data. The calculated standardized coefficients and their confidence limits are reported in Table 7.6. A graphical representation of the coefficients is also provided in Figure 7.3.

As can be observed, Fe, humic acids and Size factors can be considered as significant because they largely exceed the coefficient of the dummy factors. Moreover, they are the largest coefficients. The initial concentration of Fe and the size of the crystals have a positive influence in the generation of elemental sulfur, whereas the presence of humic acids has a negative influence, i.e., if the concentration of humic acids increases, then the amount of elemental sulfur produced will be lower.

Table 7.6. Standardized coefficients calculated by PLS regression and confidence limits.

Term	Coefficient	Confidence limit (95%)
Fe	0.69	± 0.05
Humic acids	-0.33	± 0.06
Ca	0.15	± 0.06
Mg	-0.2	± 0.04
Sr	0.13	± 0.07
Cl ⁻	0.06	± 0.03
SO ₄ ²⁻	-0.06	± 0.05
F ⁻	-0.12	± 0.05
Size	0.52	± 0.05
Na	-0.13	± 0.08
K	-0.21	± 0.10
NO ₃ ⁻	-0.12	± 0.12
Dummy 1	-0.24	±0.05
Dummy 2	0.04	± 0.04
Dummy 3	-0.11	± 0.04

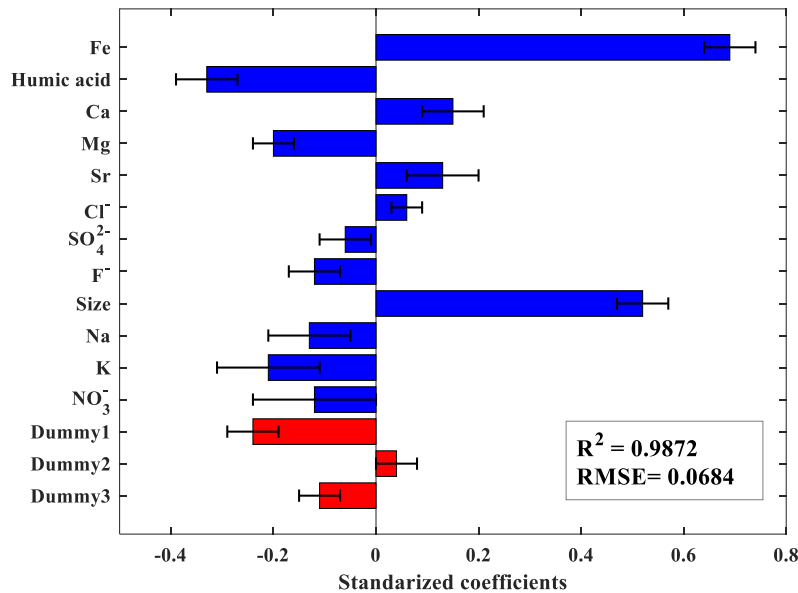


Figure 7.3. Coefficients of the PLS model calculated with 6 latent variables (LVs) over elemental sulfur amount (expressed in logarithmic scale) response.

On the other hand, it is interesting to analyze the evolution of each factor from t_0 to t_f to see if changes are somehow related to the oxidation mechanism. For this purpose, a new dataset was built joining the values of Table 7.3 and Table 7.4. The dimensions of the resulting dataset were 32 samples times 12 factors (Si and dummy factors excluded). The samples included were N1 to N16 at t_0 (16 in total) and N1 to N16 at t_f (16 in total). Central point samples were not considered in this analysis. A PCA model was calculated and scores and loading plots are reported in Figure 7.4.

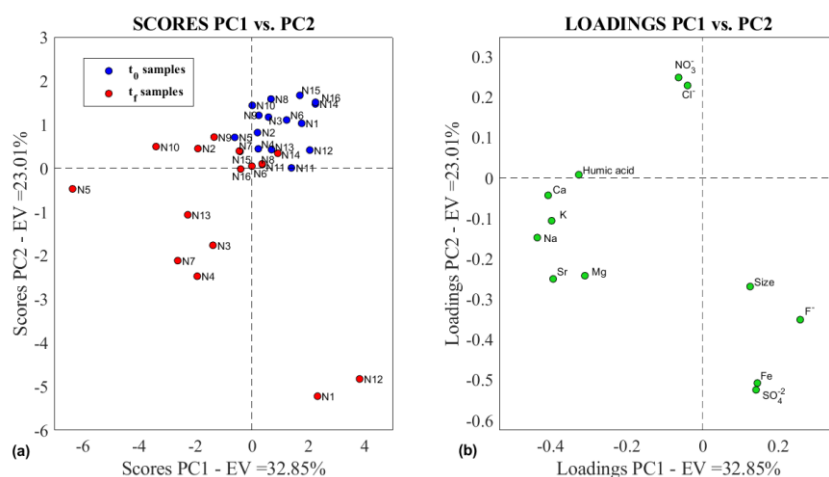


Figure 7.4. Scores (a) and loadings (b) plot using the real values of the factors as dataset, before and after the conclusion of the experiments

The first two PCs explain $\sim 56\%$ of data variance. Scores plot (Figure 7.4 a) shows that samples at t_f are more dispersed compared to the initial situation at t_0 , where samples are more clustered, as they follow the experimental plan. This dispersion at t_f can be attributed to relevant chemical changes in solution during the 2 months of weathering. On the one hand, PC2 explains the difference between N1 and N12 samples at t_f and the rest of the samples. It should be noted that N1 and N12 are the samples with the highest amount of extracted sulfur, as seen in Table 7.5. According to the loadings (Figure 7.4 b), this difference is mainly due to Fe and SO_4^{2-} factors. On the other hand, PC1 highlights differences between sample N5 at t_f (negative scores) and the rest of the samples, indicating a net increase of Na, K, Ca and Sr factors.

On the basis of these results, it was calculated the correlation between the difference of Fe and SO_4^{2-} factors at t_0 and t_f (e.g. $\Delta[\text{Fe}] = [\text{Fe}]_{t_f} - [\text{Fe}]_{t_0}$) and the amount of sulfur extracted. The same thing was done but against the mass loss of each crystal. Results are shown in Figure 7.5.

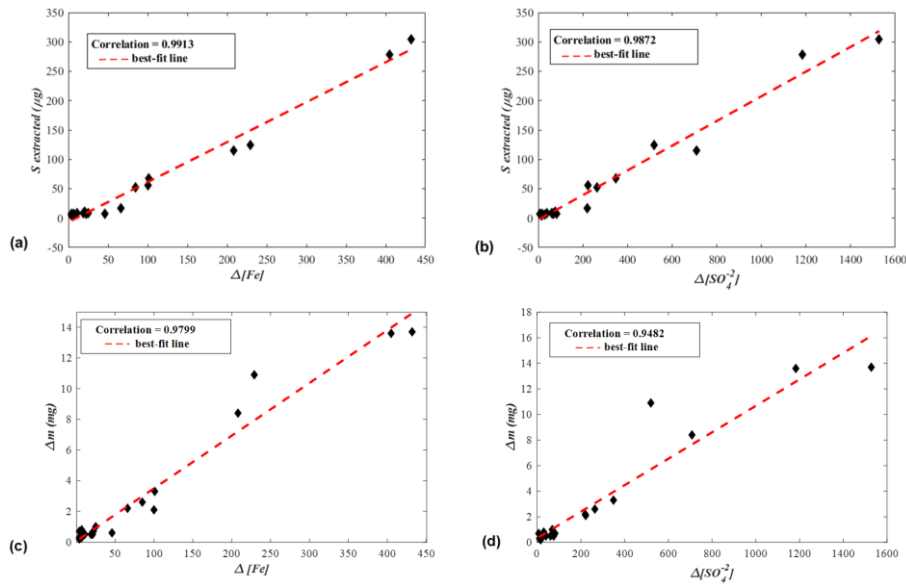


Figure 7.5. Correlation between (a) the difference of total Fe concentration and the amount of sulfur; (b) the difference of sulfate concentration and the amount of sulfur; (c) the difference of total Fe concentration and mass loss and (d) the difference of sulfate concentration and mass loss.

According to the correlation values shown in Figure 7.5 (a) and (b), it seems that the greater the elemental sulfur produced, the greater the difference between Fe and SO_4^{2-} . This has important chemical implications regarding the Fe speciation ($\text{Fe}^{2+}/\text{Fe}^{3+}$) and SO_4^{2-} production, as will be discussed in the next section. Similar results are obtained considering mass loss, which suggests that the amount of sulfur produced to some extent correlated with mass loss, as seen in Figure 7.6.

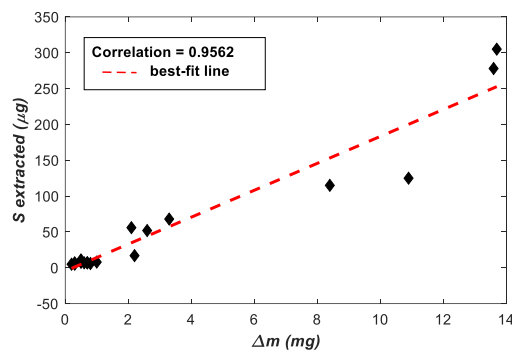


Figure 7.6. Correlation between the amount of sulfur and mass loss responses.

Finally, a new dataset like the previous one was built, but this time only including the difference between t_0 and t_f (in absolute value), so the dimensions are 16 samples times 12 factors. Again, the PCA model was calculated, and scores and loadings are shown in Figure 7.7.

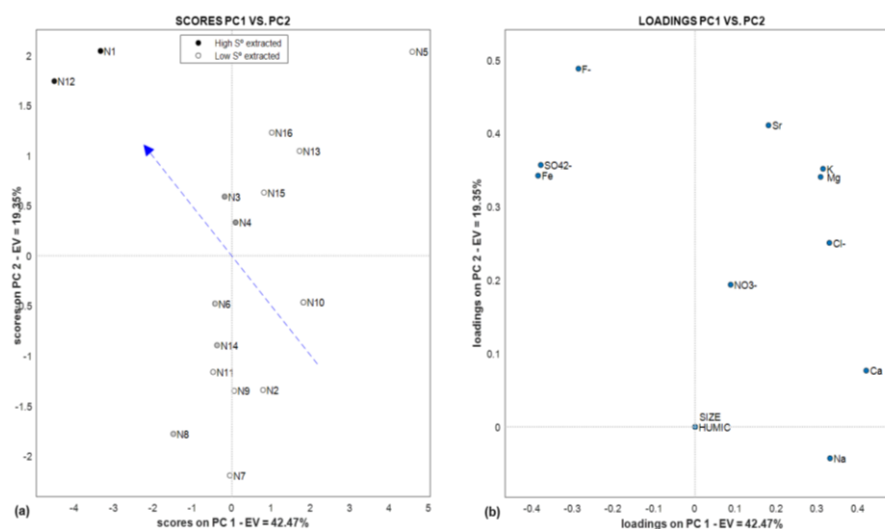


Figure 7.7. Scores (a) and loadings (b) plot considering each factor as the difference between t_0 and t_f . Samples are colored from white to black depending on the amount of sulfur.

The first two PCs explain ~62 % of data variance. It can be observed a trend on the amount of sulfur, from samples with positive and negative scores in PC1 and PC2, respectively, to the opposite situation, i.e. samples with negative and positive scores in PC1 and PC2, respectively. N1 and N12 samples are characterized by a net increment of Fe, SO₄²⁻ and F⁻ in solution.

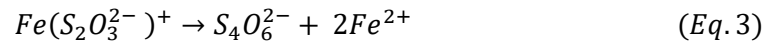
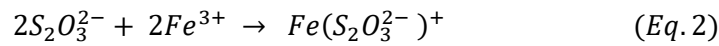
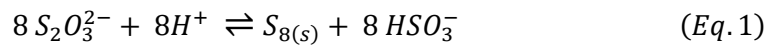
To summarize, a high concentration of Fe at t_0 generates remarkable amounts of elemental sulfur in pristine pyrite crystals, whereas the concentration of SO₄²⁻ at t_0 is not significant. However, when the concentration of both SO₄²⁻ and Fe is high at t_f , the amount of sulfur produced is also high. In other words, a high SO₄²⁻ and total Fe concentration in natural waters means that a large amount of sulfur will have been generated on pyrite surfaces.

7.3.2 Chemical discussion: effect of significant factors

Some assumptions can be made on the influence of the Fe factor, without taking into account electrochemical, surficial or photochemical considerations. It is worth mentioning that, in the experiments performed, the pH of the prepared solutions was below 1 in all cases, so that at t_0 , all Fe is expected to be in the Fe³⁺ state.

Fe³⁺ influence discussion. After decades of study regarding OWP, it is accepted that Fe³⁺ as oxidant and S₂O₃²⁻ as reaction intermediate are central

in the oxidation pathway of pyrite. In circumneutral pH waters, high amounts of polythionates ($S_xO_6^{2-}$) and $S_2O_3^{2-}$ are reported in the literature [46,142,143]. In contrast, in acidic waters of acid mine drainage locations, a rapid conversion of $S_2O_3^{2-}$ to $S_4O_6^{2-}$ and the further oxidation to SO_4^{2-} is observed [144,145]. When Fe^{3+} is in excess at pH=1.5 or lower, the conversion of $S_2O_3^{2-}$ to $S_4O_6^{2-}$ is almost complete [146]. However, if the Fe^{3+} is depleted, $S_xO_6^{2-}$ is the main product, but a generation of elemental sulfur is expected, which is formed by $S_2O_3^{2-}$ disproportionation [40,147,148]. This reaction, which is shown in Eq.1 is a reversible equilibrium and it is displaced to the right at pH below 2:



$S_2O_3^{2-}$ disproportionation competes against the reaction of $S_2O_3^{2-}$ with Fe^{3+} (Eq.2 and Eq.3), so Eq.1 only occurs when Fe^{3+} is depleted. This can be explained if, below pH 1.7, the oxidation by Fe^{3+} to form $S_4O_6^{2-}$ (which decomposes into SO_4^{2-}), is faster than $S_2O_3^{2-}$ disproportionation [147]. The kinetics of Eq.2 depends on the starting Fe^{3+} and $S_2O_3^{2-}$ concentration to form the $Fe(S_2O_3^{2-})^+$ complex. In addition, the HSO_3^- and $S_4O_6^{2-}$ generated in Eq.1 and Eq.3, respectively, react to form SO_4^{2-} in acidic solutions, which explains the great increment found after 2 months in most of the experiments carried out. In the literature, additional pathways for elemental sulfur formation are described [149–151]. These involve a S-enriched layer and S_n^{2-} intermediates, as described in [152].

Crystal size influence discussion. Since all the pyrite crystals used in the experiments have the same morphology, the significance of this factor can be explained on the basis of the reactive surface and the number of sites for $S_2O_3^{2-}$ formation. The larger the available surface for oxidation, the greater the amount of elemental sulfur produced. However, it should be also taken into account crystalline defects as they play an important role in OWP. The same applies for electron deficiency sites at the surface, which lead to different oxidation pathways and the involvement of hydroxyl radicals and water molecules [153–155].

Humic acid influence discussion. To explain the negative influence of this factor in the production of elemental sulfur, additional studies should be carried out to properly analyze the interaction of humic acids with the surface of pyrite crystals. The statistical analysis supports the hypothesis that under acid mine drainage conditions, this factor negatively influences the release of $S_2O_3^{2-}$ into solution, as commented above. However, in the literature the interaction of humic acids with the interface surface-solution was explained by electrochemical reactions, i.e., they are adsorbed on the surface and inhibits the production of elemental sulfur [156].

7.3.3 Raman hyperspectral image analysis

First, microscope images taken at t_0 and t_f of a randomly selected sample (N12) were compared to check whether the experimental setup generates evident changes, as commented in section 7.1.6. These images are shown in Figure 7.8 (a) and (b).

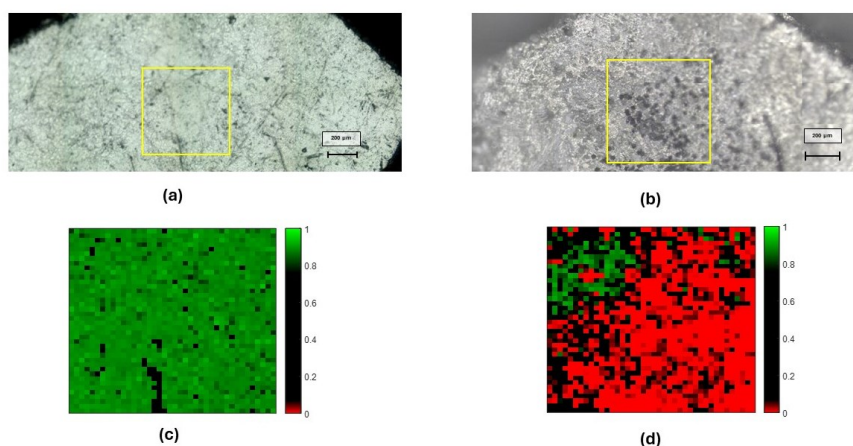


Figure 7.8. Real images of sample N12 at t_0 (a) and t_f (b). Pearson correlation model by using a pyrite reference spectrum at t_0 (c) and t_f (d).

To evaluate the success of the experimental setup, a Pearson correlation model with respect to a reference pyrite spectrum was calculated. If the experimental setup has been successful, weathering products other than pyrite should appear on the surface after 2 months of weathering. For this purpose, we used as a reference the average spectrum of all the pyrite samples from Val Trebbia included in the Raman library described in Chapter 5.

Sample N12 at t_0 , shows no other vibrational modes as those of pyrite (correlation coefficient higher than 0.8 for most of the pixels, Figure 7.8 c),

whereas the same surface at t_f (Figure 7.8 d) seems different, showing most of the pixels correlation coefficient values below 0.1. This means that, in effect, the experimental setup produced evident changes on the surface of the samples, as can also be seen by looking at the microscopic images in Figure 7.8 (a) and (b).

As commented in the previous sections of this chapter, the images of the rest of the samples acquired at t_f (before sulfur extraction) were merged into a single image and analyzed together. The objective is the assessment of the spatial distribution of elemental sulfur.

A PCA model was calculated and the score map and loadings for the first three PCs are shown in Figure 7.9.

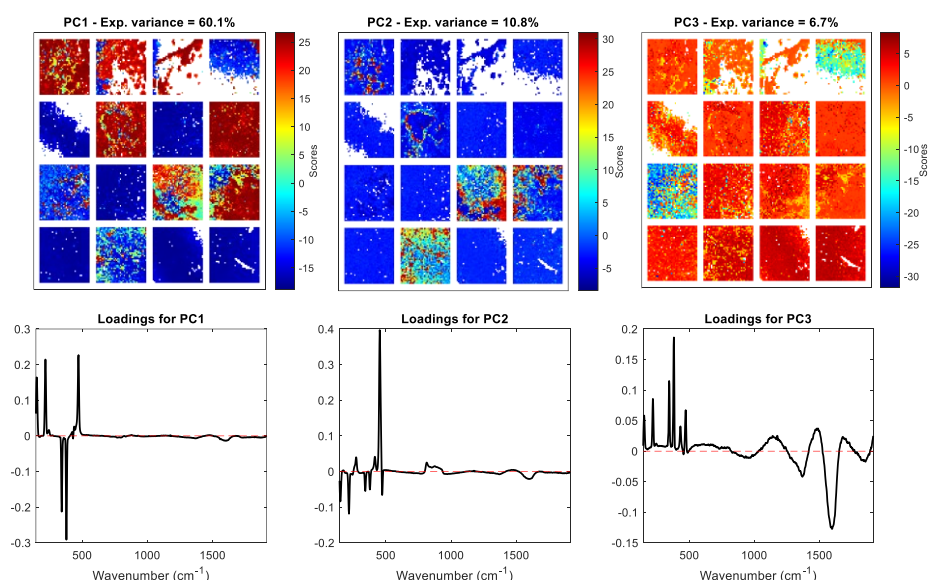


Figure 7.9. PCA score maps (upper) and loadings (bottom). From left to right and from up to down, samples N1 to N16.

These PCs explain $\sim 78\%$ of data variance. PC1 highlights differences between pixels characterized by 151, 218 and 471 cm^{-1} wavenumbers (positive scores) which are the vibrational modes of elemental sulfur, and peaks at 343 and 379 cm^{-1} (negative scores), which are two of the Raman modes of pyrite. Pixels with positive scores in PC2 are characterized by 272, 415 and 453 cm^{-1} . However, not a clear pattern was found for most of the pixels in PC3, except for those with very high positive scores which seem to be characterized by a combination of the peaks seen in the positive and negative loadings of PC1. Pixels with negative scores seem to be characterized by broad bands in the 1300-1700 cm^{-1} region, which could be

associated with amorphous or low-crystalline mineralogical phases, as already seen in Chapter 6.

The next step for the assessment of the spatial distribution of elemental sulfur was the calculation of Pearson correlation models using the spectrum of a high-purity elemental sulfur standard included in our Raman library and the same average spectra of pyrite (as previously done for sample N12). The results are shown in Figure 7.10 and Figure 7.11.

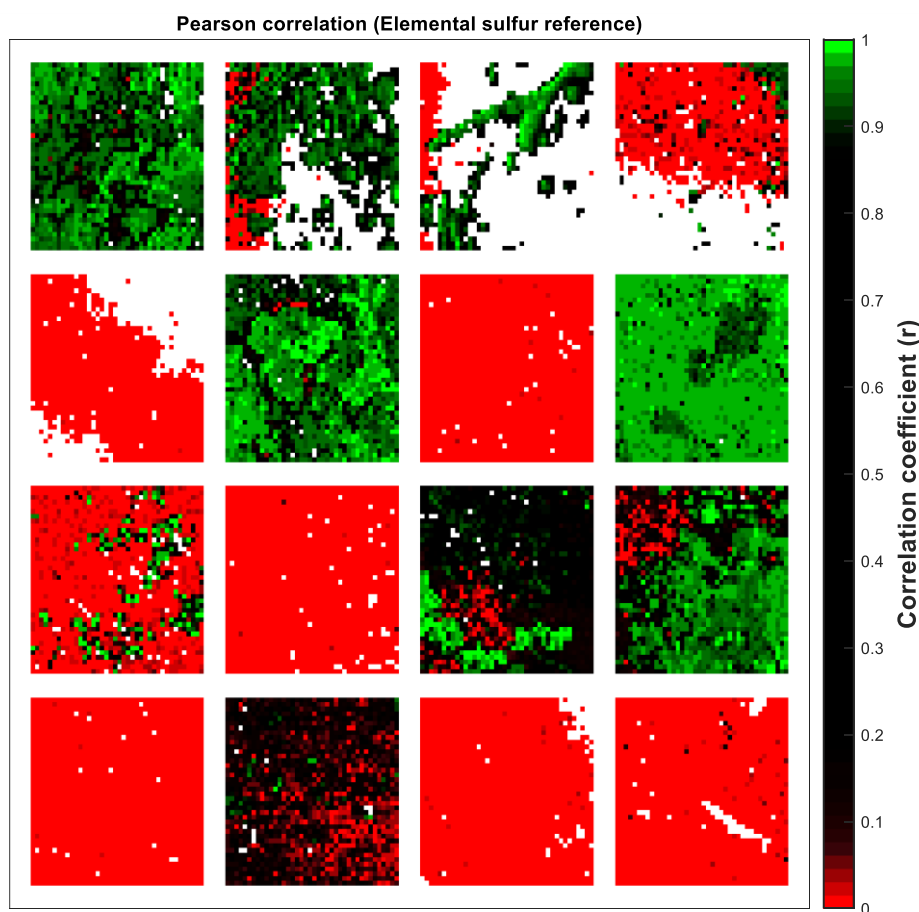


Figure 7.10. Pearson correlation calculated using an elemental sulfur reference spectrum. From left to right and from up to down, samples N1 to N16.

As can be seen in Figure 7.10, elemental sulfur homogeneously distributes across the surface of most of the samples, contrary to the conclusions of [63]. It is worth mentioning that the samples with the highest number of pixels with a high correlation coefficient (with respect to the sulfur spectrum) do not necessarily correspond to the samples with the highest amount of extracted sulfur. The explanation is that the analyzed sulfur covers only a small fraction of the surface of the crystals, since the aim was only to check how elemental sulfur is distributed. Nevertheless, elemental

sulfur covers patches of at least $600 \mu\text{m}^2$ in samples N1, N6 and N8, taking into account the scale and the dimension of the images. Furthermore, it could be hypothesized that the thickness of the patina is sufficiently thick that these pixels do not show vibrational modes other than those of sulfur, since the laser does not penetrate to the interior of the pyrite crystal. Finally, in Figure 7.11, black pixels for which the correlation coefficient is between 0.1 and 0.9, spectral information may be the combination of different mineralogical phases, in this case pyrite and elemental sulfur.

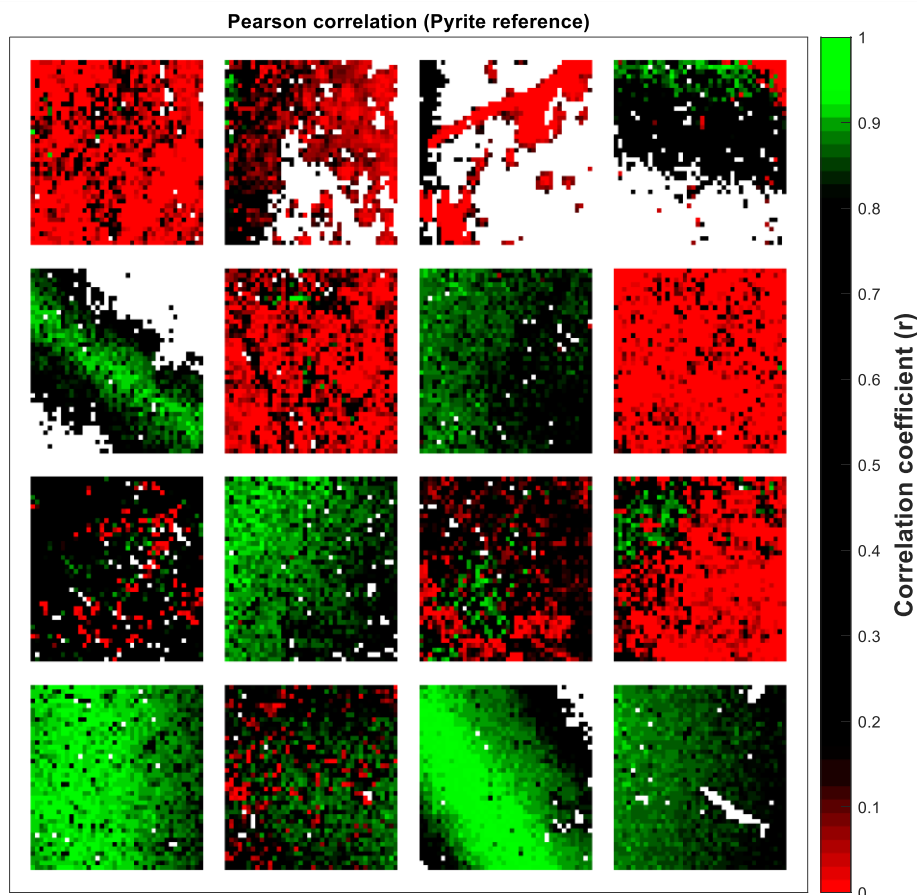


Figure 7.11. Pearson correlation calculated using a pyrite reference spectrum. From left to right and from up to down, samples N1 to N16.

7.4 Conclusions

It can be concluded that the proposed data-driven simulation of OWP in acidic conditions leads to the production of weathering compounds providing interesting results related to the significance of some of the factors analyzed. In addition, the experimental setup followed in the laboratory could help to minimize oxidation times compared to those in nature.

Since the value of DoE for the screening of several factors has been demonstrated, the same procedure could be applied to the study of pyrite under conditions other than extreme acidic environments. In addition, DoE could be applied in a second optimization step, once all the significant factors have been previously identified. This could help to minimize or maximize the amount of elemental sulfur or other weathering products produced, for instance, minimizing the acidification of the environment.

The analysis of the results confirms that Fe^{3+} depletion is the rate-limiting step at low pH waters and not dissolved oxygen, since $\text{S}_2\text{O}_3^{2-}$ preferentially reacts with Fe^{3+} to form SO_4^{2-} (after $\text{S}_4\text{O}_6^{2-}$ decomposition), instead of $\text{S}_2\text{O}_3^{2-}$ disproportionation into sulfur and HSO_3^- . The elemental sulfur produced in this pathway is homogeneously distributed, forming patches of at least $600 \mu\text{m}^2$. In the future, more knowledge could be added to the study of OWP mechanisms by including analytical methods for iron speciation, i.e., to analyze the $\text{Fe}^{2+}/\text{Fe}^{3+}$ ratio throughout the experiments. Microbially induced pyrite oxidation and crystal morphology should be also considered in the future.

Chapter: Case study: sedimentary pyrite in river sands of Taiwan

8

” *The sediments are a sort of epic poem of the earth.*

— Rachel Carson

Taiwan is a complex and dynamic environment. Its geological environment is strongly modulated by the interaction of tectonic plates, which makes this country very rich in a multitude of different landscapes. The island is located at the convergence of the Philippine Sea plate to the southeast, which is being subducted by the Eurasian plate to the northwest. This plate collision has been occurring for the past million years and continues to shape the dramatic topography of the island today. The central mountain range is probably the foremost geological setting. This range runs through the island from north to south and it is composed of metamorphic rocks, mainly gneiss and schist. Moreover, this island is one of the most seismically active regions of the Earth, with frequent earthquakes every year, some of them of catastrophic consequences. The northern part of the island contains dormant volcanoes which show signs of geothermal activity. As if this were not enough, there are also periods of the year influenced by continuous rainfall, and from summer to fall, it is also affected by typhoons. Some of these extreme events can lead to floods, because of the accumulation of rainfall within a short period of time, with dire consequences for the geography of the island. Furthermore, tectonic uplift and erosive forces modulated by the ocean are the cause of Taiwan's coastline shape. Their river systems are steep and short, which facilitates a rapid transportation of sediments coming from the mountains to the sea. Therefore, Taiwan is a unique natural laboratory for the geochemical study of minerals and source rocks.

In the present study, we try to provide some insights on the persistence of pyrite in the sedimentary records. These samples have been characterized by different analytical techniques, trying to provide a chemical explanation of the persistence of pyrite, if any.

8.1 Material and instrumentation

8.1.1 Samples

Sand samples were collected at the bars and levees sediments of five rivers located at the south of the island. The geographic distribution and coordinates of the sampling points are reported in Table 8.1 and Figure 8.1, respectively.

Table 8.1. Geographical coordinates expressed in decimal degrees scale.

Sample	River	Site	Date	Latitude (N)	Longitude (E)
S4562	Luye	Luye	4/10/2012	22.8902	121.0946
S4569	Taimali	Taimali	5/10/2012	22.5916	120.9931
S4572	Dazhu	Daxi	5/10/2012	22.4582	120.9395
S4574	Dawu	Dawu	5/10/2012	22.3610	120.9064
S4577	Fenggang	Fenggang	5/10/2012	22.1960	120.6905

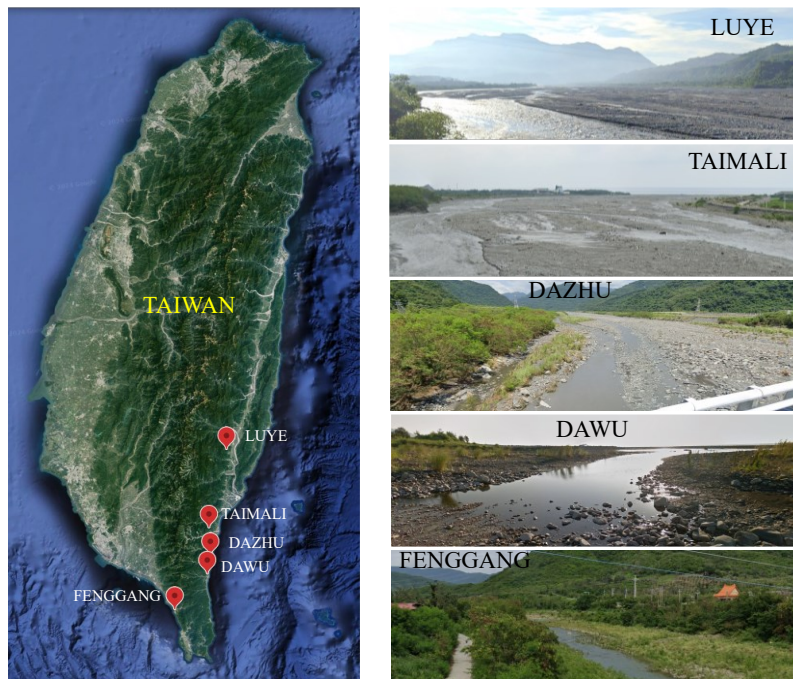


Figure 8.1. Map of Taiwan and images of the sampling points. Images acquired from Google Earth.

The heavy mineral (HM) fraction (<math><500\ \mu\text{m}</math>) was gravimetrically separated following each step of the protocol described in [157]. The samples were embedded in araldite resin and polished until exposure of the grains.

8.1.2 Instrumentation

Polarized Leica DM750 optical microscope equipped with 10 ×, 20 ×, and 63 ×. An external light source was used for the identification of opaque minerals.

The Raman spectrometer used for the acquisition of the spectra has been already described in chapter 5. The acquisition conditions were as follows: 0.1 to 100 % power of the laser, slit opening 65 μm, exposure time 1 to 50 s and number of accumulations from 1 to 10. The spectral range was 145-1912 cm⁻¹. The average spectral resolution was 1.7 cm⁻¹, with a total number of points per spectrum equal to 1015.

Zeiss Gemini 500 Scanning Electron Microscope (SEM) with emission source (FEG) equipped with Bruker QUANTAX integrated energy dispersive (EDS) microanalysis system. The microscope operated with acceleration voltages of 0.5-30 kV, beam currents of 3 pA-20 nA, and a nominal resolution of 0.6 nm at 15 kV. In addition to the common “in-camera” detectors for secondary electrons (SE) and backscattered electrons (BSE), the instrument is equipped with “in-lens” detectors (BSE/SE) for high-resolution imaging.

8.1.3 Software

MATLAB R2022b (*MathWorks, Massachusetts, USA*) was used for dataset preparation and the use of a toolbox for PCA analysis [158]. ESPRIT software (Bruker) was used for the visualization and analysis of EDS spectra and images.

8.2 Results

8.2.1 Optical microscope

Polarized optical microscopes are useful when dealing with transparent minerals. However, opaque minerals such as pyrite are difficult to identify with transmitted light. In this project, a different approach was instead followed. An external light source was placed orthogonal to the lens of the microscope, manually adjusting the angle with respect to the sample to increase the amount of reflected light and the image quality. Figure 8.2 shows images of the same sample but acquired in transmitted light and in reflected light mode.

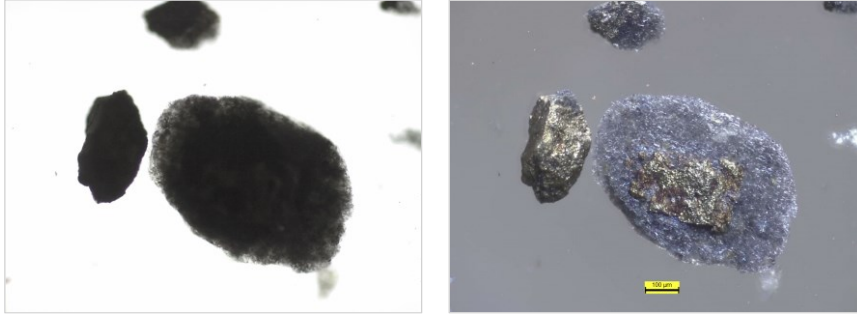


Figure 8.2. Pyrite crystal in rock fragment under transmitted light (left) and reflected light (right).

Therefore, the HM fraction of the five samples collected was analyzed in reflected light. Among the five samples, pyrite was not found in the sample collected in Dawu river. Figure 8.3 shows some of the pyrite fragments identified.



Figure 8.3. From left to the right, pyrite fragments identified in Taimali, Dazhu and Fenggang rivers, respectively.

Some of the pyrite fragments from Taimali and Dazhu are found as inclusions of rock fragments. In the case of Dazhu, cubic morphology seems to be predominant, showing also features of oxidation regarding the reddish patina covering the fragments. Conversely, some of the pyrite fragments found in Fenggang are not rock fragments, although oxidation features are also evident.

Among the different samples analyzed, the one from Luye seems to be a very special case. This HM fraction is full of unweathered and slightly to severely weathered pyrite fragments. Figure 8.4 shows just some of the many identified pyrite fragments.

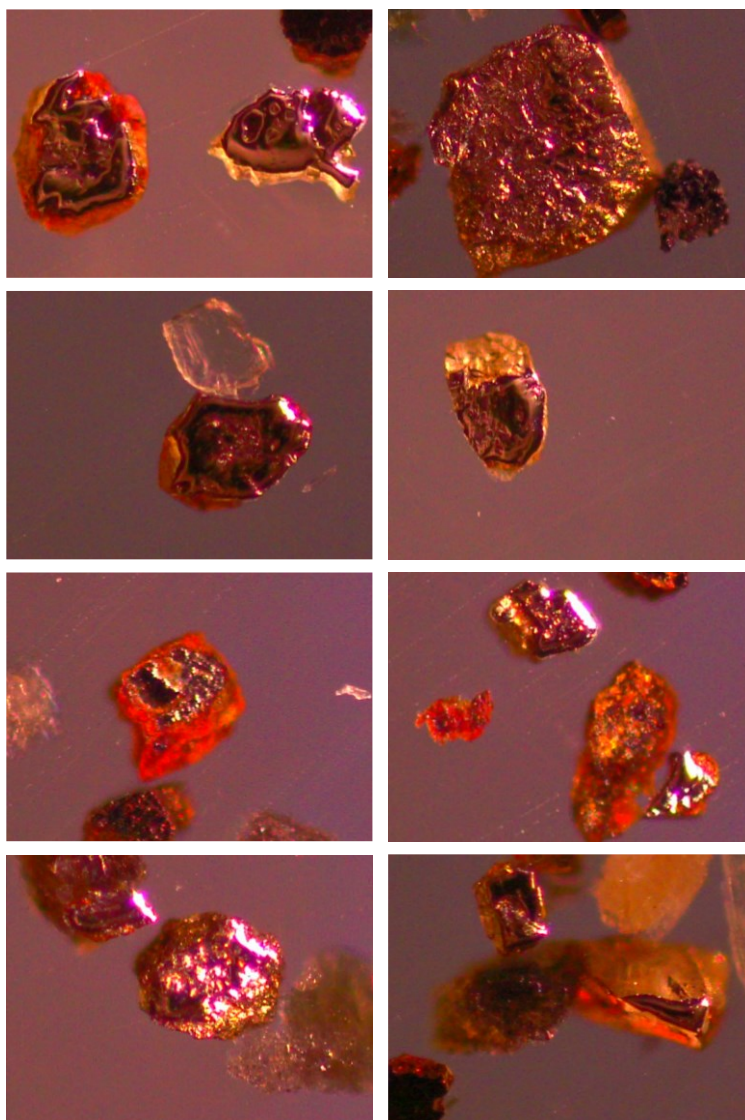


Figure 8.4. Pyrite fragments identified in the sample collected in Luye river.

8.2.2 Raman spectroscopy

To confirm the identity of the pyrite fragments found at Luye by visual evaluation under the optical microscope, single-point Raman analyses were conducted. First, a part of the HM fraction collected was embedded in araldite resin and the surface was polished until exposure of the fragments, as shown in Figure 8.5. Before starting the analysis, the microscope of the Raman spectrometer was used to make a mosaic image representative of the surface. Then, fragments were selected and marked according to the previous information gathered during the analysis with the optical microscope. This image is shown in Figure 8.6.

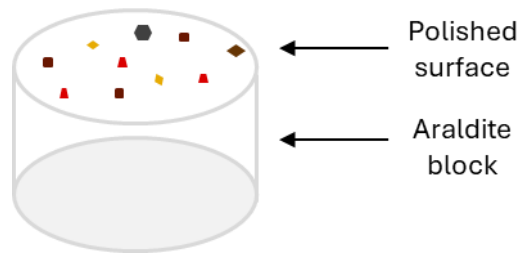


Figure 8.5. Schematic representation on the HM fraction preparation of the sample collected in Luye.

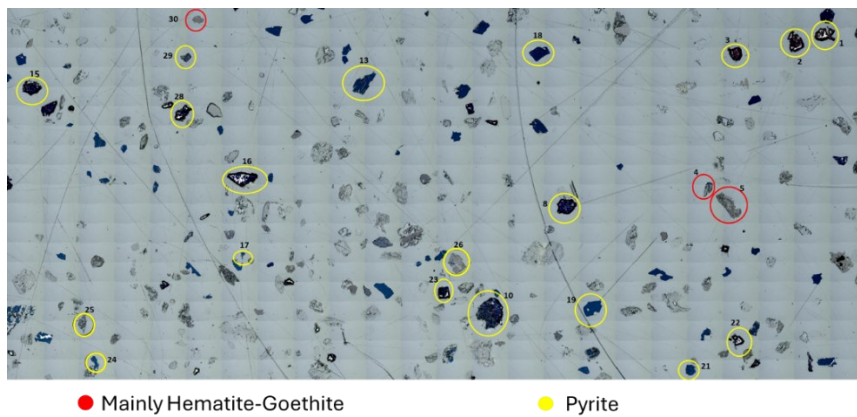


Figure 8.6. Mosaic image of the araldite block acquired with the optical microscope of the Raman spectrometer.

During spot analysis of pyrite fragments, no vibrational modes other than those of the three typical vibrational modes of pyrite were found. However, discrepancies in peak position from one point to another of the same fragments were found in more than half of the samples analyzed. A detailed discussion will be provided in section 8.3.1. Some examples of the Raman spectra acquired are provided in Figure 8.7.

In order to confirm that the discrepancies found are not due to the acquisition parameters, e.g., due to a high laser power that induces mineralogical transformations, several spectra were acquired of the sample and point, changing the power of the laser, the number of accumulations and the exposure time. The surface of the sample was visually evaluated with the microscope after each acquisition, to check for burns marks, making the

sample apparently intact. The results of these experiments are shown in Figure 8.8 and 8.9.

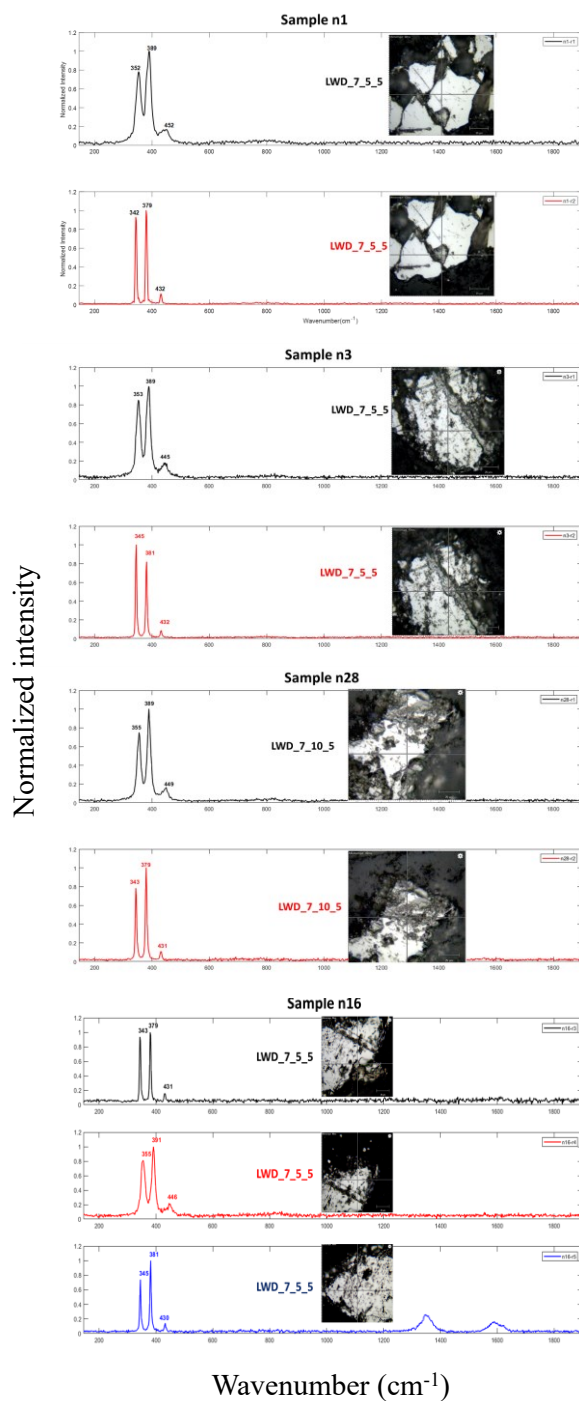


Figure 8.7. Raman spectra acquired from some of the samples analyzed. The objective used was the long working distance (LWD) 50x. The rest of the numbers refer to the exposure time (s), the power of the laser (%) and the number of accumulations, respectively.

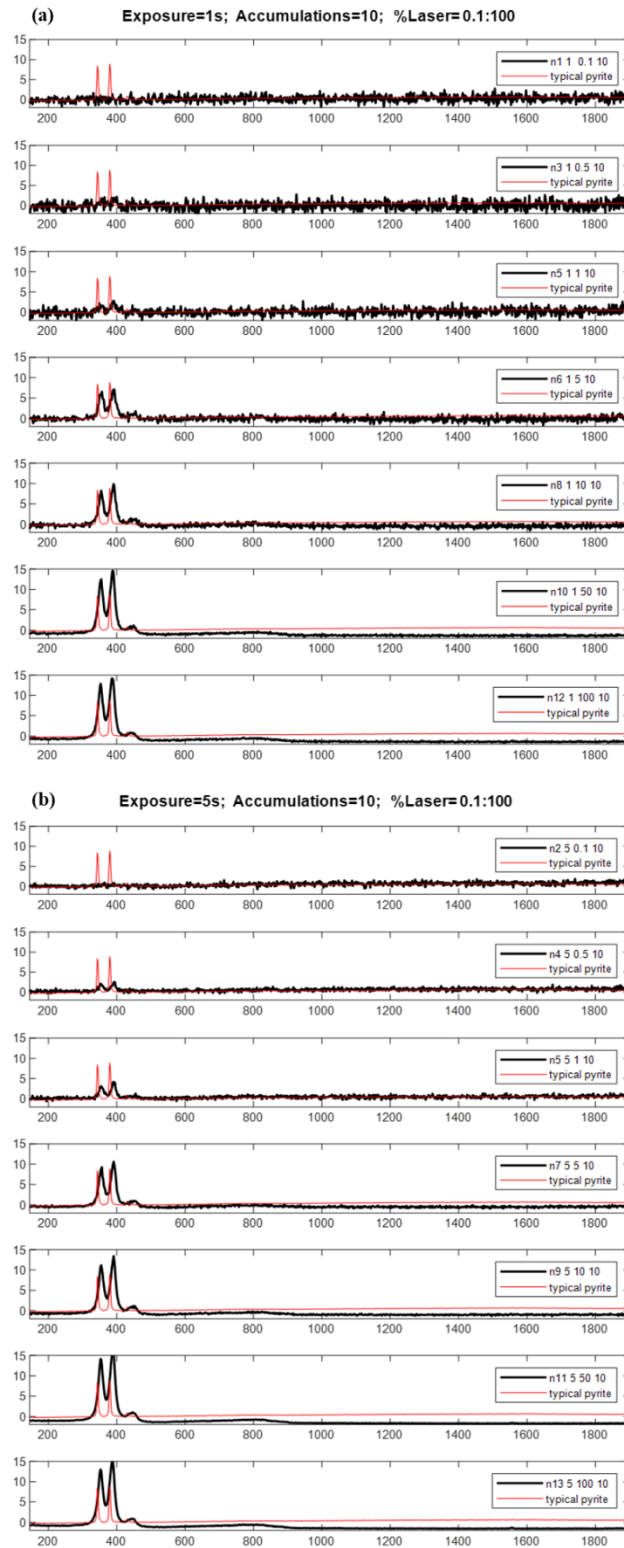


Figure 8.8. (a) Exposure time and number of accumulations equal to 1 s and 10, respectively. (b) Exposure time and number of accumulations equal to 5 s and 10, respectively. In both cases, from the top to the bottom, the power of the laser ranges from 0.1 to 100 %.

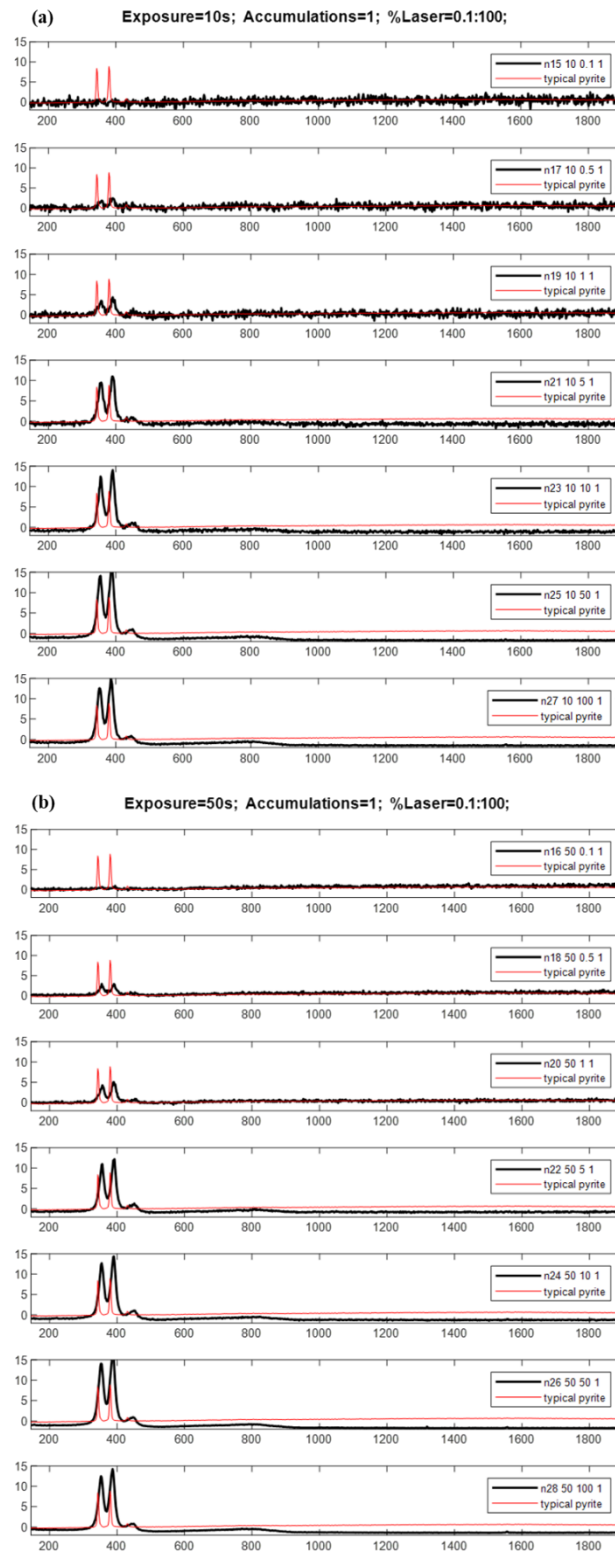


Figure 8.9. (a) Exposure time and number of accumulations equal to 10 s and 1, respectively. (b) Exposure time and number of accumulations equal to 50 s and 1, respectively. In both cases, from the top to the bottom, the power of the laser ranges from 0.1 to 100 %.

8.2.3 Scanning electron microscopy-energy dispersive spectroscopy (SEM-EDS)

The same fragments were subsequently analyzed with SEM-EDS to evaluate the chemical composition of the fragments. Some examples are shown in Figure 8.10.

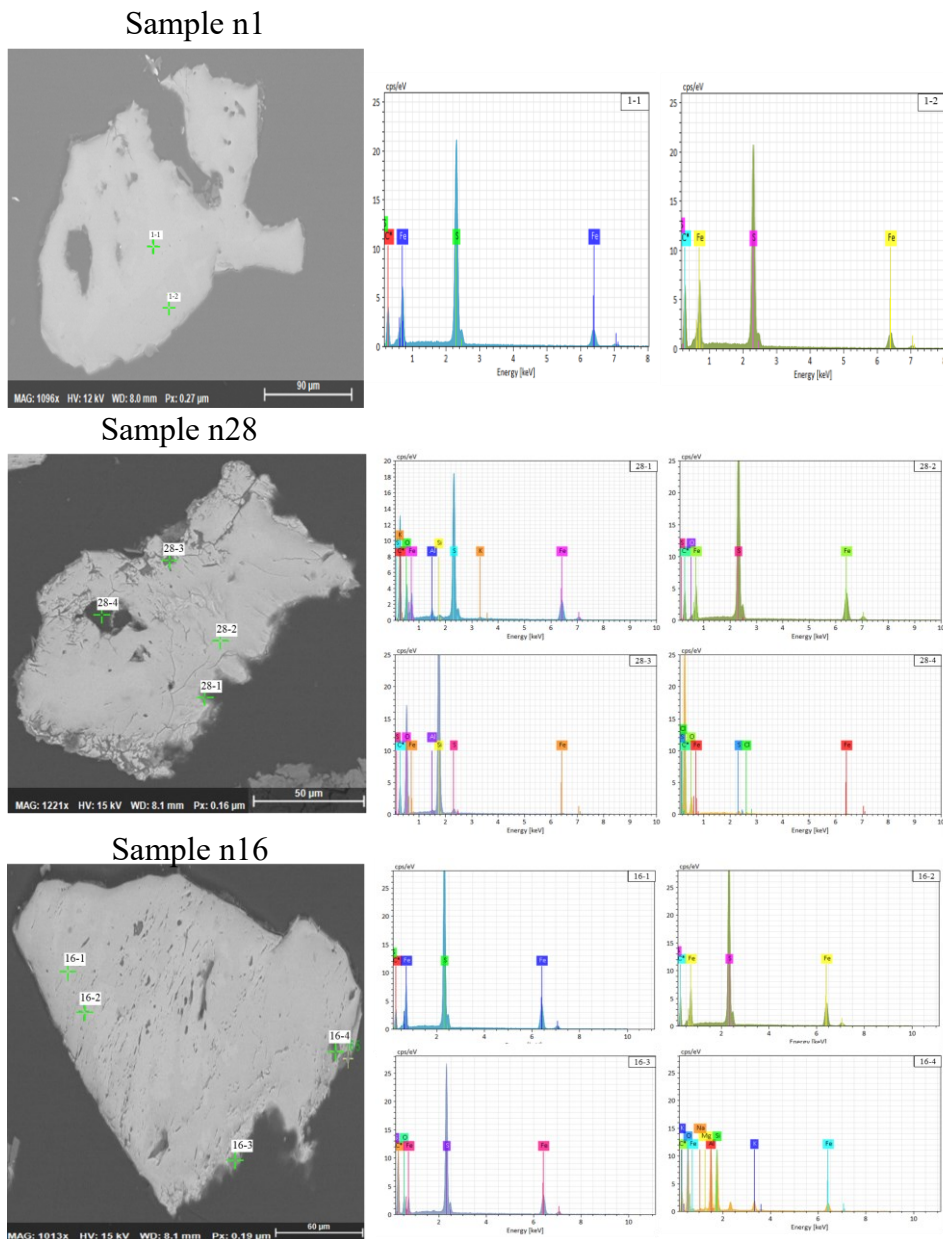


Figure 8.10. EDS analysis of some of the samples whose Raman spectra have been shown above as examples in Section 8.2.2.

In addition to the traditional spot analysis, elemental images were acquired from some of the samples. Figure 8.11 shows an example of one of the samples that has been mapped.

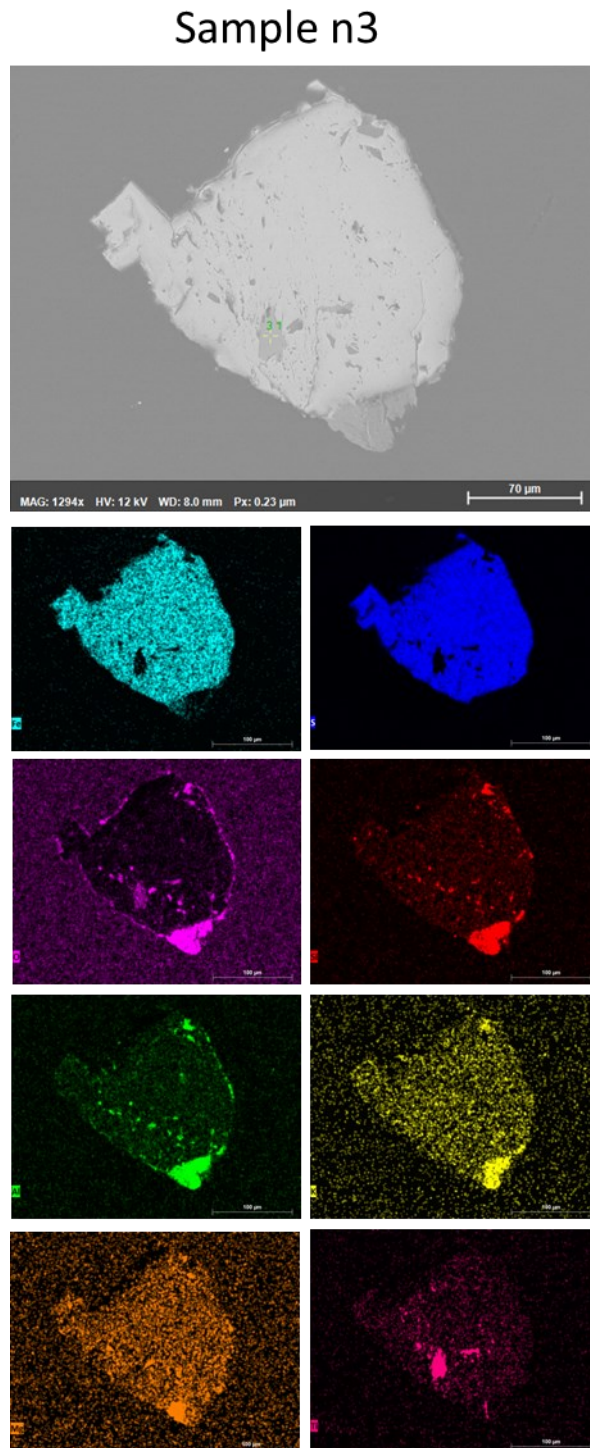


Figure 8.11. Example of EDS images based on the elemental composition of the sample.

8.3 Discussion

8.3.1 Analysis of the samples collected

The entire sedimentary fractions collected in Taiwan were prepared in thin sections and analyzed by the Laboratory for Sediment Provenance Studies (University of Milano Bicocca) following the area method, which combines optical microscope (transmitted light and reflected light) and Raman spectroscopy. However, only values of interest to the ongoing research will be reported in this thesis. On the one hand, the heavy mineral concentration (HMC), which is the percentage of both opaque and transparent heavy minerals in the sedimentary fraction is shown in Table 8.2. This value is characteristic of each sample.

Table 8.2. HMC of the sedimentary samples.

Sample	River	HMC (%)
S4562	Luye	6.10
S4569	Taimali	1.00
S4572	Dazhu	1.00
S4574	Dawu	1.20
S4577	Fenggang	0.77

There is a significant difference in HMC in Luye with respect to the rest of the samples, indicating a different geological environment. On the other hand, the percentages of pyrite in the HM fraction are reported in Table 8.3, making a distinction between the percentage of fresh pyrite, oxidized pyrite and pyrite in rock fragments. As can be seen, in Luye half of the pyrite is fresh and the other half oxidized. The opaque fraction (22%) is dominated by fresh angular pyrite with conchoidal fracture, abundant oxidized corroded pyrite and rusty grains transformed into goethite and lepidocrocite.

Table 8.3. Pyrite percentages found in the HM fraction, expressed as total percentage with respect to all the grains of the sedimentary fraction analyzed.

Location	Fresh Py (%)	Oxidized py (%)	Py in RF (%)
Luye	0.68	0.67	0.00
Taimali	0.00	0.22	0.03
Dazhu	0.01	0.04	0.01
Dawu	0.00	0.00	0.00
Fenggang	0.00	0.03	0.01

This can also be seen in the reflected light images shown in Figure 8.4, where some pyrite fragments are bright and fresh, while many others are covered by the characteristic reddish oxidation patina.

In Taimali, however, no fresh pyrite was found, being all the fragments oxidized or in rock fragments as those shown in Figure 8.3. The opaque fraction (23%) is dominated by weathered grains. Abundant Fe-oxides and hydroxides and common deeply oxidized grains of pyrite (small cubes).

Dazhu and Fenggang present similar percentages. In Dazhu, the opaque fraction (22%) is dominated by deeply weathered grains of orange-yellow goethite. Pyrite is present and rare, and it is always oxidized (corroded grains). In Fenggang, the opaque fraction (9%) is dominated by aggregates of orange-reddish oxidized grains, composed of goethite, very rare lepidocrocite and residual rare fresh pyrite (few micron crystals). Subordinate grains of framboidal pyrite are also present.

In Dawu, no pyrite was found. The opaque fraction (11%) is dominated by weathered grains of orange-yellow goethite. Pyrite is rare and oxidized. Opaque small euhedral crystals are detected (Magnetite).

Therefore, the HMC reported in Table 8.2 seems to be higher in samples with fresh pyrite and rare goethite-lepidocrocite aggregates, while lower in samples with deeply weathered opaque minerals.

As mentioned before, the area method followed was supported by Raman spectroscopy for the confirmation of the minerals. The pyrite from Luye, Taimali and Dazhu do not show discrepancies with respect to the position of the characteristic vibrational modes ($E_g \sim 343 \text{ cm}^{-1}$, $A_g \sim 379 \text{ cm}^{-1}$ and $T_g \sim 430 \text{ cm}^{-1}$). However, some of the framboidal pyrite found in Fenggang (biogenic origin) shows lower frequency modes and a broadening, with a peak position for the E_g and A_g , of ~ 341 and $\sim 376 \text{ cm}^{-1}$, respectively. The broadening of the peaks is justified by the lower crystallinity of biogenic pyrite. In addition, some of the pyrite fragments forming aggregates of small crystals found at Luye, Taimali, Dazhu and Fenggang show typical peaks of carbonaceous material (D-band from 1320 to 1360 cm^{-1} and G-band from 1520 to 1600 cm^{-1}) which provide information on the presence of organic matter on the surface of these aggregates.

The Raman analysis of the araldite blocks prepared from the HM fraction of the sample collected at Luye (section 8.2.2) highlights a peak shifting towards a higher wavenumber with respect to the typical peak position of the three vibrational modes of pyrite, as well as peak broadening. As can be seen in the images provided in Figure 8.7, which represent only a few of the many analyses performed, there are two different situations. On the one hand, the spectra acquired on the parts of the crystal surface that were not well polished and, therefore, completely exposed, show the characteristic peak position of the pyrite vibrational modes. On the other hand, the spectra acquired in areas of the surface that were polished and exposed, show this phenomenon of displacement and broadening of the peaks. Regarding the additional test carried out and reported in Figure 8.8 and Figure 8.9, it can be concluded that the acquisition parameters employed did not induce mineralogical transformation in the surface that could justify this situation. Therefore, two hypotheses are presented. The first hypothesis is that the polishing of the araldite block somehow modifies the acquired vibrational modes, although it is just the exposed zones that show this behavior and not the unpolished zones, as one would think. The second hypothesis is that the crystal structure inside and in the nucleus of the pyrite crystals found in Luye is different from that of other pyrite fragments in the rest of the samples, presenting only the typical vibrational modes on the surface. This could also justify a different provenance of the pyrite in Luye with respect to the rest of the samples, which is ultimately related to the very different geological settings of the island. Unfortunately, during the period of the PhD project, it has not been possible to perform additional experiments to confirm some of these hypotheses, for example with characterization techniques such as X-ray Diffraction (XRD).

Finally, the results obtained by the SEM-EDS analysis confirm that the elemental composition of the pyrite fragments found at Luye does not differ from that of other pyrites, being mainly constituted by Fe and S. Only in some of the fragments were also found other elements such as O, which could be justified by the presence of an oxidation patina, which tends to start on the edges, ridges or defects of the crystals. Thus, from a chemical point of view, it cannot be justified the persistence of fresh pyrite fragments in the sedimentary records of Luye due to the lack of trace elements in the crystalline structure. In this sense, other studies [159] suggest that the

presence of trace elements such as Co and As modifies the electrical properties of pyrite, which ultimately is responsible for the oxidative chemical weathering of this mineral.

However, the analysis of the EDS images acquired from some of the fragments (an example is shown in Figure 8.11) revealed the presence of other elements contained in inclusions, which were not previously noticed by the visual evaluation under the microscope. These elements include Al, Si, K, Mg and Ti. A detailed analysis of these inclusions allowed us to differentiate 6 main types of inclusions (none of them made of Fe or S), whose elemental composition is reported in Table 8.4.

Table 8.4. Elemental composition of the different inclusions found in the analyzed pyrite fragments from Luye. Positive presence is denoted by (+) while negative presence is denoted by (-).

Inclusion	Si	O	Al	Ti	K	Mg
1	+	+	-	-	-	-
2	-	+	-	+	-	-
3	-	+	+	-	-	-
4	-	+	+	-	+	-
5	+	+	+	-	+	-
6	+	+	+	-	-	+

8.3.2 Analysis of geochemical data from the literature

To shed light on the factors that make the sedimentary samples found at Luye different from the others, in particular with respect to the % of fresh and oxidized pyrite found (Table 8.3), it was compiled different data from the literature with respect to the water chemistry of Luye, Taimali, Dazhu, Dawu and Fenggang and some other parameters as the pH, temperature and conductivity [160,161]. In addition, erosion rate data was published in [162,163]. Based on the collected data, additional parameters have been calculated:

$$Erosion\ flux\ \left[\frac{t}{km^2y^1} \right] = 2.5 * measured\ erosion\ rate$$

$$Pyrite\ flux\ \left[\frac{t}{km^2y^1} \right] = Erosion\ flux * \frac{\sum(fresh + oxidized + in\ RF)\%_{py}}{100}$$

All the data collected is shown in Table 8.5. Values reported are the average values of the data found in the literature.

Table 8.5. Water chemistry and erosion rate data collected from the literature, except for % of pyrite values, which have been generated in this study.

	pH	T (°C)	EC ($\mu\text{S}/\text{c}$)	Ba (μM)	Ca (μM)	Fe (μM)	K (μM)	Li (μM)	Mg (μM)	Na (μM)	Si (μM)	Sr (μM)	Cl ⁻ (μM)
Luye	7.8	26.3	631	0	2455.5	0	97.4	14.9	820	1183.4	236.3	7.6	228.1
Taimali	8.1	23.2	476	0	2320.3	0	59	0	135	202.7	144.1	5.2	23.8
Dazhu	8.2	23.5	388	0	1355.6	0	34.5	0	311.8	265.7	173.7	4.4	71.4
Dawu	8.5	25.5	377	0	1188.1	0	38.9	0	363.8	323.9	156.8	1.9	67.8
Fenggang	8.2	25.9	313.2	0.03	831.5	0.2	33	1.4	440.4	851.4	230.8	1.8	250.7

	NO ₃ ⁻ (μM)	SO ₄ ²⁻ (μM)	TDS (μM)	Erosion rate (m/My)	HMC (%)	Fresh Py (%)	Oxidized py (%)	Py in RF (%)	Erosion Flux ($\text{t km}^{-2} \text{y}^{-1}$)	Pyrite Flux ($\text{t km}^{-2} \text{yr}^{-1}$)
	9.6	1494.6	6547.3	3170	6.1	0.7	0.7	0	7925	107.32
	0	1415.3	8076	2220	1	0	0.2	0.03	5550	14.1
	0	779.5	5800.8	1320	1	0	0	0.01	3300	1.85
	0	643.7	5558.8	370	1.2	0	0	0	925	0
	9.6	261.6	5859.2	130	0.8	0	0	0.01	325	0.13

A PCA was performed on the data collected. Scores and loadings for the first four PCs are reported in Figure 8.12.

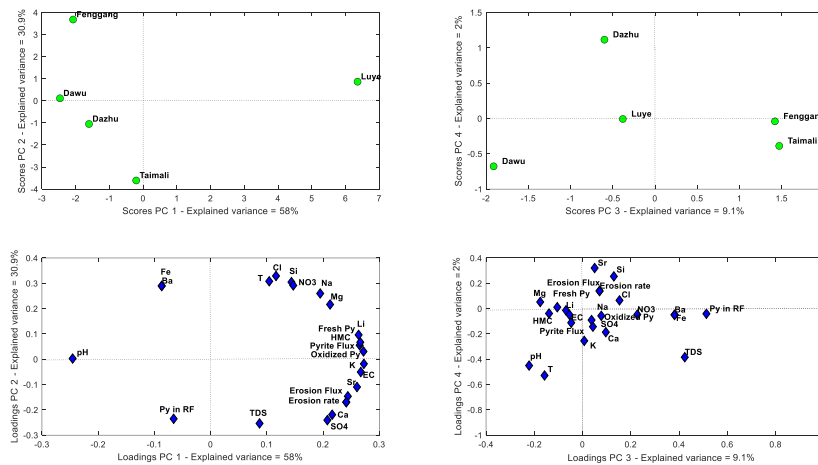


Figure 8.12. Scores (top) and loadings (bottom) of PC1 vs. PC2 (left) and PC3 vs. PC4 (right).

PC1, which explains 58% of the total variance, seems to differentiate between Luye (positive scores) and Dazhu, Dawu and Fenggang samples (negative scores). This separation is mainly due to factors such as pH (negative loadings) and a combination of factors (positive loadings) such as conductivity of the water, pyrite and erosion fluxes, the percentages of fresh and oxidized pyrite and thus, the concentration of heavy minerals in the

sedimentary fraction, and chemical elements present in the water, such as K, Li or Sr. On the contrary, PC2 which explains ~31% of the variance, highlights differences between Taimali (negative scores) and Fenggang (positive scores), mainly due to differences between the percentage of pyrite in rock fragments, the total dissolved solids in water and the concentration of SO_4^{2-} (negative loadings) and the temperature and elements such as Fe, Ba, Cl or Si (positive loadings).

PC3 and PC4, which together explain ~11% of the total variance, seem to explain differences between Taimali, Dazhu, Dawu and Fenggang samples, which indicates that, regarding this data collection, Luye is very different from the rest of the sedimentary locations, as was already suspected.

A better way of visualizing this is to plot the scores of PC1, PC2 and PC3, as shown in Figure 8.13. As can be observed, Taimali, Dazhu, Dawu and Fenggang are clustered almost in the same plane, while Luye in the space of principal components is located far from this imaginary plane.

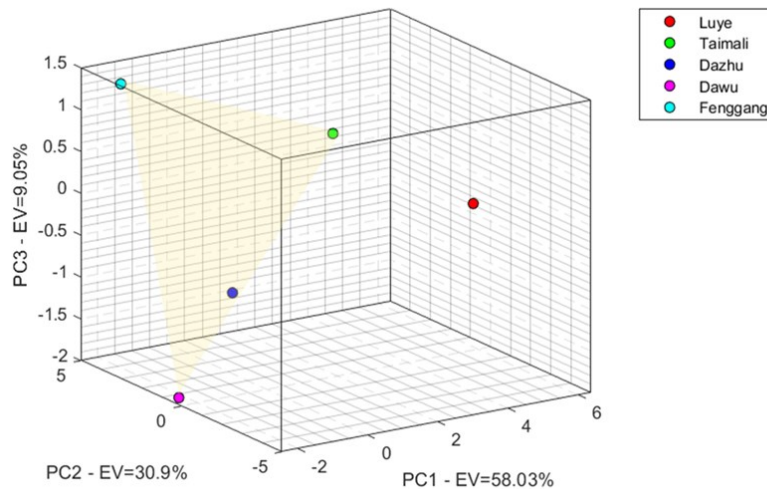


Figure 8.13. Scores of PC1 vs. PC2 vs. PC3.

Moreover, correlations between the total percentage of fresh and oxidized pyrite, the erosion rate, the concentration of sulfates in water (ultimately related to pyrite weathering) and pyrite flux (expressed in logarithmic scale) are reported in Figure 8.14. As can be observed, the total percentage of pyrite appears to follow an increasing trend with the erosion rate from Fenggang to Taimali (from south to north), which can be explained by the fact that, due to the increasing erosion rate, more pyrite fragments are eroded,

transported through the fluvial system and then deposited in the sediments. However, more pyrite available and in contact with water and oxygen means more sulfate ions in solution, leading to the acidification of the waters due to pyrite weathering. Therefore, a similar trend is observed from Fenggang to Taimali but considering the concentration of sulfate. However, in both cases, this trend dramatically changes from Taimali to Luye. The erosion rate in Luye is much higher than in Taimali, although the concentration of sulfate is similar. The total percentage of pyrite at Luye is much higher than at Taimali, as already discussed, which cannot be justified only by south to north trend. Although the number of samples analyzed is not sufficient to propose a solid hypothesis, pyrite found in the HM fraction from Luye must come from a geological setting different from the rest of the samples collected.

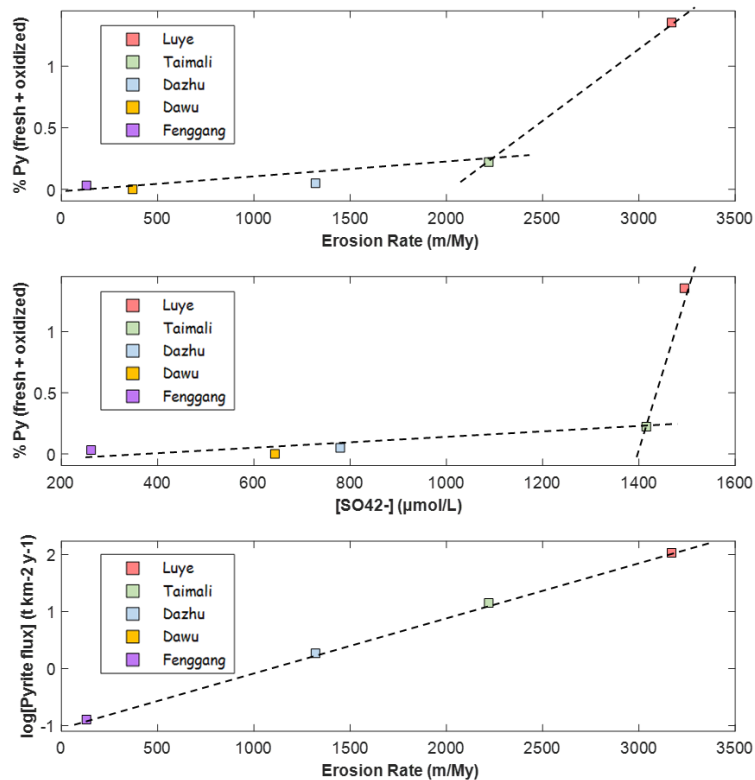


Figure 8.14. Correlation plot between some of the variables.

8.3.3 Geological thoughts on pyrite persistence

Despite no chemical explanation has been found to justify the persistence of pyrite (which was one of the objectives of this thesis), this section will discuss some possible factors that may help unravel the persistence of pyrite in the Luye sedimentary record in future studies from a geological perspective.

Figure 8.15 shows a geological sketch map of Taiwan, where it is possible to differentiate between different source rocks (information taken from the study carried out by A. Resentini et al. [164]). As can be observed, Fenggang, Dawu and Dazhu are mainly characterized by Miocene (slate belt), whereas Taimali also by Eocene. However, Luye's river is the only one that passes through different geological settings characterized by Eocene (Slate belt), Tailuko and Yuli belts (Tananao complex) and Lichi mélange (Coastal range).

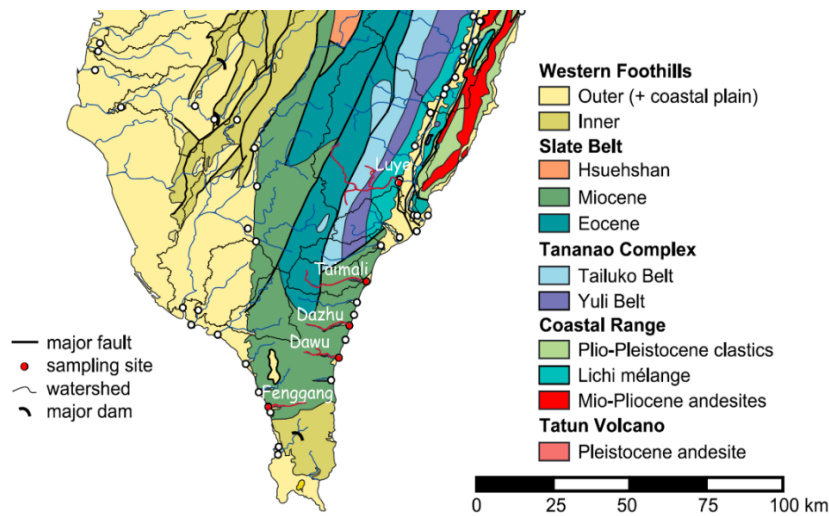


Figure 8.15. Geological map adapted from [164]. Rivers where the sedimentary samples were collected are highlighted in red.

In order to better understand the geological diversity of Taiwan, petrographic and mineralogical parameters of Taiwan river sands data reported by E. Garzanti et al. [165] on 23 samples collected all along the island were explored. The results of the PCA are reported in Figure 8.16.

The calculated scores of the first two PCs are colored according to the provenance, the drainage or the relative geographic position of the samples.

PC1 seems to highlight differences among samples such as those belonging to the Tatun volcano and Luzon arc (positive scores), characterized by heavy minerals, transparent heavy-mineral concentration, plagioclase, orthopyroxene, clinopyroxene, mica and lithic volcanic grains (positive loadings), and those belonging to the Western Foothills, Major western Taiwan rivers, Slate belt and Backbone range (negative scores), characterized by zircon/tourmaline/Ti oxides index (ZTR), apatite and garnet (negative loadings). PC2 mostly differentiates between Tatun volcano and Luzon Arc (negative scores) and Tailuko and Yuli belt (positive scores), characterized by epidote, medium/high-rank felsic metamorphic lithic grains, metavolcanic and metabasite lithic grains, carbonate lithic grains and amphibole.

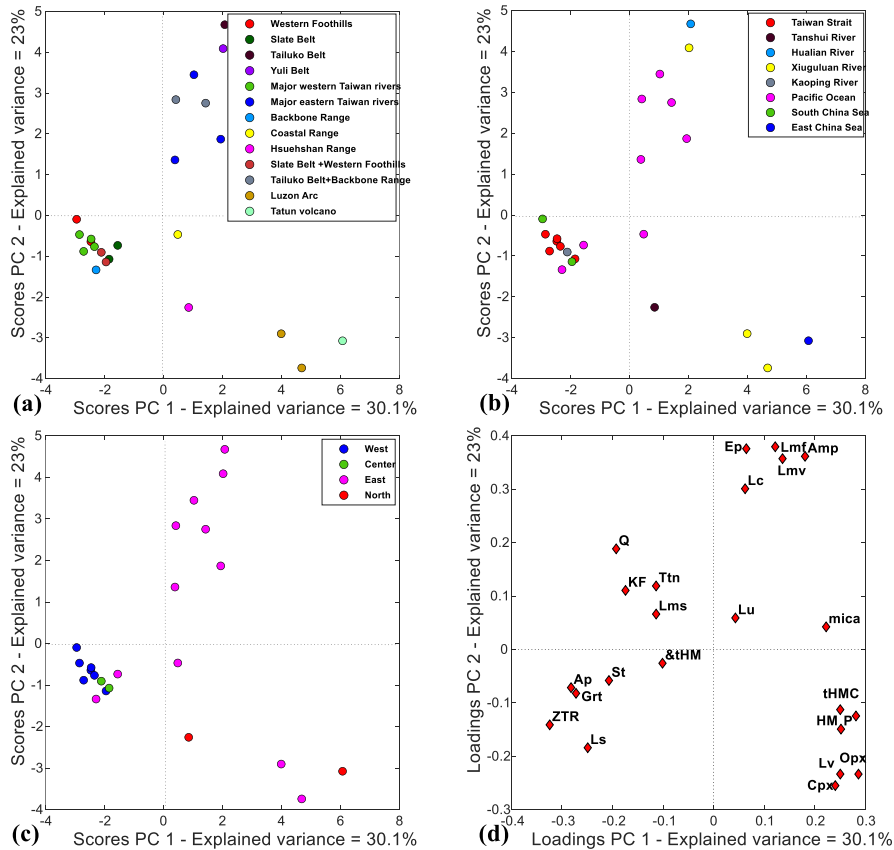


Figure 8.16. PCA of the petrographic and mineralogical data reported in [165]. The scores of the first two PCs are reported, being each sample colored according to their provenance (a), to their drainage (b) or to their relative geographic position (c). Common loadings for PC1 and PC2 are shown in (d).

When samples are colored according to the drainage, different insights can be extracted. All samples belonging to the Taiwan strait and South China Sea classes seem to be clustered and thus characterized by similar variables (negative loadings in PC1). However, the samples belonging to the Pacific Ocean class do not seem to be closely related to each other, which could be explained because this class alone is not enough to explain the petrographic and mineralogical parameters of the samples, and thus source rocks must be also taken into account. A similar situation is found if samples are colored according to their relative geographic position. River sand samples collected at the west of Taiwan are more clustered than those collected at the east of the island, which makes sense, considering that the west is geologically characterized basically by Western Foothills, while the eastern part of the island is much more geologically diverse.

Furthermore, during a qualitative evaluation under the optical microscope in reflected light of some additional samples collected in Taiwan and provided by the Laboratory for Sediment Provenance Studies, pyrite was found. In particular, in sedimentary sand samples collected at Jialu and Luping rivers (Yuli Belt and coastal Eocene), pyrite is rare and mostly oxidized, but rich in rock fragments, meaning that although pyrite was significant in the source rocks, single grains have been mostly dissolved. In samples collected at Beinan river (which has the very same provenance as Luye), fresh pyrite is very abundant, being contained in the Backbone Range and Tananao Schists, although oxidized pyrite is also found weathered. Despite all these similarities with Luye, no framboidal pyrite grains were found at Beinan, whereas some framboidal grains of biogenic origin were found at Luye (although very residual in comparison with other morphologies).

Finally, additional considerations should also be made regarding extreme events affecting the island. Typhoons are very frequent and devastating phenomena, capable of exposing a huge number of sediments and debris, causing floods and dramatically changing the topography of the island. Just to cite some of the most famous, Morakot typhoon (2009), which is considered as the deadliest typhoon to impact Taiwan in recorded history, the very recent Doksuri and Gaemi typhoons (2023 and 2024, respectively) or the Tembin (2012), which affected the southeast of the island a couple of

months before the sampling campaign of the samples analyzed in this project began.

8.4 Conclusions

Evaluation of opaque minerals under the microscope in reflected light mode is a powerful technique for the identification of pyrite with different morphologies and degrees of oxidation, if combined with Raman spectroscopy. Regarding the peak shifting and broadening found in some of the polished pyrite fragments, additional XRD analyses are necessary to support or refute the hypothesis of pyrite from Luye presenting a particular crystalline structure.

The data derived from the SEM-EDS analysis carried out reveals that the chemical composition of the pyrite fragments is the same as other pyrite fragments, without having noticed the presence of trace elements on the crystalline structure. However, different inclusions, not previously noticed by optical microscopic analysis, have been revealed.

In the future, it could be interesting to assess the speciation of Fe and S in these pyrite fragments found in Luye, for example by X-ray photoelectron spectroscopy (XPS). The presence of different weathering products not detected by Raman spectroscopy could justify the passivation of the surface-solution interface against external oxidants, or at least provide information on different oxidation pathways with respect to the pyrite fragments found in other points of the island.

Besides these additional analyses, in future studies, pyrite persistence in the sedimentary records should be evaluated taking into consideration geological aspects such as the different provenance of the samples collected, the rapid erosion rate in the northeast part of the island and the extreme events which can alter for instance, the water chemistry of the different fluvial systems. The combination of all these different factors could lead to a rapid exposure of pyrite fragments, followed by transportation through the fluvial system, deposition and burial of the sediments, making dissolved oxygen less available to act as oxidant. Finally, efforts should also be made to evaluate the kinetics of oxidative weathering in this natural context.

Concluding remarks and future perspectives

This dissertation, part of the Chemical curriculum, focuses on the application of analytical techniques to study OWP. The data generated was supported by various chemometric methods used for characterizing weathered samples, assessing the factors that influence pyrite oxidation in specific environments, and examining a case study where pyrite's persistence was found to be anomalous.

Raman spectroscopy was employed to identify minerals and weathering compounds and to characterize samples. As the first activity, it was developed a personal Raman library incorporating pyrite samples from various locations along with other related minerals. This library, presented in Chapter 5, was crucial to the thesis, as acquisition parameters were carefully selected and controlled to prevent mineralogical transformations, ensuring replicability and consistent comparison of spectra acquired on different days but under the same calibration protocol. The library includes a diverse collection of spectra representing different morphologies of the same minerals, including in some cases vibrational modes relative to the presence of different alteration products, which helps identify similar patterns of chemical weathering among samples from different locations. Additionally, a graphical user interface was developed in MATLAB for managing and creating Raman libraries, allowing for both data visualization and processing. This software is user-friendly, and its code could be modified for educational purposes, potentially becoming a standalone tool that requires no programming skills to operate.

Weathered pyrite spectra are often challenging to analyze due to the presence of various alteration products. Single-point analysis may not always provide a comprehensive understanding of the surface's chemical diversity. Modern Raman instruments offer surface mapping capabilities, but output images are typically based on the intensity of certain peak positions. Moreover, commercial software often lacks advanced data analysis features. In contrast, HSI analysis provides a multivariate framework, utilizing all spectral information from each pixel. Chapter 6 demonstrated the importance of data processing in achieving meaningful results. Preliminary data exploration was crucial for identifying different information sources, especially in heterogeneous samples. Data can be split into distinct datasets for independent analysis, depending on the objectives. This study also introduced a method to resolve spectral overlaps, isolating pure spectra components from a sample. As a result, this methodology enables the generation of compositional images based on comprehensive spectral data and accurate chemical information.

Chemometrics also offers tools for smarter experimental design, maximizing the information extracted. Chapter 7 applied DoE to identify significant factors in pyrite oxidation under acidic conditions. Various analytical techniques, including ICP OES, IC, and HPLC, were employed. Three factors were found to be statistically significant, supporting mechanistic theories on pyrite oxidation pathways. Hyperspectral Raman

imaging was also used to examine how elemental sulfur, a surface weathering product generated during the experiments, is distributed. This study highlights the potential of DoE in geochemical research, as it is increasingly used in various scientific fields and widely applied in industries for process optimization and product manufacturing.

In Chapter 8, pyrite persistence in sand samples from Taiwan was examined from an analytical chemistry perspective. Taiwan is one of the most geologically diverse regions globally. Surprisingly, some pyrite fragments found in the HM fraction of sand samples collected in 2012 were completely fresh and unoxidized. SEM-EDS analysis was conducted to assess the chemical composition of these fragments, but no specific characteristics, such as trace elements linked to pyrite preservation, were found. However, some fragments contained inclusions, which could potentially be used to trace the source rocks. Discrepancies between the shape and peak positions of pyrite's three vibrational modes were observed during Raman analysis of the internal and external regions of the fragments, leading to two proposed hypotheses. Therefore, in relation to the analytical techniques that were possible to apply in the thesis, no clear chemical explanation for pyrite persistence in the sedimentary record was identified. However, geochemical data already published in the literature were analyzed from a multivariate perspective to search for correlations that may help experts better understand pyrite persistence in this context. The chapter also includes a few reflections on Taiwan's geological diversity, erosion trends, fluvial systems, and extreme events that impact the island.

In summary, this thesis presents a novel data-driven approach to the characterization of weathered samples and contributes to understanding the complex oxidation mechanisms of pyrite, which involve multiple pathways, alteration products, and chemical variables.

Future research could apply the proposed HSI methodology to other minerals, demonstrating the potential of Raman spectroscopy beyond single-point analysis or mapping based on peak intensity. The successful DoE approach used in this thesis for extreme acidic conditions could also be applied to other environmental contexts, such as circumneutral water. This information could be relevant for the mining industry, as well as for environmental conservation and for a better understanding of long-term climate change. Additionally, the case study findings could serve as a basis for future interdisciplinary studies.

References

- [1] V.D. Bowles JFW, Howie RA, Rock-Forming Minerals. 5A. Non-Silicates: Oxides, Hydroxides, and Sulphides (2nd edition), Can. Mineral. 49 (2011) 1335–1336. <https://doi.org/10.3749/canmin.49.5.1335>.
- [2] D.J. Vaughan, C.L. Corkhill, Mineralogy of Sulfides, Elements. 13 (2017) 81–87. <https://doi.org/10.2113/gselements.13.2.81>.
- [3] D.J. Vaughan, Sulfide Mineralogy and Geochemistry: Introduction and Overview, Rev. Mineral. Geochemistry. 61 (2006) 1–5. <https://doi.org/10.2138/rmg.2006.61.1>.
- [4] D.J. Vaughan, C.L. Corkhill, Mineralogy of sulfides, Elements. 13 (2017) 81–87. <https://doi.org/10.2113/gselements.13.2.81>.
- [5] R. Jameson, Manual of mineralogy, Wiley, 2011. <https://doi.org/10.5962/bhl.title.49995>.
- [6] A.G.B. H.-R. Wenk, Minerals: their constitution and origin, 2004. <https://doi.org/10.5860/choice.42-2243>.
- [7] R.A. Berner, Models for carbon and sulfur cycles and atmospheric oxygen: application to Paleozoic geologic history., Am. J. Sci. 287 (1987) 177–196. <https://doi.org/10.2475/ajs.287.3.177>.
- [8] R.A. Berner, Phanerozoic atmospheric oxygen: new results using the geocarbsulf model, Am. J. Sci. 309 (2009) 603–606. <https://doi.org/10.2475/07.2009.03>.
- [9] A. Bufe, N. Hovius, R. Emberson, J.K.C. Rugenstein, A. Galy, H.J. Hassenruck-Gudipati, J.M. Chang, Co-variation of silicate, carbonate and sulfide weathering drives CO₂ release with erosion, Nat. Geosci. 14 (2021) 211–216. <https://doi.org/10.1038/s41561-021-00714-3>.
- [10] M.A. Torres, A.J. West, G. Li, Sulphide oxidation and carbonate dissolution as a source of CO₂ over geological timescales, Nature. 507 (2014) 346–349. <https://doi.org/10.1038/nature13030>.
- [11] D. Calmels, J. Gaillardet, A. Brenot, C. France-Lanord, Sustained sulfide oxidation by physical erosion processes in the Mackenzie River basin: Climatic perspectives, Geology. 35 (2007) 1003–1006. <https://doi.org/10.1130/G24132A.1>.
- [12] P.K. Abraitis, R.A.D. Patrick, D.J. Vaughan, Variations in the compositional, textural and electrical properties of natural pyrite: A review, Int. J. Miner. Process. 74 (2004) 41–59. <https://doi.org/10.1016/j.minpro.2003.09.002>.
- [13] D.D. Rimstidt, D.J. Vaughan, Pyrite oxidation: A state-of-the-art assessment of the reaction mechanism, Geochim. Cosmochim. Acta. 67 (2003) 873–880. [https://doi.org/10.1016/S0016-7037\(02\)01165-1](https://doi.org/10.1016/S0016-7037(02)01165-1).
- [14] J.B. Murowchick, H.L. Barnes, Marcasite precipitation from hydrothermal solutions, Geochim. Cosmochim. Acta. 50 (1986) 2615–2629. [https://doi.org/10.1016/0016-7037\(86\)90214-0](https://doi.org/10.1016/0016-7037(86)90214-0).

- [15] M.A.A. Schoonen, H.L. Barnes, Reactions forming pyrite and marcasite from solution: II. Via FeS precursors below 100°C, *Geochim. Cosmochim. Acta.* 55 (1991) 1505–1514. [https://doi.org/10.1016/0016-7037\(91\)90123-M](https://doi.org/10.1016/0016-7037(91)90123-M).
- [16] M.A. Schoonen, H. Barnes, Mechanisms of pyrite and marcasite formation from solution: III. Hydrothermal processes, *Geochim. Cosmochim. Acta.* 55 (1991) 3491–3504. [https://doi.org/10.1016/0016-7037\(91\)90050-F](https://doi.org/10.1016/0016-7037(91)90050-F).
- [17] B.R. Frost, C.D. Frost, *An Introduction to Igneous and Metamorphic Petrology*, 2008.
- [18] J.R. Craig, F.M. Vokes, The metamorphism of pyrite and pyritic ores: an overview, *Mineral. Mag.* 57 (1993) 3–18. <https://doi.org/10.1180/minmag.1993.057.386.02>.
- [19] B.W.D. Yardley, J.S. Cleverley, The role of metamorphic fluids in the formation of ore deposits, *Geol. Soc. London, Spec. Publ.* 393 (2015) 117–134. <https://doi.org/10.1144/SP393.5>.
- [20] J.W. Hedenquist, J.B. Lowenstern, The role of magmas in the formation of hydrothermal ore deposits, *Nature.* 370 (1994) 519–527. <https://doi.org/10.1038/370519a0>.
- [21] A. Martin-Izard, D. Arias, M. Arias, P. Gumiel, D.J. Sanderson, C. Castañón, J. Sanchez, Ore deposit types and tectonic evolution of the Iberian Pyrite Belt: From transtensional basins and magmatism to transpression and inversion tectonics, *Ore Geol. Rev.* 79 (2016) 254–267. <https://doi.org/10.1016/j.oregeorev.2016.05.011>.
- [22] R.R. Seal, Sulfur isotope geochemistry of sulfide minerals, *Rev. Mineral. Geochemistry.* 61 (2006) 633–677. <https://doi.org/10.2138/rmg.2006.61.12>.
- [23] R.A. Berner, Sedimentary pyrite formation: An update, *Geochim. Cosmochim. Acta.* 48 (1984) 605–615. [https://doi.org/10.1016/0016-7037\(84\)90089-9](https://doi.org/10.1016/0016-7037(84)90089-9).
- [24] D. Rickard, G.W. Luther, Chemistry of Iron Sulfides, *Chem. Rev.* 107 (2007) 514–562. <https://doi.org/10.1021/cr0503658>.
- [25] Z. Zhang, C. Zhang, Y. Yang, Z. Zhang, Y. Tang, P. Su, Z. Lin, A review of sulfate-reducing bacteria: Metabolism, influencing factors and application in wastewater treatment, *J. Clean. Prod.* 376 (2022) 134109. <https://doi.org/10.1016/j.jclepro.2022.134109>.
- [26] D. Rickard, M. Musmann, J.A. Steadman, Sedimentary Sulfides, *Elements.* 13 (2017) 117–122. <https://doi.org/10.2113/gselements.13.2.117>.
- [27] R. Raiswell, D.E. Canfield, Sources of iron for pyrite formation in marine sediments, *Am. J. Sci.* 298 (1998) 219–245. <https://doi.org/10.2475/ajs.298.3.219>.
- [28] C.S. Cronan, Mineral Weathering, in: 2018: pp. 87–100. https://doi.org/10.1007/978-3-319-66444-6_7.

- [29] A. Courtin-Nomade, C. Grosbois, M.A. Marcus, S.C. Fakra, J.M. Beny, A.L. Foster, The weathering of a sulfide orebody: Speciation and fate of some potential contaminants, *Can. Mineral.* 47 (2009) 493–508. <https://doi.org/10.3749/canmin.47.3.493>.
- [30] R.A. Berner, Weathering, plants, and the long-term carbon cycle, *Geochim. Cosmochim. Acta.* 56 (1992) 3225–3231. [https://doi.org/10.1016/0016-7037\(92\)90300-8](https://doi.org/10.1016/0016-7037(92)90300-8).
- [31] J.C.. Walker, Global geochemical cycles of carbon, sulfur and oxygen, *Mar. Geol.* 70 (1986) 159–174. [https://doi.org/10.1016/0025-3227\(86\)90093-9](https://doi.org/10.1016/0025-3227(86)90093-9).
- [32] J. Spence, K. Telmer, The role of sulfur in chemical weathering and atmospheric CO₂ fluxes: Evidence from major ions, $\delta^{13}\text{CDIC}$, and $\delta^{34}\text{SSO}_4$ in rivers of the Canadian Cordillera, *Geochim. Cosmochim. Acta.* 69 (2005) 5441–5458. <https://doi.org/10.1016/j.gca.2005.07.011>.
- [33] M.A. Torres, A.J. West, G. Li, Sulphide oxidation and carbonate dissolution as a source of CO₂ over geological timescales, *Nature.* 507 (2014) 346–349. <https://doi.org/10.1038/nature13030>.
- [34] A.N. Buckley, R. Woods, The surface oxidation of pyrite, *Appl. Surf. Sci.* 27 (1987) 437–452. [https://doi.org/10.1016/0169-4332\(87\)90153-X](https://doi.org/10.1016/0169-4332(87)90153-X).
- [35] P.K. Abraitis, R.A.D. Patrick, D.J. Vaughan, Variations in the compositional, textural and electrical properties of natural pyrite: a review, *Int. J. Miner. Process.* 74 (2004) 41–59. <https://doi.org/10.1016/j.minpro.2003.09.002>.
- [36] M.A. Williamson, J.D. Rimstidt, The kinetics and electrochemical rate-determining step of aqueous pyrite oxidation, *Geochim. Cosmochim. Acta.* 58 (1994) 5443–5454. [https://doi.org/10.1016/0016-7037\(94\)90241-0](https://doi.org/10.1016/0016-7037(94)90241-0).
- [37] V.P. (Bill) Evangelou, *Pyrite Oxidation and Its Control*, CRC Press, 2018. <https://doi.org/10.1201/9780203741641>.
- [38] B.. Giannetti, S.. Bonilla, C.. Zinola, T. Rabóczkay, A study of the main oxidation products of natural pyrite by voltammetric and photoelectrochemical responses, *Hydrometallurgy.* 60 (2001) 41–53. [https://doi.org/10.1016/S0304-386X\(00\)00158-4](https://doi.org/10.1016/S0304-386X(00)00158-4).
- [39] M.A. McKibben, H.L. Barnes, Oxidation of pyrite in low temperature acidic solutions: Rate laws and surface textures, *Geochim. Cosmochim. Acta.* 50 (1986) 1509–1520. [https://doi.org/10.1016/0016-7037\(86\)90325-X](https://doi.org/10.1016/0016-7037(86)90325-X).
- [40] K. Sasaki, M. Tsunekawa, T. Ohtsuka, H. Konno, Reply to the Comment by G. W. Luther III on “Confirmation of a sulfur-rich layer on pyrite after oxidative dissolution by Fe(III) ions around pH 2,” *Geochim. Cosmochim. Acta.* 61 (1997) 3273–3274. [https://doi.org/10.1016/S0016-7037\(97\)00145-2](https://doi.org/10.1016/S0016-7037(97)00145-2).
- [41] J.A. Leiro, S.S. Mattila, K. Laajalehto, XPS study of the sulphur 2p spectra of pyrite, *Surf. Sci.* 547 (2003) 157–161. <https://doi.org/10.1016/j.susc.2003.09.033>.
- [42] A.G. Schaufuß, H.W. Nesbitt, I. Kartio, K. Laajalehto, G.M. Bancroft, R. Szargan, Reactivity of surface chemical states on fractured pyrite, *Surf. Sci.*

- 411 (1998) 321–328. [https://doi.org/10.1016/S0039-6028\(98\)00355-0](https://doi.org/10.1016/S0039-6028(98)00355-0).
- [43] J.K. Jerz, J.D. Rimstidt, Pyrite oxidation in moist air, *Geochim. Cosmochim. Acta.* 68 (2004) 701–714. [https://doi.org/10.1016/S0016-7037\(03\)00499-X](https://doi.org/10.1016/S0016-7037(03)00499-X).
- [44] R.T. Lowson, Aqueous oxidation of pyrite by molecular oxygen, *Chem. Rev.* 82 (1982) 461–497. <https://doi.org/10.1021/cr00051a001>.
- [45] R. V. Nicholson, R.. Gillham, E.. Reardon, Pyrite oxidation in carbonate-buffered solution: 2. Rate control by oxide coatings, *Geochim. Cosmochim. Acta.* 54 (1990) 395–402. [https://doi.org/10.1016/0016-7037\(90\)90328-I](https://doi.org/10.1016/0016-7037(90)90328-I).
- [46] C.O. Moses, D. Kirk Nordstrom, J.S. Herman, A.L. Mills, Aqueous pyrite oxidation by dissolved oxygen and by ferric iron, *Geochim. Cosmochim. Acta.* 51 (1987) 1561–1571. [https://doi.org/10.1016/0016-7037\(87\)90337-1](https://doi.org/10.1016/0016-7037(87)90337-1).
- [47] W. Zhu, J.R. Reinfelder, The Microbial Community of a Black Shale Pyrite Biofilm and its Implications for Pyrite Weathering, *Geomicrobiol. J.* 29 (2012) 186–193. <https://doi.org/10.1080/01490451.2010.539663>.
- [48] E.. Todd, D.. Sherman, J.. Purton, Surface oxidation of pyrite under ambient atmospheric and aqueous (pH = 2 to 10) conditions: electronic structure and mineralogy from X-ray absorption spectroscopy, *Geochim. Cosmochim. Acta.* 67 (2003) 881–893. [https://doi.org/10.1016/S0016-7037\(02\)00957-2](https://doi.org/10.1016/S0016-7037(02)00957-2).
- [49] D.M.C. Huminicki, J.D. Rimstidt, Iron oxyhydroxide coating of pyrite for acid mine drainage control, *Appl. Geochemistry.* 24 (2009) 1626–1634. <https://doi.org/10.1016/j.apgeochem.2009.04.032>.
- [50] R.L. McCreery, *Raman Spectroscopy for Chemical Analysis*, Wiley, 2000. <https://doi.org/10.1002/0471721646>.
- [51] E. Smith, G. Dent, *Modern Raman Spectroscopy – A Practical Approach*, Wiley, 2004. <https://doi.org/10.1002/0470011831>.
- [52] W. Guozhen, *Raman spectroscopy: An intensity approach*, 2017.
- [53] S.N. White, Laser Raman spectroscopy as a technique for identification of seafloor hydrothermal and cold seep minerals, *Chem. Geol.* 259 (2009) 240–252. <https://doi.org/10.1016/j.chemgeo.2008.11.008>.
- [54] J.R. Mycroft, G.M. Bancroft, N.S. McIntyre, J.W. Lorimer, I.R. Hill, Detection of sulphur and polysulphides on electrochemically oxidized pyrite surfaces by X-ray photoelectron spectroscopy and Raman spectroscopy, *J. Electroanal. Chem. Interfacial Electrochem.* 292 (1990) 139–152. [https://doi.org/10.1016/0022-0728\(90\)87332-E](https://doi.org/10.1016/0022-0728(90)87332-E).
- [55] M.M. McGuire, K.J. Edwards, J.F. Banfield, R.J. Hamers, Kinetics, surface chemistry, and structural evolution of microbially mediated sulfide mineral dissolution, *Geochim. Cosmochim. Acta.* 65 (2001) 1243–1258. [https://doi.org/10.1016/S0016-7037\(00\)00601-3](https://doi.org/10.1016/S0016-7037(00)00601-3).
- [56] K. Sasaki, M. Tsunekawa, T. Ohtsuka, H. Konno, Confirmation of a sulfur-

- rich layer on pyrite after oxidative dissolution by Fe(III) ions around pH2, *Geochim. Cosmochim. Acta.* 59 (1995) 3155–3158. [https://doi.org/10.1016/0016-7037\(95\)00203-C](https://doi.org/10.1016/0016-7037(95)00203-C).
- [57] D. Susac, L. Zhu, M. Teo, A. Sode, K.C. Wong, P.C. Wong, R.R. Parsons, D. Bizzotto, K.A.R. Mitchell, S.A. Campbell, Characterization of FeS₂-Based Thin Films as Model Catalysts for the Oxygen Reduction Reaction, *J. Phys. Chem. C.* 111 (2007) 18715–18723. <https://doi.org/10.1021/jp073395i>.
- [58] V. Toniazzo, C. Mustin, J. Portal, B. Humbert, R. Benoit, R. Erre, Elemental sulfur at the pyrite surfaces: speciation and quantification, *Appl. Surf. Sci.* 143 (1999) 229–237. [https://doi.org/10.1016/S0169-4332\(98\)00918-0](https://doi.org/10.1016/S0169-4332(98)00918-0).
- [59] M. Cabán-Acevedo, D. Liang, K.S. Chew, J.P. DeGrave, N.S. Kaiser, S. Jin, Synthesis, Characterization, and Variable Range Hopping Transport of Pyrite (FeS₂) Nanorods, Nanobelts, and Nanoplates, *ACS Nano.* 7 (2013) 1731–1739. <https://doi.org/10.1021/nn305833u>.
- [60] J.M. Amigo, *Hyperspectral imaging*, Elsevier, 2019.
- [61] H. Govil, G. Mishra, N. Gill, A. Taloor, P. Diwan, Mapping Hydrothermally Altered Minerals and Gossans using Hyperspectral data in Eastern Kumaon Himalaya, India, *Appl. Comput. Geosci.* 9 (2021) 100054. <https://doi.org/10.1016/j.acags.2021.100054>.
- [62] G. FERRIER, G. WADGE, The application of imaging spectrometry data to mapping alteration zones associated with gold mineralization in southern Spain, *Int. J. Remote Sens.* 17 (1996) 331–350. <https://doi.org/10.1080/01431169608949009>.
- [63] M.M. McGuire, K.N. Jallad, D. Ben-Amotz, R.J. Hamers, Chemical mapping of elemental sulfur on pyrite and arsenopyrite surfaces using near-infrared Raman imaging microscopy, *Appl. Surf. Sci.* 178 (2001) 105–115. [https://doi.org/10.1016/S0169-4332\(01\)00303-8](https://doi.org/10.1016/S0169-4332(01)00303-8).
- [64] M.M. McGuire, R.J. Hamers, Extraction and Quantitative Analysis of Elemental Sulfur from Sulfide Mineral Surfaces by High-Performance Liquid Chromatography, *Environ. Sci. Technol.* 34 (2000) 4651–4655. <https://doi.org/10.1021/es0011663>.
- [65] S.R.C. Douglas A. Skoog, F. James Holler, *Principles of Instrumental Analysis*, 7th ed., 2017.
- [66] Z. Xu, Y. Li, P. Zhou, X. Song, Y. Wang, New insights on simultaneous nitrate and phosphorus removal in pyrite-involved mixotrophic denitrification biofilter for a long-term operation: Performance change and its underlying mechanism, *Sci. Total Environ.* 845 (2022) 157403. <https://doi.org/10.1016/j.scitotenv.2022.157403>.
- [67] C.B. Tabelin, R.D. Corpuz, T. Igarashi, M. Villacorte-Tabelin, R.D. Alorro, K. Yoo, S. Raval, M. Ito, N. Hiroyoshi, Acid mine drainage formation and arsenic mobility under strongly acidic conditions: Importance of soluble phases, iron oxyhydroxides/oxides and nature of oxidation layer on pyrite, *J. Hazard. Mater.* 399 (2020) 122844. <https://doi.org/10.1016/j.jhazmat.2020.122844>.

- [68] C.M.N.L. Cutruneo, M.L.S. Oliveira, C.R. Ward, J.C. Hower, I.A.S. de Brum, C.H. Sampaio, R.M. Kautzmann, S.R. Taffarel, E.C. Teixeira, L.F.O. Silva, A mineralogical and geochemical study of three Brazilian coal cleaning rejects: Demonstration of electron beam applications, *Int. J. Coal Geol.* 130 (2014) 33–52. <https://doi.org/10.1016/j.coal.2014.05.009>.
- [69] B. Polit, P. Mączyński, M. Bosiak, Catch me if you can: Identifying pyrite residues on flint strike-a-lights with the use of SEM-EDS analysis on the example of ancient materials from the northern coast of the Black Sea, *J. Archaeol. Sci. Reports.* 50 (2023) 104064. <https://doi.org/10.1016/j.jasrep.2023.104064>.
- [70] G. Ye, Y. Miao, D. Liu, G. Zhang, Investigation into the impact of High-Altitude conditions on the characteristics and flotation performance of pyrite grinding products, *Miner. Eng.* 209 (2024) 108629. <https://doi.org/10.1016/j.mineng.2024.108629>.
- [71] O.N. Filimonova, I.I. Snigireva, P. Thompson, D. Wermeille, Incorporation of palladium into pyrite: Insights from X-ray absorption spectroscopy analysis and modelling, *Sci. Total Environ.* 920 (2024) 170927. <https://doi.org/10.1016/j.scitotenv.2024.170927>.
- [72] W. Jin, M. Kang, Y. Kang, J. She, D. Qin, H. Wu, K. Wu, C. Chen, H. Liu, Kinetics study on the temperature-dependent reduction of aqueous U(VI) by natural pyrite, *Geochim. Cosmochim. Acta.* 380 (2024) 18–30. <https://doi.org/10.1016/j.gca.2024.07.006>.
- [73] A.O.W. Leung, N.S. Duzgoren-Aydin, K.C. Cheung, M.H. Wong, Heavy Metals Concentrations of Surface Dust from e-Waste Recycling and Its Human Health Implications in Southeast China, *Environ. Sci. Technol.* 42 (2008) 2674–2680. <https://doi.org/10.1021/es071873x>.
- [74] L. Zhao, S. Zhong, K. Fang, Z. Qian, J. Chen, Determination of cadmium(II), cobalt(II), nickel(II), lead(II), zinc(II), and copper(II) in water samples using dual-cloud point extraction and inductively coupled plasma emission spectrometry, *J. Hazard. Mater.* 239–240 (2012) 206–212. <https://doi.org/10.1016/j.jhazmat.2012.08.066>.
- [75] D. Demirezen, K. Uruç, Comparative study of trace elements in certain fish, meat and meat products, *Meat Sci.* 74 (2006) 255–260. <https://doi.org/10.1016/j.meatsci.2006.03.012>.
- [76] M.L. González-Miret, A. Terrab, D. Hernanz, M.Á. Fernández-Recamales, F.J. Heredia, Multivariate Correlation between Color and Mineral Composition of Honeys and by Their Botanical Origin, *J. Agric. Food Chem.* 53 (2005) 2574–2580. <https://doi.org/10.1021/jf048207p>.
- [77] M.R. Gomez, S. Cerutti, L.L. Sombra, M.F. Silva, L.D. Martínez, Determination of heavy metals for the quality control in argentinian herbal medicines by ETAAS and ICP-OES, *Food Chem. Toxicol.* 45 (2007) 1060–1064. <https://doi.org/10.1016/j.fct.2006.12.013>.
- [78] P.C. Naha, P. Chhour, D.P. Cormode, Systematic in vitro toxicological screening of gold nanoparticles designed for nanomedicine applications, *Toxicol. Vitro.* 29 (2015) 1445–1453.

<https://doi.org/10.1016/j.tiv.2015.05.022>.

- [79] H. Li, H. Ji, Chemical speciation, vertical profile and human health risk assessment of heavy metals in soils from coal-mine brownfield, Beijing, China, *J. Geochemical Explor.* 183 (2017) 22–32. <https://doi.org/10.1016/j.gexplo.2017.09.012>.
- [80] J. Wang, G. Liu, L. Lu, J. Zhang, H. Liu, Geochemical normalization and assessment of heavy metals (Cu, Pb, Zn, and Ni) in sediments from the Huaihe River, Anhui, China, *CATENA*. 129 (2015) 30–38. <https://doi.org/10.1016/j.catena.2015.02.008>.
- [81] *Principles and Practice of Modern Chromatographic Methods*, Elsevier, 2022. <https://doi.org/10.1016/c2019-0-03803-4>.
- [82] P.K. Abraitis, R.A. D. Patrick, G.H. Kelsall, D.J. Vaughan, Acid leaching and dissolution of major sulphide ore minerals: processes and galvanic effects in complex systems, *Mineral. Mag.* 68 (2004) 343–351. <https://doi.org/10.1180/0026461046820191>.
- [83] Y. Xu, M.A.A. Schoonen, D.K. Nordstrom, K.M. Cunningham, J.W. Ball, Sulfur geochemistry of hydrothermal waters in Yellowstone National Park, Wyoming, USA. II. Formation and decomposition of thiosulfate and polythionate in Cinder Pool, *J. Volcanol. Geotherm. Res.* 97 (2000) 407–423. [https://doi.org/10.1016/S0377-0273\(99\)00173-0](https://doi.org/10.1016/S0377-0273(99)00173-0).
- [84] K. Fukushi, M. Sasaki, T. Sato, N. Yanase, H. Amano, H. Ikeda, A natural attenuation of arsenic in drainage from an abandoned arsenic mine dump, *Appl. Geochemistry.* 18 (2003) 1267–1278. [https://doi.org/10.1016/S0883-2927\(03\)00011-8](https://doi.org/10.1016/S0883-2927(03)00011-8).
- [85] M.C. Jung, Heavy metal contamination of soils and waters in and around the Imcheon Au–Ag mine, Korea, *Appl. Geochemistry.* 16 (2001) 1369–1375. [https://doi.org/10.1016/S0883-2927\(01\)00040-3](https://doi.org/10.1016/S0883-2927(01)00040-3).
- [86] P. Steinmann, W. Shotyk, Chemical composition, pH, and redox state of sulfur and iron in complete vertical porewater profiles from two Sphagnum peat bogs, Jura Mountains, Switzerland, *Geochim. Cosmochim. Acta.* 61 (1997) 1143–1163. [https://doi.org/10.1016/S0016-7037\(96\)00401-2](https://doi.org/10.1016/S0016-7037(96)00401-2).
- [87] Y. Xu, M.A.. Schoonen, D.. Nordstrom, K.. Cunningham, J.. Ball, Sulfur geochemistry of hydrothermal waters in Yellowstone National Park: I. the origin of thiosulfate in hot spring waters, *Geochim. Cosmochim. Acta.* 62 (1998) 3729–3743. [https://doi.org/10.1016/S0016-7037\(98\)00269-5](https://doi.org/10.1016/S0016-7037(98)00269-5).
- [88] N. Randazzo, R.W. Hilts, M.C. Holt, C.D.K. Herd, B. Reiz, R.M. Whittal, Detection and quantification of organosulfur species in the Tagish Lake Meteorite by highly sensitive <sc>LC-MS</sc>, *Meteorit. Planet. Sci.* (2024). <https://doi.org/10.1111/maps.14189>.
- [89] W. Wang, J. Sun, C. Dong, B. Lian, Biotite weathering by *Aspergillus niger* and its potential utilisation, *J. Soils Sediments.* 16 (2016) 1901–1910. <https://doi.org/10.1007/s11368-016-1388-3>.
- [90] A. Sanchini, S. Szidat, W. Tylmann, H. Vogel, A. Wacnik, M. Grosjean, A

Holocene high-resolution record of aquatic productivity, seasonal anoxia and meromixis from varved sediments of Lake Ładzuny, North-Eastern Poland: insight from a novel multi-proxy approach, *J. Quat. Sci.* 35 (2020) 1070–1080. <https://doi.org/10.1002/jqs.3242>.

- [91] K.A. Burns, Evidence for the importance of including hydrocarbon oxidation products in environmental assessment studies, *Mar. Pollut. Bull.* 26 (1993) 77–85. [https://doi.org/10.1016/0025-326X\(93\)90095-2](https://doi.org/10.1016/0025-326X(93)90095-2).
- [92] Z. Martins, B.A. Hofmann, E. Gnos, R.C. Greenwood, A. Verchovsky, I.A. Franchi, A.J.T. Jull, O. Botta, D.P. Glavin, J.P. Dworkin, P. Ehrenfreund, Amino acid composition, petrology, geochemistry, ^{14}C terrestrial age and oxygen isotopes of the Shiřr 033 CR chondrite, *Meteorit. Planet. Sci.* 42 (2007) 1581–1595. <https://doi.org/10.1111/j.1945-5100.2007.tb00592.x>.
- [93] Handbook of Chemometrics and Qualimetrics: Part A, n.d.
- [94] R. Leardi, Experimental design in chemistry: A tutorial, *Anal. Chim. Acta.* 652 (2009) 161–172. <https://doi.org/10.1016/j.aca.2009.06.015>.
- [95] No Title, (n.d.). <https://doi.org/10.1080/10408347.2020.1848517>.
- [96] H. Ebrahimi-Najafabadi, R. Leardi, M. Jalali-Heravi, Experimental Design in Analytical Chemistry—Part I: Theory, *J. AOAC Int.* 97 (2014) 3–11. <https://doi.org/10.5740/jaoacint.SGEEbrahimi1>.
- [97] H. Ebrahimi-Najafabadi, R. Leardi, M. Jalali-Heravi, Experimental Design in Analytical Chemistry—Part II: Applications, *J. AOAC Int.* 97 (2014) 12–18. <https://doi.org/10.5740/jaoacint.SGEEbrahimi2>.
- [98] D.C. Woods, S.M. Lewis, Design of Experiments for Screening, in: *Handb. Uncertain. Quantif.*, Springer International Publishing, Cham, 2017: pp. 1143–1185. https://doi.org/10.1007/978-3-319-12385-1_33.
- [99] R.C. Torrijos, R. Phan-Tan-Luu, Screening Strategies, in: *Compr. Chemom.*, Elsevier, 2020: pp. 209–250. <https://doi.org/10.1016/B978-0-12-409547-2.14755-9>.
- [100] P. Oliveri, C. Malegori, R. Simonetti, M. Casale, The impact of signal pre-processing on the final interpretation of analytical outcomes – A tutorial, *Anal. Chim. Acta.* 1058 (2019) 9–17. <https://doi.org/10.1016/j.aca.2018.10.055>.
- [101] R. Bro, A.K. Smilde, Principal component analysis, *Anal. Methods.* 6 (2014) 2812–2831. <https://doi.org/10.1039/C3AY41907J>.
- [102] A.M. Ikotun, A.E. Ezugwu, L. Abualigah, B. Abuhaija, J. Heming, K-means clustering algorithms: A comprehensive review, variants analysis, and advances in the era of big data, *Inf. Sci. (Ny)*. 622 (2023) 178–210. <https://doi.org/10.1016/j.ins.2022.11.139>.
- [103] A.K. Jain, Data clustering: 50 years beyond K-means, *Pattern Recognit. Lett.* 31 (2010) 651–666. <https://doi.org/10.1016/j.patrec.2009.09.011>.
- [104] J. Benesty, J. Chen, Y. Huang, I. Cohen, Pearson Correlation Coefficient, in: 2009: pp. 1–4. https://doi.org/10.1007/978-3-642-00296-0_5.

- [105] P. Schober, C. Boer, L.A. Schwarte, Correlation Coefficients: Appropriate Use and Interpretation, *Anesth. Analg.* 126 (2018) 1763–1768. <https://doi.org/10.1213/ANE.0000000000002864>.
- [106] A. de Juan, R. Tauler, Multivariate Curve Resolution: 50 years addressing the mixture analysis problem – A review, *Anal. Chim. Acta.* 1145 (2021) 59–78. <https://doi.org/10.1016/j.aca.2020.10.051>.
- [107] A. de Juan, S. Piqueras, M. Maeder, T. Hancewicz, L. Duponchel, R. Tauler, Chemometric Tools for Image Analysis, in: *Infrared Raman Spectrosc. Imaging*, Wiley, 2014: pp. 57–110. <https://doi.org/10.1002/9783527678136.ch2>.
- [108] J.M. Amigo, H. Babamoradi, S. Elcoroaristizabal, Hyperspectral image analysis. A tutorial, *Anal. Chim. Acta.* 896 (2015) 34–51. <https://doi.org/10.1016/j.aca.2015.09.030>.
- [109] J. Jaumot, R. Tauler, MCR-BANDS: A user friendly MATLAB program for the evaluation of rotation ambiguities in Multivariate Curve Resolution, *Chemom. Intell. Lab. Syst.* 103 (2010) 96–107. <https://doi.org/10.1016/j.chemolab.2010.05.020>.
- [110] J. Xia, Y. Yang, H. He, X. Zhao, C. Liang, L. Zheng, C. Ma, Y. Zhao, Z. Nie, G. Qiu, Surface analysis of sulfur speciation on pyrite bioleached by extreme thermophile *Acidianus manzaensis* using Raman and XANES spectroscopy, *Hydrometallurgy.* 100 (2010) 129–135. <https://doi.org/10.1016/j.hydromet.2009.11.001>.
- [111] H. Vogt, T. Chattopadhyay, H.J. Stolz, Complete first-order Raman spectra of the pyrite structure compounds FeS₂, MnS₂ AND SiP₂, *J. Phys. Chem. Solids.* 44 (1983) 869–873. [https://doi.org/10.1016/0022-3697\(83\)90124-5](https://doi.org/10.1016/0022-3697(83)90124-5).
- [112] B. Cavalazzi, R. Barbieri, S.L. Cady, A.D. George, S. Gennaro, F. Westall, A. Lui, R. Canteri, A.P. Rossi, G.G. Ori, K. Taj-Eddine, Iron-framboids in the hydrocarbon-related Middle Devonian Hollard Mound of the Anti-Atlas mountain range in Morocco: Evidence of potential microbial biosignatures, *Sediment. Geol.* 263–264 (2012) 183–193. <https://doi.org/10.1016/j.sedgeo.2011.09.007>.
- [113] T. Borjigin, L. Yin, L. Bian, X. Yuan, C. Zhou, F. Meng, X. Xie, F. Bao, Nano-Scale Spheroids and Fossils from the Ediacaran Doushantuo Formation in China, *Open Paleontol. J.* 5 (2014) 1–9. <https://doi.org/10.2174/1874425701405010001>.
- [114] A.K. Kleppe, A.P. Jephcoat, High-pressure Raman spectroscopic studies of FeS₂ pyrite, *Mineral. Mag.* 68 (2004) 433–441. <https://doi.org/10.1180/0026461046830196>.
- [115] J.A. Tamayo, F.A. Vásquez, F. Bedoya, J.A. Calderón, Oxidation mechanism of pyrite in a thiosulfate solution: electrochemical impedance (EIS) and in situ Raman spectroscopy, *Heliyon.* 9 (2023) e21809. <https://doi.org/10.1016/j.heliyon.2023.e21809>.
- [116] S. Danise, B. Cavalazzi, S. Dominici, F. Westall, S. Monechi, S. Guioli,

Evidence of microbial activity from a shallow water whale fall (Voghera, northern Italy), *Palaeogeogr. Palaeoclimatol. Palaeoecol.* 317–318 (2012) 13–26. <https://doi.org/10.1016/j.palaeo.2011.12.001>.

- [117] Z. Wei, Y. Qiu, H. Chen, K. Yan, Z. Zhu, Q. Kuang, S. Yang, Magnetic-field-assisted aerosol pyrolysis synthesis of iron pyrite sponge-like nanochain networks as cost-efficient counter electrodes in dye-sensitized solar cells, *J. Mater. Chem. A.* 2 (2014) 5508–5515. <https://doi.org/10.1039/C4TA00199K>.
- [118] S. Wang, Y. Wang, M. Li, T. Qi, G. Liu, Q. Zhou, Z. Peng, X. Li, Characteristics of product layer and effects of sulfur-bearing ions on pyrite leaching in sodium aluminate solutions, *Miner. Eng.* 202 (2023) 108295. <https://doi.org/10.1016/j.mineng.2023.108295>.
- [119] T.P. Mernagh, A.G. Trudu, A laser Raman microprobe study of some geologically important sulphide minerals, *Chem. Geol.* 103 (1993) 113–127. [https://doi.org/10.1016/0009-2541\(93\)90295-T](https://doi.org/10.1016/0009-2541(93)90295-T).
- [120] Z. Tu, J. Wan, C. Guo, C. Fan, T. Zhang, G. Lu, J.R. Reinfelder, Z. Dang, Electrochemical oxidation of pyrite in pH 2 electrolyte, *Electrochim. Acta.* 239 (2017) 25–35. <https://doi.org/10.1016/j.electacta.2017.04.049>.
- [121] J. Xu, H. Xue, X. Yang, H. Wei, W. Li, Z. Li, W. Zhang, C. Lee, Synthesis of Honeycomb-like Mesoporous Pyrite FeS₂ Microspheres as Efficient Counter Electrode in Quantum Dots Sensitized Solar Cells, *Small.* 10 (2014) 4754–4759. <https://doi.org/10.1002/sml.201401102>.
- [122] G. Jervis, *I tesori sotterranei dell'Italia*, 1873.
- [123] B. G., *I minerali del piacentino – come riconoscerli dove trovarli*, 2008.
- [124] N. Mobaraki, J.M. Amigo, HYPER-Tools. A graphical user-friendly interface for hyperspectral image analysis, *Chemom. Intell. Lab. Syst.* 172 (2018) 174–187. <https://doi.org/10.1016/j.chemolab.2017.11.003>.
- [125] J. Jaumot, R. Gargallo, A. de Juan, R. Tauler, A graphical user-friendly interface for MCR-ALS: a new tool for multivariate curve resolution in MATLAB, *Chemom. Intell. Lab. Syst.* 76 (2005) 101–110. <https://doi.org/10.1016/j.chemolab.2004.12.007>.
- [126] R. Bro, A.K. Smilde, Principal component analysis, *Anal. Methods.* 6 (2014) 2812–2831. <https://doi.org/10.1039/c3ay41907j>.
- [127] V. Mazet, D. Brie, J. Idier, Baseline spectrum estimation using half-quadratic minimization, *Eur. Signal Process. Conf.* 06-10-Sept (2015) 305–308.
- [128] J. Jaumot, R. Tauler, MCR-BANDS: A user friendly MATLAB program for the evaluation of rotation ambiguities in Multivariate Curve Resolution, *Chemom. Intell. Lab. Syst.* 103 (2010) 96–107. <https://doi.org/10.1016/j.chemolab.2010.05.020>.
- [129] S. Praver, R.J. Nemanich, Raman spectroscopy of diamond and doped diamond, *Philos. Trans. R. Soc. A Math. Phys. Eng. Sci.* 362 (2004) 2537–2565. <https://doi.org/10.1098/rsta.2004.1451>.

- [130] A. Dychalska, P. Popielarski, W. Franków, K. Fabisiak, K. Paprocki, M. Szybowicz, Study of CVD diamond layers with amorphous carbon admixture by Raman scattering spectroscopy, *Mater. Sci. Pol.* 33 (2015) 799–805. <https://doi.org/10.1515/msp-2015-0067>.
- [131] C. Brolly, J. Parnell, S. Bowden, Raman spectroscopy: Caution when interpreting organic carbon from oxidising environments, *Planet. Space Sci.* 121 (2016) 53–59. <https://doi.org/10.1016/j.pss.2015.12.008>.
- [132] V. Consonni, G. Baccolo, F. Gosetti, R. Todeschini, D. Ballabio, A MATLAB toolbox for multivariate regression coupled with variable selection, *Chemom. Intell. Lab. Syst.* 213 (2021) 104313. <https://doi.org/10.1016/j.chemolab.2021.104313>.
- [133] A. Samanta, G.R. Tripathy, R. Das, Temporal Variations in Water Chemistry of the (Lower) Brahmaputra River: Implications to Seasonality in Mineral Weathering, *Geochemistry, Geophys. Geosystems.* 20 (2019) 2769–2785. <https://doi.org/10.1029/2018GC008047>.
- [134] P.C. Kemeny, G.I. Lopez, N.F. Dalleska, M. Torres, A. Burke, M.P. Bhatt, A.J. West, J. Hartmann, J.F. Adkins, Sulfate sulfur isotopes and major ion chemistry reveal that pyrite oxidation counteracts CO₂ drawdown from silicate weathering in the Langtang-Trisuli-Narayani River system, Nepal Himalaya, *Geochim. Cosmochim. Acta.* 294 (2021) 43–69. <https://doi.org/10.1016/j.gca.2020.11.009>.
- [135] T. Tsering, M.S.M. Abdel Wahed, S. Iftekhhar, M. Sillanpää, Major ion chemistry of the Teesta River in Sikkim Himalaya, India: Chemical weathering and assessment of water quality, *J. Hydrol. Reg. Stud.* 24 (2019) 100612. <https://doi.org/10.1016/j.ejrh.2019.100612>.
- [136] I. Cartwright, Concentration vs. streamflow (C-Q) relationships of major ions in south-eastern Australian rivers: Sources and fluxes of inorganic ions and nutrients, *Appl. Geochemistry.* 120 (2020) 104680. <https://doi.org/10.1016/j.apgeochem.2020.104680>.
- [137] V.N. Amrith, K. Arun, D. Nishitha, K. Balakrishna, H.N. Udayashankar, N. Khare, Major ion chemistry and silicate weathering rate of a small Western Ghats river, Sharavati, southwestern India, *Appl. Geochemistry.* 136 (2022) 105182. <https://doi.org/10.1016/j.apgeochem.2021.105182>.
- [138] N. Madhavan, V. Subramanian, Fluoride concentration in river waters of south Asia, *Curr. Sci.* 80 (2001) 1312–1319.
- [139] A.R. Elsetinow, M.J. Borda, M.A.A. Schoonen, D.R. Strongin, Suppression of pyrite oxidation in acidic aqueous environments using lipids having two hydrophobic tails, *Adv. Environ. Res.* 7 (2003) 969–974. [https://doi.org/10.1016/S1093-0191\(02\)00101-6](https://doi.org/10.1016/S1093-0191(02)00101-6).
- [140] B.M.G. Katrina J. Edwards, Geomicrobiology of Pyrite (FeS₂) Dissolution: Case Study at Iron Mountain, California, *Geomicrobiol. J.* 16 (1999) 155–179. <https://doi.org/10.1080/014904599270668>.
- [141] R.G. Brereton, *Chemometrics: Data Analysis for the Laboratory and Chemical Plant*, Wiley, 2003. <https://doi.org/10.1002/0470863242>.

- [142] A. Schippers, T. Rohwerder, W. Sand, Intermediary sulfur compounds in pyrite oxidation: implications for bioleaching and biodepyritization of coal, *Appl. Microbiol. Biotechnol.* 52 (1999) 104–110. <https://doi.org/10.1007/s002530051495>.
- [143] A. Schippers, P. Jozsa, W. Sand, Sulfur chemistry in bacterial leaching of pyrite, *Appl. Environ. Microbiol.* 62 (1996) 3424–3431. <https://doi.org/10.1128/aem.62.9.3424-3431.1996>.
- [144] J.D. Rimstidt, D.J. Vaughan, Pyrite oxidation: a state-of-the-art assessment of the reaction mechanism, *Geochim. Cosmochim. Acta.* 67 (2003) 873–880. [https://doi.org/10.1016/S0016-7037\(02\)01165-1](https://doi.org/10.1016/S0016-7037(02)01165-1).
- [145] M. Descostes, P. Vitorge, C. Beaucaire, Pyrite dissolution in acidic media, *Geochim. Cosmochim. Acta.* 68 (2004) 4559–4569. <https://doi.org/10.1016/j.gca.2004.04.012>.
- [146] G.K. Druschel, R.J. Hamers, J.F. Banfield, Kinetics and mechanism of polythionate oxidation to sulfate at low pH by O₂ and Fe³⁺, *Geochim. Cosmochim. Acta.* 67 (2003) 4457–4469. [https://doi.org/10.1016/S0016-7037\(03\)00388-0](https://doi.org/10.1016/S0016-7037(03)00388-0).
- [147] M.A. Williamson, J.D. Rimstidt, The rate of decomposition of the ferric-thiosulfate complex in acidic aqueous solutions, *Geochim. Cosmochim. Acta.* 57 (1993) 3555–3561. [https://doi.org/10.1016/0016-7037\(93\)90138-M](https://doi.org/10.1016/0016-7037(93)90138-M).
- [148] G.W. Heunisch, Stoichiometry of the reaction of sulfites with hydrogen sulfide ion, *Inorg. Chem.* 16 (1977) 1411–1413. <https://doi.org/10.1021/ic50172a033>.
- [149] P.R. Holmes, F.K. Crundwell, The kinetics of the oxidation of pyrite by ferric ions and dissolved oxygen: an electrochemical study, *Geochim. Cosmochim. Acta.* 64 (2000) 263–274. [https://doi.org/10.1016/S0016-7037\(99\)00296-3](https://doi.org/10.1016/S0016-7037(99)00296-3).
- [150] T. Biegler, D.A. Swift, Anodic behaviour of pyrite in acid solutions, *Electrochim. Acta.* 24 (1979) 415–420. [https://doi.org/10.1016/0013-4686\(79\)87029-2](https://doi.org/10.1016/0013-4686(79)87029-2).
- [151] J.R. Flatt, R. Woods, A voltammetric investigation of the oxidation of pyrite in nitric acid solutions: relation to treatment of refractory gold ores, *J. Appl. Electrochem.* 25 (1995). <https://doi.org/10.1007/BF00233904>.
- [152] S.L. Harmer, H.W. Nesbitt, Stabilization of pyrite (FeS₂), marcasite (FeS₂), arsenopyrite (FeAsS) and loellingite (FeAs₂) surfaces by polymerization and auto-redox reactions, *Surf. Sci.* 564 (2004) 38–52. <https://doi.org/10.1016/j.susc.2004.06.199>.
- [153] G.K. Druschel, R.J. Hamers, G.W. Luther, J.F. Banfield, Kinetics and Mechanism of Trithionate and Tetrathionate Oxidation at Low pH by Hydroxyl Radicals, *Aquat. Geochemistry.* 9 (2003) 145–164. <https://doi.org/10.1023/B:AQUA.0000019495.91752.d7>.
- [154] M.J. Borda, A.R. Elsetinow, M.A. Schoonen, D.R. Strongin, Pyrite-Induced

Hydrogen Peroxide Formation as a Driving Force in the Evolution of Photosynthetic Organisms on an Early Earth, *Astrobiology*. 1 (2001) 283–288. <https://doi.org/10.1089/15311070152757474>.

- [155] M.J. Borda, A.R. Elsetinow, D.R. Strongin, M.A. Schoonen, A mechanism for the production of hydroxyl radical at surface defect sites on pyrite, *Geochim. Cosmochim. Acta*. 67 (2003) 935–939. [https://doi.org/10.1016/S0016-7037\(02\)01222-X](https://doi.org/10.1016/S0016-7037(02)01222-X).
- [156] K. Zheng, H. Li, L. Xu, S. Li, L. Wang, X. Wen, Q. Liu, The influence of humic acids on the weathering of pyrite: Electrochemical mechanism and environmental implications, *Environ. Pollut.* 251 (2019) 738–745. <https://doi.org/10.1016/j.envpol.2019.05.060>.
- [157] S. Andò, Gravimetric Separation of Heavy Minerals in Sediments and Rocks, *Minerals*. 10 (2020) 273. <https://doi.org/10.3390/min10030273>.
- [158] D. Ballabio, A MATLAB toolbox for Principal Component Analysis and unsupervised exploration of data structure, *Chemom. Intell. Lab. Syst.* 149 (2015) 1–9. <https://doi.org/10.1016/j.chemolab.2015.10.003>.
- [159] K.S. Savage, D. Stefan, S.W. Lehner, Impurities and heterogeneity in pyrite: Influences on electrical properties and oxidation products, *Appl. Geochemistry*. 23 (2008) 103–120. <https://doi.org/10.1016/j.apgeochem.2007.10.010>.
- [160] J.-M. Bufe, Aaron; Hovius, Niels; Emberson, Robert; Rugenstein, Jeremy K. C.; Galy, Albert; Hassenruck-Gudipati, Hima J.; Chang, Major element stream water chemistry, compiled 10Be erosion rates, and analyses of weathering across an erosion-rate gradient in in southern Taiwan, (2021). <https://doi.org/10.5880/GFZ.4.6.2021.001>.
- [161] A. Bufe, N. Hovius, R. Emberson, J.K.C. Rugenstein, A. Galy, H.J. Hassenruck-Gudipati, J.-M. Chang, Co-variation of silicate, carbonate and sulfide weathering drives CO₂ release with erosion, *Nat. Geosci.* 14 (2021) 211–216. <https://doi.org/10.1038/s41561-021-00714-3>.
- [162] M.G. Fellin, C.-Y. Chen, S.D. Willett, M. Christl, Y.-G. Chen, Erosion rates across space and timescales from a multi-proxy study of rivers of eastern Taiwan, *Glob. Planet. Change*. 157 (2017) 174–193. <https://doi.org/10.1016/j.gloplacha.2017.07.012>.
- [163] C. Chen, S.D. Willett, A.J. West, S. Dadson, N. Hovius, M. Christl, J.B.H. Shyu, The impact of storm-triggered landslides on sediment dynamics and catchment-wide denudation rates in the southern Central Range of Taiwan following the extreme rainfall event of Typhoon Morakot, *Earth Surf. Process. Landforms*. 45 (2020) 548–564. <https://doi.org/10.1002/esp.4753>.
- [164] A. Resentini, L. Goren, S. Castelltort, E. Garzanti, Partitioning sediment flux by provenance and tracing erosion patterns in Taiwan, *J. Geophys. Res. Earth Surf.* 122 (2017) 1430–1454. <https://doi.org/10.1002/2016JF004026>.
- [165] E. Garzanti, A. Resentini, Provenance control on chemical indices of weathering (Taiwan river sands), *Sediment. Geol.* 336 (2016) 81–95.

<https://doi.org/10.1016/j.sedgeo.2015.06.013>.

Publications during the PhD course

- [1] Termopoli, V.; Piergiovanni, M.; Ballabio, D.; Consonni, V.; **Cruz Muñoz, E.**; Gosetti, F., “Condensed Phase Membrane Introduction Mass Spectrometry: A Direct Alternative to Fully Exploit the Mass Spectrometry Potential in Environmental Sample Analysis”. *Separations* 2023, 10, doi:10.3390/separations10020139.
- [2] **Muñoz, E.C.**; Gosetti, F.; Ballabio, D.; Andò, S.; Gómez-Laserna, O.; Amigo, J.M.; Garzanti, E., “Characterization of Pyrite Weathering Products by Raman Hyperspectral Imaging and Chemometrics Techniques”. *Microchem. J.* 2023, 190, 108655, doi:10.1016/j.microc.2023.108655.
- [3] **Cruz Muñoz, E.**; Termopoli, V.; Orlandi, M.; Gosetti, F., “Non-Targeted Identification of Tianeptine Photodegradation Products in Water Samples by UHPLC-QTOF MS/MS”. *Chemosphere* 2024, 361, 142534, doi:10.1016/j.chemosphere.2024.142534.
- [4] **Cruz Muñoz, E.**; Gosetti, F.; Andò, S.; Ballabio, D.; Garzanti, E. “Oxidative Weathering of Pyrite in Acidic Environments: Data-Driven Experimental Evaluation Coupled with Raman Hyperspectral Imaging”. *Sci. Total Environ.* 2024, 954, 176284, doi:10.1016/j.scitotenv.2024.176284.
- [5] **Cruz Muñoz, E.**; Tseberlidis, G.; Hasan Husien, A.; Binetti, S.; Gosetti, F.; “Photolytic and photocatalytic degradation of diclofenac. Identification of the transformation products by non-target UHPLC-MS/MS approach”. *Springer*; (**under revision**).
- [6] Fernández-Ramos, M.D.; Malaespina, R.; López-Aveiga M.G.; **Cruz Muñoz, E.**; Medina-Castillo, A.L.; “Chapter 16. Data Analysis for microfluidic-based analytical devices (μ FADs)” Chapter in book “Problem-Oriented Analytical Chemistry Driven by Chemometrics”, *Elsevier S&T Books*, (**under revision**).

Congresses and courses attended

- Incontri Gruppo Interdivisionale di Scienza delle separazioni GISS 2024, Bari, Italy (Oral communication)
- 16th International GEORAMAN conference, Rhodes, Greece (Oral communication)
- SCI 2024- XXVIII Congresso nazionale della Società Chimica Italiana, Milan (Poster)
- Multivariate Curve Resolution (MCR) course, Ravenna, Italy
- Workshop di Chemiometria 2024, Ravenna, Italy (Oral communication)
- XXVIII School of Mass spectrometry, Siena, Italy
- XXX Congresso Divisione di Chimica Analitica, Vasto, Italy (Oral communication and poster)
- XI Colloquium Chemometricum Mediterraneum, Padova, Italy, (Oral communication)
- International School of Chemometrics 2023.- DATA FUSION, University of Copenhagen, Denmark
- International School of Chemometrics 2023.- DEEP LEARNING, University of Copenhagen, Denmark
- International School of Chemometrics 2022.- HYPER, University of Copenhagen, Denmark
- International School of Chemometrics 2022.-BASIC, University of Copenhagen, Denmark

Research period abroad

- University of the Basque Country, Bilbao, Spain (4 months).
- GFZ German Research Centre for Geosciences, Potsdam, Germany (1 month).
- LMU Ludwig Maximilian University of Munich, Munich, Germany (1 month).

